PREDICTIVE MODELING OF DEGRADATION MECHANISMS IN ADVANCED LITHIUM BATTERIES AND BARRIER COATINGS

A Dissertation
Presented to
The Academic Faculty

by

Hao Luo

In Partial Fulfillment
of the Requirements for the Degree
Doctor of Philosophy in the
Georgia W. Woodruff School of Mechanical Engineering

Georgia Institute of Technology
December 2017

COPYRIGHT © 2017 BY HAO LUO

PREDICTIVE MODELING OF DEGRADATION MECHANISMS IN ADVANCED LITHIUM BATTERIES AND BARRIER COATINGS

Approved by:

Dr. Ting Zhu, Advisor
School of Mechanical Engineering
Georgia Institute of Technology

Dr. Hailong Chen
School of Mechanical Engineering
Georgia Institute of Technology

Dr. Shuman Xia
School of Mechanical Engineering
Georgia Institute of Technology

Dr. Matthew McDowell
School of Mechanical Engineering
Georgia Institute of Technology

Dr. Olivier Pierron
School of Mechanical Engineering
Georgia Institute of Technology

Dr. Meilin Liu
School of Materials Science and Engineering
Georgia Institute of Technology

Date Approved: 10/30/2017

ACKNOWLEDGEMENTS

First of all, I would like to thank my advisor, Dr. Ting Zhu, for his continuous invaluable guidance and support. Dr. Zhu has been always strict and helpful in research. Each time after discussion with him, I always feel motivated to tackle the difficulties encountered in research problems, not only because his expertise in my area sheds lights on feasible directions, but also because the way he tackles problems can always inspire me to think harder and deeper. Without Dr. Zhu's guidance and support, it would be impossible for me to finish my Ph.D. On the other hand, he is very easy going in daily life and cares a lot about my personal life. I would never forget when Dr. Zhu invited me and my fiancée to his house to celebrate the Thanksgiving Day; I would always remember the days when we welcome new team member and farewell to our old friends together. What is more important, he fully supports and understands my career choices! Dr. Zhu has been playing a very important role in my whole life and will continue to be a mentor for my future development. Just as the old Chinese saying said, "A teacher for a day is a father for a lifetime".

Also I would like to thank my thesis committee members: Dr. Hailong Chen, Dr. Meilin Liu, Dr. Pierron Olivier, Dr. Matthew McDowell, Dr. Shuman Xia for their valuable insights and comments on my research. In addition, I would like to extend my gratitude to my collaborators, including Dr. Yang Liu in Nanyang Technological University, Dr. Jiangwei Wang in Zhejiang University, Dr. Scott Mao in University of Pittsburgh, Dr. Qiaobao Zhang and Dr. Yong Yang in Xiamen University, Dr. Langli Luo and Dr. Chongmin Wang in Pacific Northwest National Laboratory, Dr. Samuel Graham, Ms. Shan

Xiong, Ms. Kyunjin Kim in Georgia Institute of Technology. Other than that, I would like to thank my teammates, Dr. Feifei Fan, Dr. Zhi Zeng, Mr. Baolin Wang, Mr. Yin Zhang and Dr. Dengke Chen for helpful discussions and support.

Last but not least, I would like to give my special thanks to my family, my parents, my brother and my fiancée. It is their endless love and sacrifice that have made my five years more meaningful and more worthwhile.

TABLE OF CONTENTS

ACKNOWLEDGEMENTS **iii**

LIST OF TABLES **vi**

LIST OF FIGURES **vii**

LIST OF SYMBOLS AND ABBREVIATIONS **xiii**

SUMMARY **xvi**

CHAPTER 1. INTRODUCTION **1**
1.1 Lithium ion batteries **2**
1.1.1 Silicon anode 3
1.2.1 Mixture cathode and parallel cells 6
1.2 Barrier layers 7

CHAPTER 2. LITHIUM ION BATTERIES **11**
2.1 **Si anode in lithium ion batteires** **11**
2.1.1 Lithiation model of Si anode 11
2.1.2 Introduction to the coating effect on Si anode 13
2.1.3 Lithiation of *c*-Si nanowires with SiO_x coating 15
2.1.4 Lithiation of *a*-Si nanotube with SiO_x coating 25
2.1.5 Lithiation of Ge/Si/Cu nanowire in lithium ion battery 43
2.1.6 Lithiation of Si nanoparticles coated with SiO_x 63
2.2 Parallel cells and mixture cathode **70**
2.2.1 Continuum model for parallel cell 70
2.2.2 Preliminary results and discussion for parallel cell 71
2.2.3 Continuum model of mixture cathode 74

CHAPTER 3. BARRIER LAYERS IN FLEXIBLE ELECTRONICS **76**
3.1 Elastic-viscoplastic model **77**
3.2 Time dependent cracking in SiN_x thin film within short time period **79**
3.3 Time dependent cracking in SiN_x thin film in long time period **94**

CHAPTER 4. CONCLUSIONS AND FUTURE RESEARCH **108**
4.1 Contributions **108**
4.2 Future research **109**

REFERENCES **111**

LIST OF TABLES

Table 3.1. Mechanical properties of PECVD SiN_x film and PET polymer substrate. 82

LIST OF FIGURES

Figure 1.1 Electronic devices in daily life. (a) A wearable watch by Apple; (b) A flex LG phone; (c) Portable laptop; (d) Thin film solar cell; (e) Tesla Model 3. 1

Figure 1.2 Development of batteries roadmap. (a) Energy density in terms of volume and weight for different battery materials. Reproduced from Ref[1]. (b) Anode candidates for the next generation of lithium ion batteries. Reproduced from Ref[2]. (c) Cathode candidates for the next generation of lithium ion batteries. Reproduced from Ref[1]. 3

Figure 1.3 (a) Silicon is only of the major elements on earth, taking place about 27.2% in weight among all the elements. Reproduced from Ref[6]. (b) Compared with graphite, the theoretical capacity of Si anode is almost 8 times of that of graphite anode. 4

Figure 1.4 Challenges for Si based anode in lithium ion batteries. (a) Pulverization of Si thin film anode after cycle. Reproduced from Ref[25]. (b) Fracture of Si nanoparticles anode after cycling. Reproduced from Ref[26]. (c) Fracture of Si nanowires anode after cycling. Reproduced from Ref[4]. 4

Figure 1.5. A schematic showing the clamping effect of coating on Si based anode. (a) SEI breaking and reforming during the cyclic lithiation and de-lithiation of Si nanoparticles (b) SEI breaking and reforming during the cyclic lithiation and de-lithiation of Si nanotube. (c) The clamping effect of coating protect the SEI from breakage during the cyclic lithiation and de-lithiation of Si nanotube. Reproduced from Ref[42]. 5

Figure 2.1 Morphological evolution of c-Si nanowire with coatings (a) Pristine Si nanowire with 7 nm SiO2 coating before lithiation. (b) Morphology of Lithiated Si. (c) A magnified view of pristine Si nanowire with 7nm SiO2 coating. (d) Diameters of total nanowire and unlithiated Si during lithiation for 7 nm coating. (e) Pristine Si nanowire with 11 nm SiO2 coating before lithiation. (f) Morphology of Lithiated Si, where localized fracture is observed. (h) Diameters of total nanowire and unlithiated Si during lithiatoin for 11 nm coating. 18

Figure 2.2 (a) Dynamic evolution of coating thickness during lithiation of Si with 7nm SiO_2 coating. Coating thickens first, then thins after reaches a maximum value. (b) Volume expansion of coating during lithiation. (c) Thickening process due to expansion of coating itself. (d) Thinning process due to stretch from expanding Si after SiO_2 coating is fully lithiated. (e) Lithiation sates in both SiO2 coating and Si core at two different lithiation stages. 21

Figure 2.3 Lithiation of Si nanowire with 11 nm SiO_2 coating. The SiO_2 coating keeps expanding until fracture. With more significant stress limited effect, less Si is lithiated than the case with thinner coating. 22

Figure 2.4. Lithiation of an *a*-Si nanotube with native oxide layers. (a) Pristine *a*-Si nanotube with native oxide layers, with inner and outer diameters of 330 and 280 nm, respectively. (b) The line scanning profile showing the element distributions along the radial direction of *a*-Si nanotube. The native oxide layers on both the inner and outer surfaces are less than 2 nm. (c) The lithiation kinetics of this *a*-Si nanotube, showing the evolutions of its outer (d_4) and inner (d_1) diameters as a function of the lithiation time. (d-f) The lithiation process of the *a*-Si nanotube with native oxide layers. A sandwiched lithiation structure of *a*-Li_xSi/*a*-Si/*a*-Li_xSi formed due to the lithiation from both inner and outer surfaces. No inward expansion was observed after the full lithiation. 28

Figure 2.5. Structural evolution of an a-Si nanotube with native oxides during lithiation and delithiation cycling. Reversible volumetric changes occurred during three cycles of lithiation and delithiation, without any inward expansion at the inner surface of the nanotube. 29

Figure 2.6 Significant volume expansion occurred after the lithiation of porous Si nanoparticles (a-b) and nanowires (c-d). 30

Figure 2.7. Chemomechanical modeling of the lithiation dynamics in an a-Si nanotube with native oxide. (a) Schematic of the model representing the cross section of an a-Si nanotube before lithiation. (b) Formation of a sandwich structure of a-LixSi/a-Si/a-LixSi during the first-stage lithiation. The inner and outer diameters of the a-Si nanotube are donated as d1 and d4, respectively. (c) Comparison between the experimental and simulation results of d1 and d4 as a function of reduced time t* during the two-stage lithiation. The reduced time t* is defined as the lithiation time normalized by the duration of the first-stage lithiation. 33

Figure 2.8. Lithiation of two a-Si nanotubes with different thicknesses of oxide coatings. (a) Schematic of the four diameters of d_1, d_2, d_3 and d_4 in an SiO_x/Si/SiO_x nanotube before lithiation, which involve the inner surface, the interface between the inner SiOx and a-Si layers, the interface between the outer SiOx and a-Si layers, and the outer surface, respectively. (b-f) In situ TEM lithiation of an *a*-Si nanotube with 3 nm and 4 nm SiO_x on the inner and outer surfaces, respectively (donated as 3‖4 nm SiO_x/Si/SiO_x nanotube). (b) The line scanning profile showing the thicknesses of the inner and outer SiOx layers in the SiO_x/Si/SiO_x nanotube. (c-f) Time-lapse TEM images of lithiation of the 3‖4 nm SiO_x/Si/SiO_x nanotube. (d) Lithiation initiated first from the outer surface and then from the inner surface, leading to a sandwich lithiation structure. (g-i) Lithiation of an a-Si nanotube with 4 nm and 6.5 nm SiO_x on the inner and outer surfaces, respectively (donated as 4‖6.5 nm SiO_x/Si/SiO_x nanotube). (g) High-resolution TEM (HRTEM) image showing the thicknesses of SiO_x layers on the inner and outer surfaces. (h-i) TEM images of the 4‖6.5 nm SiO_x/Si/SiO_x nanotube before and after lithiation. 35

Figure 2.9. Chemomechanical simulation results of the sandwich two-phase lithiation in an a-Si nanotube, after lithiation starts at the inner surface. (a) Radial distribution of the normalized Li concentration c (i.e., $Li_{2.3}Si$ corresponds to c = 0.8) at four characteristic stages. The symbol of d denotes the distance from the inner surface of the nanotube, and t is the thickness of the nanotube wall. (b-e) Corresponding radial distributions of stresses at four stages, S_{11} and S_{22} are respectively the radial and hoop stress in the cross section, and S_{33} is the axial stress in the nanotube. All the distributions are plotted on the undeformed configuration using ABAQUS, so as to facilitate comparison between different stages. 37

Figure 2.10. Lithiation of an a-Si nanotube with oxide coatings thicker than those in Figure 2.8. (a) The pristine 6.5‖9 nm SiO_x/Si/SiO_x nanotube. (b) HRTEM image showing the thickness of the inner and outer SiO_x layers before lithiation. (c) HRTEM image showing the thickness of the lithiated inner and outer SiO_x layers after full lithiation. (d) The outer SiO_x layer was first lithiated, accompanied by a thickness increase from 9 nm to 12 nm. (e-f) TEM images showing the first-stage lithiation, resulting in a sandwich lithiation structure, and the second-stage lithiation, resulting in a total volume expansion of ~ 220% (relative to *a*-Si). 39

Figure 2.11. Schematic illustration of a high-performance Cu/Si/Ge nanowire (NW) electrode. a, The Cu/Si/Ge NW array was grown on a Ni foam substrate, and b, each NW had a core of Cu segments and a Si/Ge bilayer shell. c, The favorable design features, in conjunction with the synergy of active Si and Ge through dynamic co-lithiation/co-delithiation, enable long-cycle stability in the Cu/Si/Ge NW electrode, while the Si/Ge thin-film electrode and Si NW (or NT) electrode are prone to mechanical degradation in both active components and SEIs during cycling. 46

Figure 2.12. Characterization of the Cu/Si/Ge NW electrode. a-c, SEM images of Cu/Si/Ge NW arrays grown on a Ni foam. d-e, TEM image of a single Cu/Si/Ge NW, f, HRTEM image of the Si/Ge bilayer with corresponding SAED pattern (inset). g, STEM image of a Cu/Si/Ge NW, with corresponding EDX scan-line spectra and h, STEM mapping. 48

Figure 2.13. Electrochemical performance of the Cu/Si/Ge NW electrode. a, Capacity performance at a slow rate of 0.2C. b, Corresponding galvanostatic charge–discharge profiles at different cycles. c, Long-cycle performance for Cu/Si/Ge NW, Cu/Si NW and Si/Ge thin-film electrodes at 2C; all the electrodes were first tested at 0.2C for two cycles and then subjected to long-term cycling. d, Comparison of specific capacity of Cu/Si/Ge NW, Cu/Si NW and Si/Ge thin-film electrodes at various C rates (from 1C to 16C) for 100 cycles and then 1C for another 900 cycles; all the electrodes were first tested at 0.2C for two cycles and then under rate testing. 49

Figure 2.14. In situ TEM and cyclic voltammetry (CV) experiments. a, Time-lapse TEM images of lithiation of a single Cu/Si/Ge NW. b, Magnified TEM images showing the thicknesses of the Si/Ge bilayer shell as a function of time during lithiation, and c, corresponding quantitative measurements showing the thickness changes of Si/Ge bilayer shell as a function of lithiation time. d-f, CV curves for the Cu/Si/Ge NW, Cu/Si NW, and Cu/Ge NW electrodes during the first three discharge/charge cycles, respectively. 53

Figure 2.15. Chemomechanical effects of lithiation of a Si/Ge NT. a-d, Chemomechanical simulation snapshots showing progressive bending (left) and the cross-sectional distribution of the normalized Li/Ge concentration (right) in a Si/Ge NT during stage I of lithiation of Ge only and stage II of co-lithiation of Si and Ge. e, Illustration of dominant mechanical expansion near the surface during lithiation of a Si NT. f, Illustration of electrochemical-mechanical expansion associated with insertion of active Li near the surface during co-lithiation of a Si/Ge NT. 55

Figure 2.16. Comparison of microstructural changes in the Cu/Si NW and Cu/Si/Ge NW electrodes after 3000 cycles at 2C. a, SEM image of a Cu/Si/Ge NW array. b, TEM image of a single Cu/Si/Ge NW. c, SEM images of a Cu/Si NW array. d, TEM image of a single Cu/Si NW. 59

Figure 2.17 The TEM images of Si nanoparticles with different oxidation treatment. The coating thickness from (a) to (g) and the corresponding treatment methods are shown in (h). (a) Pristine Si nanoparticles; (b) Si nanoparticle with native oxide layer about 1 nm thick; (c) Si nanoparticle treated under 650 ^oC for 20 min, resulting in 1 nm coating thickness; (d) Si nanoparticle treated under 750 ^oC for 20 min, resulting in 5 nm coating thickness; (e) Si nanoparticle treated under 750 ^oC for 60 min, resulting in 6 nm coating thickness; (f) Si nanoparticle treated under 850 ^oC for 5 min, resulting in 8 nm coating thickness; (g) Si nanoparticle treated under 850 ^oC for 20 min, resulting in 10 nm coating thickness. 64

Figure 2.18 Cycle performances of Si nanoparticles anode coated different thickness of SiO_x at discharge/charge current densities of 210 mA/g between voltage 5 mV and 2V. 65

Figure 2.19 Model setup and parameter definitions in the model. (a) ¼ asymmetrical model with symmetrical boundary at x and y directions. The lithium flux is applied on the surface of SiO_x coating; (b) The initial radius of Si is defined as R_0, the initial thickness of coating is t_0 and the initial volume of Si is defined as V_0; (c) The final state of the Si and coating when the lithiation stops due to self-limit effect. The unlithiated Si is defined as V^u. 66

Figure 2.20 Competing effect from self-limit lithiation and coating fracture. (a) The percentage of unlithiated Si as a function of coating thickness t_0 at two different stopping pressures, namely 2.5 GPa and 4.0 GPa; (b) The hoop stress on the surface of lithiated SiOx coating as a function of coating thickness t0 when the lithiation stops at two different stopping pressures. (c) A competing effect from self-limit and coating fracture resulting in an optimal thickness regime for S = 4.0 GPa. 68

Figure 2.21 An example showing the hoop stress distribution. The Si anode has 20 nm in radius and the thickness of coating is 5 nm. (a) The hoop stress distribution of the whole model, showing the maximum stress occurs in the coating; (b) the hoop stress distribution of the SiO_x coating, showing the maximum stress on the interface between Si and SiOx. 69

Figure 2.22 Experimental setup for parallel cells. (a) A schematic view of parallel cells. (b) Voltage variation with time, when current is controlled during charge and discharge process. The voltage cutoff is 4.4 V and 2.5 V, respectively. 72

Figure 2.23 Preliminary results for current distributions with rate ranging from C/5 to 2C. (a) A schematic view of parallel cells. (b) EIS measurement of cell resistance as a function of SOC for both charge and discharge process. (c)-(f) Current distributions in cell A and cell B under rate of C/5, C/2, 1C and 2C, respectively. 73

Figure 2.24 (a)-(c) Distributions of electrode potential, electrolyte potential and electrolyte concentrations at end the charge process. 74

Figure 2.25 A schematic illustration of ionic exchange between two particles of different size. 74

Figure 3.1 Example of time-dependent channel crack growth in 250-nm-thick SiNx in air at strain values of (a) 0.6 and (b) 0.7%, respectively. (c) Schematic of the crack model. The SiNx thin film is perfectly bonded to the PET substrate, h/H = 1/100. (d) Stress relaxation curve for PET at strain of 0.7%, 1% and 5% under air and N2 conditions. 77

Figure 3.2 (a) Stress-strain curve of PET substrate. (b) Stress relaxation curves of PET substrate. 78

Figure 3.3. Finite element model and results. (a) The von Mises stress contour in SiNx thin film and PET substrate (lower image) and magnified view of stress concentration around the crack tip in SiNx thin film (upper image). (b) The von Mises stress contour in PET, where high stresses develop beneath the crack wake in PET. (c) Calculated Gss versus ε_{app}, compared to Eqs. 3.3 and 3.6. 79

Figure 3.4 Time evolution of energy release rate and stress beneath the crack wake in PET. (a-d) The von Mises stress contour in PET at different times as indicated in (e), showing the viscous stress relaxation effect. (e) Peak stress in PET and corresponding energy release rate for film cracking as a function time. 84

Figure 3.5. Influence of thickness on ε_c and K_c for SiN_x on PET substrate. 85

Figure 3.6. Effect of strain rate on onset critical strain of 250-nm-thick SiN_x in air and dry air at room temperature. 87

Figure 3.7 (a) Measured crack growth rates of 250-nm-thick SiN_x as a function of stress intensity factor in air (green circle), nitrogen (red diamond) and dry air (blue triangle) and (b) density of cracks in air and in nitrogen measured 30 minutes after first observed crack. 89

Figure 3.8. Crack extension as a function of time. 89

Figure 3.9. J-integral contour (red square) used for calculation of energy release rate of film cracking. 93

Figure 3.10. Finite element mesh of the crack model. (a) Global view of the mesh in the system. (b) Top view of the mesh of the system. (c) Magnified view of the mesh near the crack tip in SiN_x film. (d) Mesh of PET (e) Magnified view of the mesh in PET underneath the crack. 93

Figure 3.11. (a) Schematic illustration of in-situ microscopy of a SiN_x /PET sample kept at different applied strains, for optical imaging and measurement of channel crack growth and crack extension as a function of time. (b) Measured crack growth rate as a function of driving force G for a channel crack in a 250nm-thick SiN_x film in air and nitrogen, respectively. (c - d) SEM images of SiN_x / PET cross section (cut by FIB) showing the channel crack in the film as well as the substrate crack beneath the channel crack, under (c.1-2) applied strain 0.75% for half an hour and (d.1-2) applied strain 0.6% for 5 days. 96

Figure 3.12. (a) Measured crack growth rate in SiN_x / PET at the applied strains of 0.55% and 0.58% in air. (b) Calculated driving force of an isolated crack as a function of substrate cracking depth a', when the applied strain is 0.58%. (c) Calculated driving force of a crack with spacing S to the neighboring long crack on its either side, when the applied strain is 0.75%. 97

Figure 3.13. (a) Calculated driving force of a crack as a function of substrate cracking depth of neighboring cracks. (b) Calculated driving force of a crack as a function of substrate cracking depth a' in the presence of neighboring cracks with a fixed substrate cracking depth a. Both (a) and (b) were calculated under the applied strain 0.75%, residual strain -0.15%, crack spacing 100μm. (c) Schematics of different cracking modes in the SiN_x film and PET substrate, marked with the associated crack driving force, see text for details; crack spacing S, substrate cracking depth in neighboring cracks a, and in growing crack a’ are chosen for each case. (d) Measured time dependent crack growth rate of SiN_x / PET in air, while the applied strain was kept at 0.5, 0.55, 0.6, 0.75%, respectively. For the applied strain 0.6%, the last data point at 120 hours corresponds to the sample in Fig. 3.11d. (e) Crack spacing as a function of time at the applied strain of 0.75% and 0.6%, respectively. 99

Figure 3.14. Crack growth rate behavior of SiN_x / PET at the applied strain of 0.75% subjected to change of environmental condition. 103

Figure 3.15. (a) Time-dependent crack growth rate behavior of SiN_x deposited on PET at the applied strain 0.75% versus on PI at the applied strain0.85%. (b) SEM images of SiN_x / PET and SiN_x / PI after 1 hour and 2 days passed, respectively. 105

Figure 3.16 A general mesh schema used in calculating the driving force with finite element analysis. (a) A whole view of a meshed model, which is used to calculate the crack driving force of SiN_x thin film when neighboring substrate cracks are present. (b) A view of meshed middle layer of PET substrate which has thickness of substrate penetration depth. (c) A magnified view of the mesh on the top surface of (b). (d) A magnified view of the mesh in the side surface of (b). 107

LIST OF SYMBOLS AND ABBREVIATIONS

c	Lithium concentration
σ_{ij}	Stress component
σ_0	Yield stress
ε_{ij}^{c}	Strain component induced by lithiation
ε_{ij}^{e}	Strain component induced by elastic deformation
ε_{ij}^{p}	Strain component induced by plastic deformation
ε_v	Volumetric strain
E	Elastic modulus
β_{ij}	Component of expansion coefficient induced by lithiation
Ω	Activation volume of lithium diffusion
D	Lithium diffusivity
c^A	Effective concentration of electrolyte A
I	Current in the battery
κ^A	Ionic conductivity of electrolyte A
Φ_{ele}^{A}	Electronic potential in electrolyte A
f^A	Mean molar activity coefficient of electrolyte A

t_+^0	Transference number of anion
σ^A	Electronic conductivity of active material A
Φ_s^A	Electronic potential in solid electrode A
a	crack length
E_f^*	Plain strain elastic modulus
G_{ss}	Driving force for crack propogation (energy release rate)
Z	Dimensionless energy release rate
α	Elastic mismatch
h	Thin film thickness
K	Stress intensity factor
1D	One-dimensional
3D	Three-dimensional
a-Si	Amorphous Silicon
c-Si	Crystalline Silicon
CV	Cyclic Voltammetry
FIB	Focused Ion Beam
HRTEM	High-resolution Transmission Electron Microscopy
MD	Molecular Dynamics

NW	Nanowire
NT	Nanotube
PET	Polyethylene Terephthalate
PI	Polyimide
SEI	Solid-electrolyte Interphase
SEM	Scanning Electron Microscope
TEM	Transmission Electron Microscopy

SUMMARY

Lithium batteries play a critical role in the emerging landscape of renewable energies. On the anode side of lithium batteries, silicon is a promising candidate to replace the currently used graphite. However, the mechanical degradation of Si anode induced by the large volume changes during charge and discharge hinders its wide applications in lithium batteries. To mitigate the degradation, Si nanowires or nanotubes with surface coatings are often used. But it remains unclear regarding the effects of coatings and structural changes on the degradation mechanisms in Si anodes. In this thesis, a predictive chemomechanical model will be developed to account for two-phase lithiation/delithiation and large volume changes during the lithiation and delithiation process. Alongside in situ transmission electron microscopy experiments, this chemomechanical model will be used to investigate the degradation mechanisms in Si nanowires, nanotubes and nanoparticles with coatings. The optimal design of coatings has been explored to maximize the benefits of Si based anodes. On the cathode side of lithium batteries, a major technical challenge is to achieve both high energy density and high power density simultaneously. To address this challenge, a mixture cathode consisting of $Li_{1+x}(Ni_xCoyMn_{1-x-y})O_2$ (Li-excess NMC) and nano $Li(NiCoMn)_{1/3}O_2$ (nano NMC) has been designed by our collaborators. To evaluate this design, a continuum electrode model has been developed to characterize the thermodynamics, reaction kinetics and diffusion processes in the heterogeneous electrode structures. This model enables predictions of the electrochemical behaviors of cathodes with different particle distributions and compositions, so as to guide the optimization of cathode design. Another issue for cathode is the loss of energy density for parallel cells.

The developed continuum model has then been adapted to study the origin of current distribution of two parallel cells within a battery.

In addition to lithium batteries, barrier coatings are crucial for the reliable operation of flexible electronics. To characterize the strain limits of barrier coatings in flexible electronics, a singular critical onset strain value is often used. However, such metrics do not account for time-dependent or environmentally assisted cracking, which can be critical to the overall reliability of these thin-film coatings. In this thesis, the time-dependent channel crack growth behavior of silicon nitride barrier coatings on polyethylene terephthalate substrates will be investigated in dry and humid environments. To elucidate the origin of the time-dependent crack growth behavior, predictive numerical simulations will be carried out based on the continuum elastic-viscoplastic model. The integrated experiment and modeling will provide a guideline for the optimal design of reliable barrier coatings. Overall, the models and numerical producers developed in this thesis will provide a basis for further study of the reliable lithium batteries and barrier coatings.

CHAPTER 1. INTRODUCTION

Electronic systems can be seen everywhere in current society, ranging from smart phones, electronic watches, laptops to electric vehicles, satellites (Figure 1.1). In the future, electronic systems are expected to become more intelligent, more flexible, more powerful and more reliable. For instance, phones or even laptops can be worn on wrists; electric vehicles and satellites can function longer and smarter with powerful and stable batteries. To achieve these future systems, two critical components are critical, namely barrier layers for flexible displays and batteries for reliable power systems. Hence, the research proposed here is devoted to the understanding of barrier layers and batteries through the integration of modeling and experiments, so as to facilitating the development of more advanced electronic systems for future use.

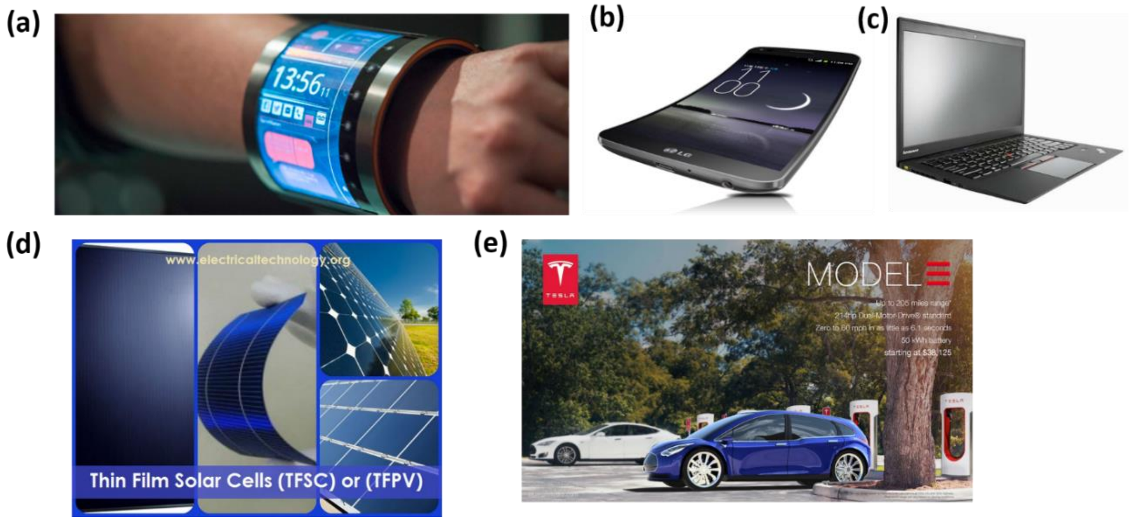
(a)
13:56
(b)
(c)
(d)
www.electricaltechnology.org
Thin Film Solar Cells (TFSC) or (TFPV)
(e)
TESLA
MODEL

Figure 1.1 Electronic devices in daily life. (a) A wearable watch by Apple; (b) A flex LG phone; (c) Portable laptop; (d) Thin film solar cell; (e) Tesla Model 3.

1.1 Lithium ion batteries

Lithium ion batteries (LIBs) have been received extensive attention as they are considered as the leading electrical energy storage system, due to its high energy density, flexible and lightweight design, fast charge/discharge rates and long cycle life[1], as shown in Figure 1.2(a). Essentially, a battery is composed of several electrochemical cells, where each cell consists of a cathode and an anode separated by electrolyte solution. To develop high-performance batteries, both cathode and anode are expected to contribute. On the anode side of lithium batteries, materials in three different categories are studied: insertion/de-insertion materials (Carbonaceous material, Titanium oxides), alloy/de-alloy materials (Germanium, Tin, Antimony, Tin Oxide, Si) and conversion materials (Metal oxides, metal phoshides/sulfides/nitrides), as shown in Figure 1.2(b). In general, insertion/de-insertion materials are cheap and safe, but its low efficiency and capacity remain a major concern; alloy/de-alloy materials usually have high energy density and capacity, but they suffer from irreversibility of capacity; conversion materials are also cheap due to their abundancy in earth and their capacity is usually high, but their low coulombic efficiency and short longevity hinder their applications[2].

Among all the candidates, silicon (Si) is a promising candidate to replace the currently used graphite, highest theoretical capacity of 3579 mAh g-1 ($Li_{15}Si_4$) at room temperature[2-4] and rich abundancy in earth(see Figure 1.3(a) – 1.3(b)). Details about the study of Si anode will be reviewed soon in section 1.1.1. On the cathode side, the corresponding lithiated materials as mentioned previously for anode are the cathode candidates for future lithium ion batteries, as shown in Figure 1.2(c). However, single cathode material that enable high energy density and high power density simultaneously has not been found yet[5,6].

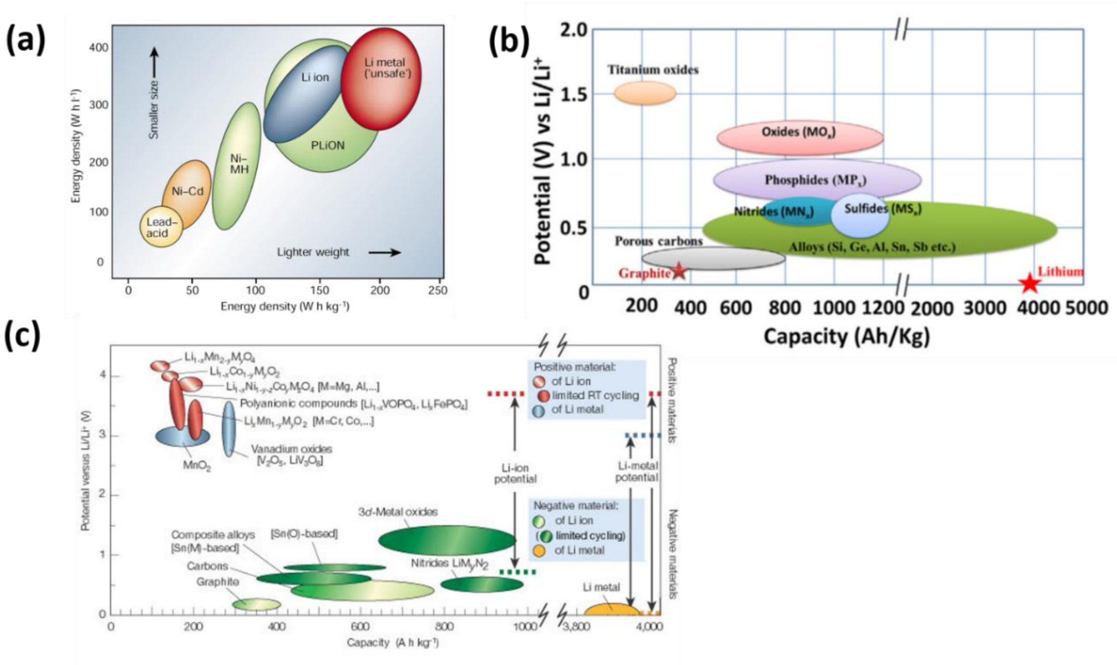

Figure 1.2 Development of batteries roadmap. (a) Energy density in terms of volume and weight for different battery materials. Reproduced from Ref[1]. (b) Anode candidates for the next generation of lithium ion batteries. Reproduced from Ref[2]. (c) Cathode candidates for the next generation of lithium ion batteries. Reproduced from Ref[1].

Instead, mixture cathode composing of different materials has been studied[7-13], which provides a way to achieve cathode of both high energy density and high power density. Also, optimal design of parallel cells is also critical to achieve high energy density for high current applications[14, 15]. As two key components of a battery, both anode and cathode will be discussed as followed.

1.1.1 Silicon anode

Silicon is one of the most promising anode materials for next-generation LIBs[16-21], due to its high theoretical capacity of 3579 mAhg^{-1} ($Li_{15}Si_4$) at room temperature, as shown in Figure 1.3(c). However, dramatic volume changes (~ 300%) of Si occur during

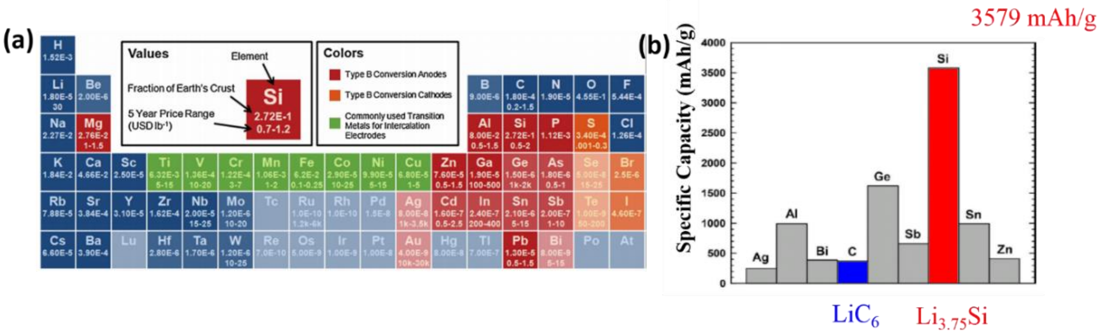

Figure 1.3 (a) Silicon is only of the major elements on earth, taking place about 27.2% in weight among all the elements. Reproduced from Ref[6]. (b) Compared with graphite, the theoretical capacity of Si anode is almost 8 times of that of graphite anode.

lithiation/delithiation, which can cause severe cracking and pulverization of Si anodes[3, 22-24], as shown in Figure 1.4. Such mechanical degradation often leads to loss of electrical contact between the active Si and the current collector, as well as destruction and regeneration of the solid electrolyte interphases (SEIs) on fractured Si surfaces, thereby resulting in rapid capacity fading (Figure 1.5a).

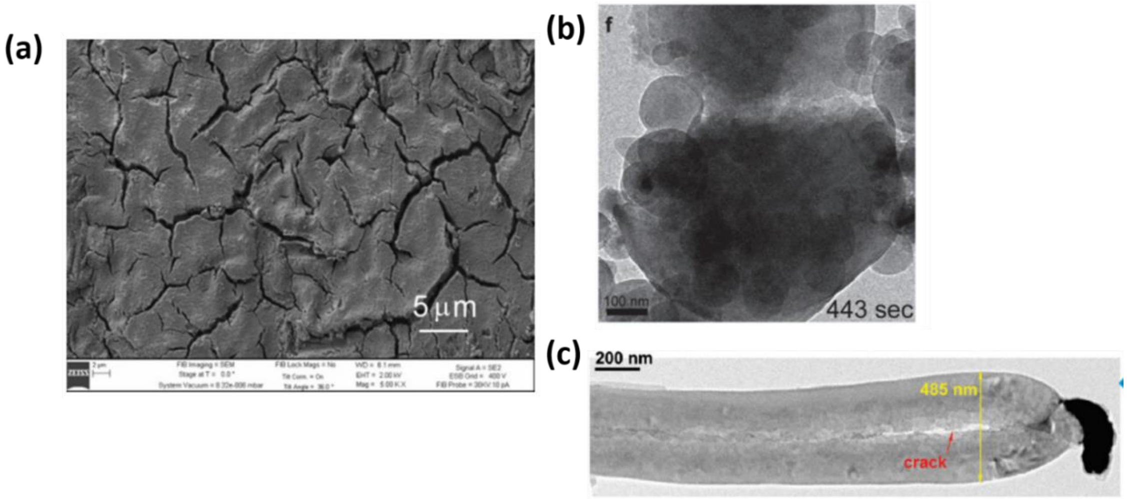

Figure 1.4 Challenges for Si based anode in lithium ion batteries. (a) Pulverization of Si thin film anode after cycle. Reproduced from Ref[25]. (b) Fracture of Si nanoparticles anode after cycling. Reproduced from Ref[26]. (c) Fracture of Si nanowires anode after cycling. Reproduced from Ref[4].

In recent years, tremendous efforts have been devoted to mitigate the electrochemically-induced mechanical degradation of Si electrodes[3]. Several effective material and electrode design strategies have been demonstrated for alleviating Si degradation during cycling. For example, reducing the feature size of Si particles and wires to the nanoscale can avert cracking and fracture[23, 27]. Creating hollow space in Si particle shells and tubes can reduce outward expansion during lithiation, thereby alleviating mechanical damage and regeneration of SEIs[28-31]. Besides engineering the geometry of Si electrodes, coatings of carbonaceous materials[32-34], metals[35, 36], oxides[29, 37-40] or conducting polymers[41] are often used, as shown in Figure 1.5. Coatings can enhance electrical transport, thus improving both the rate performance and uniform utilization of active Si. Meanwhile, coatings can impose mechanical confinement, alleviating the degradation of Si. However,

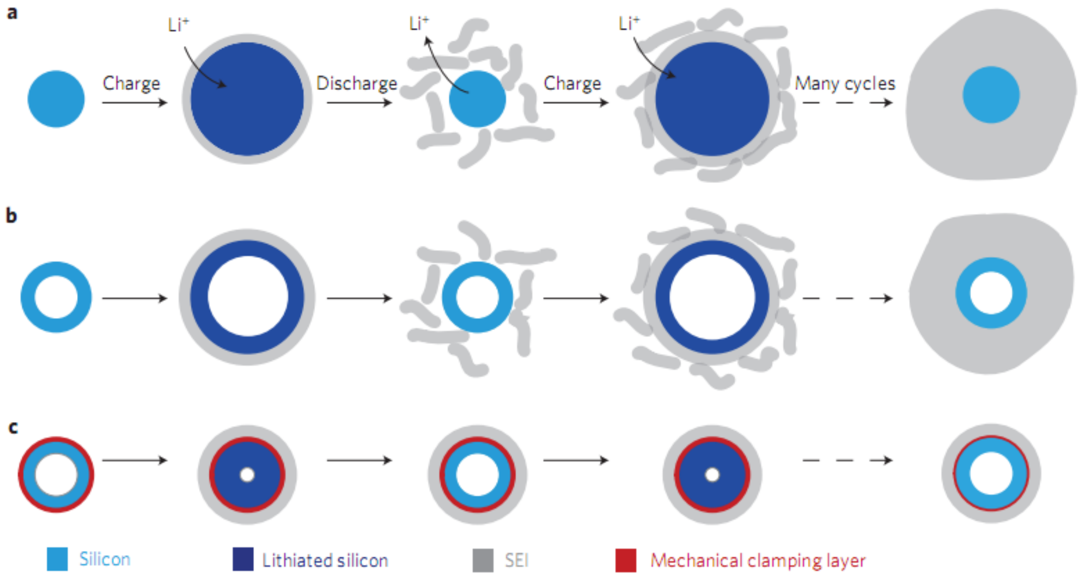

Figure 1.5. A schematic showing the clamping effect of coating on Si based anode. (a) SEI breaking and reforming during the cyclic lithiation and de-lithiation of Si nanoparticles (b) SEI breaking and reforming during the cyclic lithiation and de-lithiation of Si nanotube. (c) The clamping effect of coating protect the SEI from breakage during the cyclic lithiation and de-lithiation of Si nanotube. Reproduced from Ref[42].

one drawback of these coatings is that the specific capacity is usually reduced, due to their low Li storage capacity relative to Si. In addition, it remains unclear regarding the effects of coatings and structural changes on the degradation mechanisms in Si anodes. In section 2.1.1, a predictive chemomechanical model will be developed to account for two-phase lithiation/delithiation and large volume changes during the lithiation and delithiation process. Combined with in situ transmission electron microscopy experiments, this chemomechanical model will be developed to investigate the degradation mechanisms in Si based nanowires (section 2.1.3 and section 2.1.5), nanotubes (section 2.1.4) and nanoparticles (section 2.1.6) with coatings. Lastly, the optimal design of coatings will be explored to maximize the benefits of Si based anodes, as well as other beneficial effects aforementioned, i.e. hollow space and small feature size etc.

1.1.2 Mixture cathode and parallel cells

A major technical challenge for developing cathode for lithium ion batteries is to achieve both high energy density and high power density simultaneously. Instead of satisfying these two requirements with single cathode material, mixture of two or more active cathode materials has succeeded in some sense by combining the advantages in those materials in the same cathode, like $LiNi_xCo_yAl_{1-x-y}O_2$ (NCA)and $LiCoO_2$ (LCO)[43], $LiNi_xCo_yAl_{1-x-y}O_2$ (NCA) and $LiMn_2O_4$ (LMO)[7, 44], $Li(Ni_{1/3}Co_{1/3}Mn_{1/3})O_2$ (NCM) and $LiNi_xCo_yAl_{1-x-y}O_2$ (NCA)[11], $LiFePO_4$ (LFP) and $LiCoO_2$ (LCO)[45], $LiMn_2O_4$ (LMO) and $LiFePO_4$ (LFP)[46] $LiMn_2O_4$ (LMO) and $Li(Ni_{1/3}Co_{1/3}Mn_{1/3})O_2$ (NMC)[12], etc. Additionally, particle size impacts directly on the power capacity of lithium ion batteries. Therefore, the corresponding nanosized structure of cathode materials is often engineered to obtain high power density[47, 48]. Based on these previous studies, we propose a mixture cathode consisting of binary distribution of Li-excess NMC and nano NMC. It is expected that during charging or relaxation, interparticulate Li ion transport can occur between nm-sized and um-sized particles. The study by Nazar and co-workers indicated that nano-LiFePO4 can "suck" Li ion from bulk LiFePO4 particles after charging[49]. This phenomenon is also confirmed by other experiments[50] and modeling[51]. Another important aspects of losing energy density come from inhomogeneous current distributions in parallel cells within a battery[14, 15]. However, mechanisms of inhomogeneous current distributions in parallel cells are not clear yet, which can be important for optimal design of battery. In this thesis, electrochemical models developed by Newman and coworkers[9, 52] will be adopted to predict electrochemical behaviors of mixture cathode (section 2.2.1-2.2.2) and parallel cells (section 2.2.3).

1.2 Barrier layers

Barrier layers that contain ultrathin inorganic hard coatings on PET substrates have become indispensable to the flexible electronics industry for maintaining a reliable operation of devices, with the most notable demand from organic light emitting diodes for flexible displays and thin film solar cells, see Figure 1.1(c) and Figure 1.1(d). For these applications, various barrier film architectures (multilayer stacks) and processing methods (e.g., PECVD, ALD, etc.) have been developed to create ultrabarrier films with an effective water vapor transmission rate (WVTR) less than 10^{-4} g/m^2/day. Of these methods, multilayer amorphous silicon nitride (SiN_x) thin films fabricated by plasma enhanced chemical vapor deposition (PECVD) have recently found success in the development of flexible ultrabarrier coatings with WVTR on the order of 10^{-6} g/m^2/day and have also been demonstrated on flexible displays.[53-59] SiN_x films can be deposited at low temperatures (~100°C) and high deposition rates (60 nm/min) while exhibiting great barrier film qualities, such as low porosity and excellent transparency.[60-63] Moreover, residual stresses can be controlled through the PECVD deposition conditions, i.e. substrate temperature, plasma power, chamber gas pressure and chemical composition (i.e. ratio of silicon to nitride in this case).[64, 65] This allows the SiN_x films to have compressive residual stresses, which help prevent pre-existing microcracks from growing without applied external loads.[66]

Flexible electronics are by design meant to be subjected to applied strains. It is therefore of paramount importance to study the mechanical reliability of the inherently brittle barrier coatings, including channel cracking of the coating and its debonding from the PET substrate. Most of the related reliability studies have so far focused on determining the critical onset strains to failure and density of cracks.[67-75] For example, George and coworkers specifically studied nanoscale ALD and MLD layers.[67-69] Leterrier and coworkers also reported that inherent microdefects in inorganic films initiate crack propagation.[70-72] However, when considering the application of these barriers to flexible electronics, the strains applied may be much different than the monotonic loading that is found in most of the studies for crack onset strain. This includes the application of fixed strains for curved devices or the application of cyclic strains during flexure, both of which may allow time dependent behavior to occur. Thus, the question arises as to the appropriateness of the use of crack onset strain results to the wide range of loading conditions that may be seen in such coatings in flexible electronic devices since time dependent effects are not readily captured by this approach. In fact, Suo and co-workers demonstrated that time-dependent cracking of an elastic film made of a material that does *not* undergo any subcritical cracking (i.e., no environmentally-assisted cracking nor stress corrosion cracking) can occur if a viscous underlayer (i.e., a layer that undergoes creep) is present between the film and an elastic substrate.[76-79] The physical explanation relies on the following fact: as the underlayer creeps, the stress field relaxes in the crack wake, resulting in a decreased constraint effect of the underlayer on the film and therefore an increased driving force for crack extension (i.e., the stress field around the crack tip intensifies). If over time the driving force exceeds a critical value, crack extension occurs; after some amount of cracking, the driving force is reduced due to a larger constraint effect of the underlayer that has not crept yet. The process can repeat itself, and a steady state crack velocity is attained. Clearly, a similar cracking scenario can occur for thin barriers on PET substrates under tensile strains, depending on the viscous properties of the polymer. Here, we studied the time-dependent crack growth properties of SiN_x coatings on polyethylene terephthalate (PET) substrates by considering both polymer creep and subcritical cracking of the SiN_x films thanks to an integrated experimental and numerical approach.

Many brittle films undergo environmentally-assisted subcritical cracking, such as SiO_2 films.[80-83] So far, there are few studies on environmentally-assisted cracking of SiN_x films, although environmentally-assisted debonding between SiN_x films and Cu has already been demonstrated.[84] Recently, Vellinga *et al.* observed faster crack propagation in SiN_x barriers on polyethylene naphthalate (PEN) substrates in higher relative humidity surroundings using resistance measurements and *in situ* microscopy. They argued that this environmental effect was unlikely due to the hygroscopic expansion of the polymer, and instead concluded that SiN_x barriers undergo environmentally-assisted cracking.[85] Guan *et al.* also performed electro-mechanical two point bending tests in dynamic and static loading modes to determine the subcritical crack growth exponent *n* in SiN_x coatings on PEN substrates.[86] Their results suggest that SiN_x thin films behaves differently from bulk Si_3N_4 ceramics that are essentially immune to environmentally assisted cracking.[87, 88] However, these studies neither directly measured the crack growth rates as a function of driving force for channel cracking, nor considered the aforementioned potential effects of polymer relaxation. It is therefore the goal of this study to characterize and investigate the crack growth behavior of SiN_x films on a PET substrate in both short (section 3.2) and long time period (section 3.3) under different environments by employing an *in situ* microscopy technique for measurement of crack growth. To elucidate the origin of the time-dependent crack growth behavior, predictive numerical simulations has been carried out based on the continuum elastic-viscoplastic model (section 3.1). The integrated experiment and modeling will provide a guideline for the optimal design of reliable barrier coatings.

CHAPTER 2. LITHIUM ION BATTERIES

2.1 Si anode in lithium ion batteries

2.1.1 Lithiation model of Si anode

In situ transmission electron microscopy (TEM) experiments reveal that lithiations in crystalline silicon (*c*-Si) often proceeds through movement of an atomically sharp phase boundary that separates lithiated and unlithiated silicon, corresponding by large elastic and plastic stress[4, 89, 90], which often causes the fracture of Si anode. The large lithiation induced strains in *c*-Si are orientation dependent (expansion mainly occur in <110> and much lower in <111>)[4, 90, 91] , and thus design of Si anode should take this anisotropic chemical strain into consideration. Interestingly, two phase lithiation mechanism also applies to amorphous silicon (*a*-Si) [26, 92]. Different to lithiations in *c*-Si, the lithiation strains in a-Si are expected to be isotropic. Theoretical models and analysis that account for the two phase lithiation process and associated stress generations have been developed[92-97]. Since structural change and stress evolutions during lithiation/delithiation are the focus of this study, the detailed dynamics of evolving multiphase microstructures are not considered here. To account for the lithiations in different Si anodes of various shape, a flexible model is developed based on previous two phase model[95], which account for large volume expansions, elastic-plastic stress generations, two stage lithiations for *a*-Si, anisotropic expansions, co-lithiations, etc. As followed is a review of the main part of this model for lithiation.

$$\dot{\varepsilon}_{ij} = \dot{\varepsilon}_{ij}^{c} + \dot{\varepsilon}_{ij}^{e} + \dot{\varepsilon}_{ij}^{p} \qquad (2.1)$$

Equation (2.1) denotes strain decomposition of total strain rate, which consists of chemical strain rate $\dot{\varepsilon}_{ij}^{c}$ elastic strain rate $\dot{\varepsilon}_{ij}^{e}$ and plastic strain rate $\dot{\varepsilon}_{ij}^{p}$ It should be noted that here strains are defined as true strain instead of engineering strains, since large deformations are involved in the lithiation process.

$$\dot{\varepsilon}_{ij}^{c} = \beta_{ij}\dot{c} \tag{2.2}$$

Equation (2.2) defines chemical strain rate, which is proportional to the time variation of lithium concentration $\dot{c}$. β_{ij} is the lithiation expansion coefficient, which can be tuned to represent anisotropic strains. It is noted that only normal chemical strains have non-zero value.

$$\dot{\varepsilon}_{ij}^{p} = \dot{\bar{\varepsilon}}^{p} \frac{\sigma'_{ij}}{\sigma_e} \tag{2.3}$$

$$\dot{\bar{\varepsilon}}^{p} = \dot{\bar{\varepsilon}}_0^{p} \left(\frac{\sigma_e}{\sigma_Y} \right)^{1/m} \tag{2.4}$$

Equation (2.3) and (2.4) defines plastic strain rate. In equation (2.3), σ'_{ij} is the deviatoric stress, σ_e is the effective stress. Equation (2.4) denotes strain rate hardening behavior, where $\dot{\bar{\varepsilon}}_0^{p}$ is a strain rate constant, σ_Y is the plastic flow resistance, and m is the rate sensitivity exponent.

$$\varepsilon_{11} + \varepsilon_{22} + \varepsilon_{33} = \varepsilon_v \tag{2.5}$$

$$\varepsilon_v^c = \varepsilon_{v^1}^c + \varepsilon_{v^2}^c \tag{2.6}$$

Equation (2.5) denotes the fact that volume expansion are the sum of the normal strains, ε_v where denotes the true volume strain. Equation (2.6) denotes the volume expansions in two stage lithiation, where the total volume expansion equals to the volume expansion in the two stages.

2.1.2 Introduction to the coating effect on Si anode

Lithium ion batteries (LIBs) have been received extensive attention as they are considered as the leading electrical energy storage system. High energy/power density and long cycle ability in safe operation are the main specifications that the researchers have been pursuing for a long time.[1, 98] However, due to the huge stress that is generated upon lithium ion insertion/extraction into/from the electrodes during lithiation/delithiation, significant mechanical issues such as fracture and pulverization are accompanied with the electrochemical cycling process. Meanwhile, the reformation and continuous growth of solid electrolyte interphase (SEI) layer on the fresh surface of electrode materials after fracture can result in low Columbic efficiency and high impedance. Therefore, it is difficult to reach the theoretical energy storage capacity, especially for the high-capacity electrode materials, such as Si, Ge, Sn and SnO_2.[99-103] One straightforward strategy is to adopt a secondary phase material to coat on the surface of active materials, as shown in Figure 1.5 aforementioned. The improvements of the battery performance upon the functional surface coating have generally been attributed to the following reasons: 1) The surface coating layer can provide a compressive stress on the inner active materials, which can mechanically suppress the volume expansion of the electrodes and in turn mitigate the mechanical issues; 2) The surface coating layer can prevent the active materials from losing of contact with the electrode after pulverization, as well as prevent the isolated materials from welding in the subsequent cycles; 3) The surface coating layer can isolate the active materials from the electrolyte, which can hinder the continuous growth of SEI layer; 4) The surface coating layer can act as an artificial SEI layer after cycles, which can improve the reaction kinetics at the electrode.

Although many efforts have been made on using various coating layers on the electrodes to improve the battery performance, there is still a lack of fundamental understanding on the mechanisms that how the functional coating layer can provide the above mentioned advantages during battery operation. Particularly, the lithiation of active materials with surface coating is a complicated dynamic process that contains two dynamic systems rather than one isolated process, where inner active material core and outer surface coating layer can interact on each other. Upon lithium insertion, both of surface coating layer and active material core undergo volume expansion and phase transformation. On the one hand, the lithiation of surface layer solely can thicken the coating layer due to the lithiation-induced volume expansion; On the other hand, the expansion of the inner core upon lithiation will stretch the surface layer, resulting in thinning the coating layer like blowing a balloon. At the same time, the surface coating layer can provide a compressive stress on the inner core, and suppress its volume expansion. In other words, the surface coating layer will experience thickening process and thinning process simultaneously, which are both time dependent. In addition, the mechanical property of the surface coating layer is also time dependent, which can vary as the Li concentration in this layer changes. It can be expected that the surface layer will crack when the strain generated from the expansion of the inner core exceeds the critical fracture strain of the surface layer at that specific phase. Thus, the evolution of the surface coating layer is a dynamic system which experiences two opposite processes, i.e. the intrinsic expansion from the Li insertion as well as the external stretch from the expansion of inner core simultaneously. Such dynamic interplay between the inner active material and surface coating layer will lead to a time and lithiation-level dependent fracture property of the coating layer, as well as its fracture response, which is key to understand the functions of the surface coating and determine the optimal coating thickness. In the following sections, we will discuss about the coupled behavior of coating with the lithiation behaviors of Si anodes of different design, namely, Si nanowire, Si nanotube, Ge/Si/Cu nanowire and Si nanoparticle.

2.1.3 Lithiation of c-Si nanowires with SiO_2 coating

In this work, we systematically investigated the lithiation process of Si nanowires coated with SiO_2 layers of different thicknesses, using the in-situ transmission electron microscopy (TEM) electrochemistry experiments and chemomechanical modeling. With the help of TEM, the structural evolution and phase transformation of SiO_2 coated Si nanowires (NWs) were monitored at high spatial resolution in real time. Particularly, we focused on the concurrent dynamic processes of lithiation of Si core and SiO_2 surface layer. Time-dependent thickening and thinning as well as fracture of the surface coating layers with different thicknesses were observed. It was found that surface coating of about 7 nm SiO_2 on Si nanowire has the minimum mechanical issue, which is consistent with the ex-situ electrochemical results.[38] Surprisingly, the lithiation of SiO_2 coating underwent a mechanical transition from pristine brittle SiO_2 to more ductile lithiated layer. These observations, in combination with the chemomechanical modeling, can directly reveal the concurrent processes of lithiation of the core and coating layer, suggest the optimal coating thickness, and provide important insights into the design of battery electrodes with functional surface coatings.

The [111]-oriented Si NWs were epitaxially grown on a Si (111) wafer, and a uniform SiO_2 layer was formed after thermal annealing at 700℃ for 10 minutes under atmosphere. The advantage of using [111]-oriented Si NW for the purpose of this work is the almost symmetrical volume expansion of [111] Si NW in the radial direction during lithiation, which avoids the large difference in stress distribution in the [112]-oriented Si NW, originated from the anisotropic expansion in Si[4, 91, 104] . Upon applying a -2 V potential on the Si/SiO2 NW working electrode against the Li electrode, Li ion transport took place along the surface of the NW. Lithiation was initiated from the surface into the bulk as Li ion diffused from the surface inwards. As a result, the surface SiO2 layer was lithiated first prior to the lithiation of Si core, as evidenced by the thickening of the surface layer of 7 nm and 11 nm (Figure 2.1d and Figure 2.1h). This gradual increasing in volume indicates that the Li content in the surface layer can gradually increase with lithiation process, i.e. this process is time dependent.

After the surface SiO2 layer was partially lithiated, the lithium diffused through the surface lithiated layer and reacted with the Si core, which converted the crystalline Si to amorphous LixSi with a gray contrast, as confirmed by the electron diffraction patterns (EDP) shown in Figure 2.1b and 2.1f. The sharp interface between the crystalline Si and amorphous LixSi indicates the two-phase lithiation mechanism and allows the precise measurements on the thickness evolution of different layers. Similar lithiation process (i.e. surface layer first, then inner core) was also observed in the Al NW with native Al2O3 surface coating,105 indicating the surface diffusion inwards lithiation behavior is common for functional surface coatings on active materials, except for the recent finding of converting the surface inwards radial lithiation to axial lithiation behavior by introducing a chemical potential barrier on the surface.106

Different thicknesses of SiO2 surface layers can be obtained by controlling the thermal oxidation temperature and annealing time. In order to investigate the optimal thickness of SiO2 coating on Si anode, the lithiation kinetics of Si/SiO2 NWs with different thicknesses of surface SiO2 (native 2.5nm, 7 nm, 11 nm, 15 nm and 40 nm) were further studied. Here only 7nm and 11 nm cases are investigated. The changes of total diameter, unlithiated Si core diameter, thickness of LixSi layer and thickness of surface coating layer were obtained by monitoring the morphological changes of the NWs, and were plotted as a function of time shown in Figure 2.2(d, h). As the lithiation reaction converting the c-Si to a-LixSi, the total NW diameter increased and the diameter of unlithiated Si core decreased. It is interesting to notice that the slope of the black curve (i.e. the first order derivative) in Figure 2.1d became smaller with the time, indicating the radial lithiation rate became slower and eventually close to zero, which exhibits the self-limited lithiation behavior originated from the retardation effect of the lithiation-induced stress.89, 107 The graphs corresponding to other thicknesses of SiO2 coating layers (Figure 2.1h) also show the similar trend, indicating the robustness of the self-limited lithiation effect, regardless of the coating thickness. By comparing the incubation time as shown in Figure 2.1d and 2.1h, we can see that Si anode with 11 nm SiO2 coating requires more time to initialize the lithiation, which implies size effect for nanoscale coating.

Interestingly, the incubation time required to start obvious lithiation (marked by red arrows in the graphs) increased as the thickness of SiO_2 coating layer increased, which changed from ~20 s in the native 2.5 nm SiO_2 coating to ~100 s in the 7 nm coating, and then to ~150 s in the 11 nm surface coating. This phenomenon exhibits that the thicker the SiO_2 coating layer is, the larger the impedance is. Bulk SiO_2 is an insulator with large energy band gap of about 8 eV.[108] When the size decreases into nanoscale, more defects can be introduced into the thin SiO_2 layer, especially for the layer formed by thermal oxidation. These defects can create energy levels into the band gap, and in turn decrease the effective band gap, which will allow the insulating SiO_2 become electrical conductive in some degree. This can explain why the thinner SiO_2 layer is easier to get lithiated, while the thicker SiO_2 layer needs more incubation time. Actually, SiO_2 without any conductive coating is very difficult to get lithiated. It is worth mentioning that for the 40 nm SiO_2 coating case, the applied -2 V potential was not enough to initiate the lithiation of SiO_2

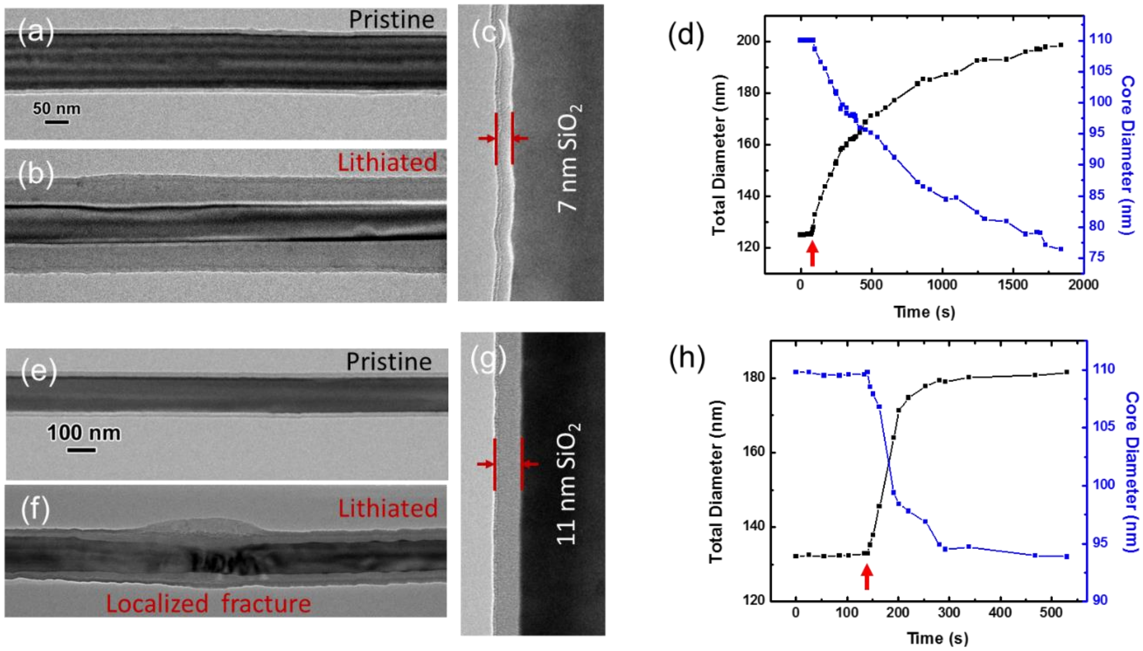

Figure 2.1 Morphological evolution of *c*-Si nanowire with coatings. (a) Pristine Si nanowire with 7 nm SiO_2 coating before lithiation. (b) Morphology of Lithiated Si. (c) A magnified view of pristine Si nanowire with 7nm SiO_2 coating. (d) Diameters of total nanowire and unlithiated Si during lithiation for 7 nm coating. (e) Pristine Si nanowire with 11 nm SiO_2 coating before lithiation. (f) Morphology of Lithiated Si, where localized fracture is observed. (h) Diameters of total nanowire and unlithiated Si during lithiatoin for 11 nm coating.

layer, which can be attributed to the higher impedance from the thicker SiO_2 surface layer. Finally, a -4 V potential against Li electrode was applied on the Si/SiO_2 (40nm) NW to initiate the lithiation process. The higher required potential compared with the thinner SiO_2 coating cases suggests that the thicker SiO_2 will introduce larger impedance and thus a larger over potential is required to lithiate the coating materials.

Due to the anisotropic volume expansion in Si (i.e. the largest volume expansion in <110> direction and the smallest volume expansion in <111> direction), stress-induced fracture was observed in [112]-orientated Si NW even with only native SiO_2 surface layer.[4] There was no fracture formation in the bulk [111]-orientated Si NWs without any intentional coating during lithiation, attributed to the almost symmetrical volume expansion of [111] Si NW in the radial direction during lithiation.[19, 107] In our experiments, for the thin SiO_2 coating (7 nm), the surface layer remained almost intact after lithiation, as shown in Figure 2.1b. Interestingly, if the thickness of surface SiO_2 coating layer increased, fracture in the Si/SiO_2 NWs were observed (Figure 2.1f). It is worth noticing that the fracture morphologies of the 11 nm and 40 nm SiO_2 coating are different. Only localized fracture (~350 nm size along the NW) was observed in the NW with 11 nm SiO_2 coating (Figure 2.1f), while the fracture in the NW with 40 nm SiO_2 coating showed global fracture, which spanned almost the whole NW (not shown). This result suggests that it will not benefit the battery performance if the surface coating layer is continuously increased, as the mechanical issue can become more severe. Thus, there should exist an optimal thickness of surface SiO_2 coating for Si anode. Our above experimental results indicate that the 7 nm SiO_2 surface coating on Si NW can give the best performance from both the mechanical and kinetic viewpoints, which is consistent with the ex-situ electrochemical result.[38]

To further study the effects of SiO_2 coatings on the lithiation of Si anode, 7nm coating case is taken as an example here for illustration. Figure 2.2 shows the dynamic evolution of SiO_2 coating thickness (Figure 2.2a) and corresponding volume expansion (Figure 2.2b). It should be noted that the dynamic evolution of SiO_2 coating thickness is totally captured by the model developed in Part 2.1.1, by assuming the lithiation of SiO_2 as diffusion control with single phase. As we see from Figure 2.2, SiO_2 experienced two opposite process simultaneously: 1) the volume expansion induced by the lithiation of the surface layer; 2) thinning effect from the stretch of the surface layer as the inner core expanded upon lithiation. Initially, the surface layer was lithiated first as the lithium insertion from the surface inwards. The thickness of surface layer was increased from pristine 7 nm to about 8.7 nm before the Si core started to lithiate. Since the lithiation of surface SiO_2 layer didn’t reach the final phase, the lithiation of this layer continued, and this layer would trend to become thicker due to the continued volume expansion (Figure 2.2c, Figure 2.2e). On the other hand, the lithium ions diffused through the surface layer and lithiated the inner Si core, resulting in the volume expansion of the Si core. This volume expansion stretched and thinned the surface layer, especially when the lithiation of SiO_2 layer stopped (Figure 2.2b, 2.2d, Figure 2.2e). Figure 2.1a-2.1b shows that no fracture or of SiO_2 over 30%, which implies the excellent ductility of fully lithiated SiO_2. stops at earlier stage than that in the case of 7 nm coating. Consequently, the thickness of coating layer continues to increase until the end, which also indicates partially lithiated. coating layer. Since pure SiO_2 is brittle and thicker coating has lower flaw tolerance than thinner

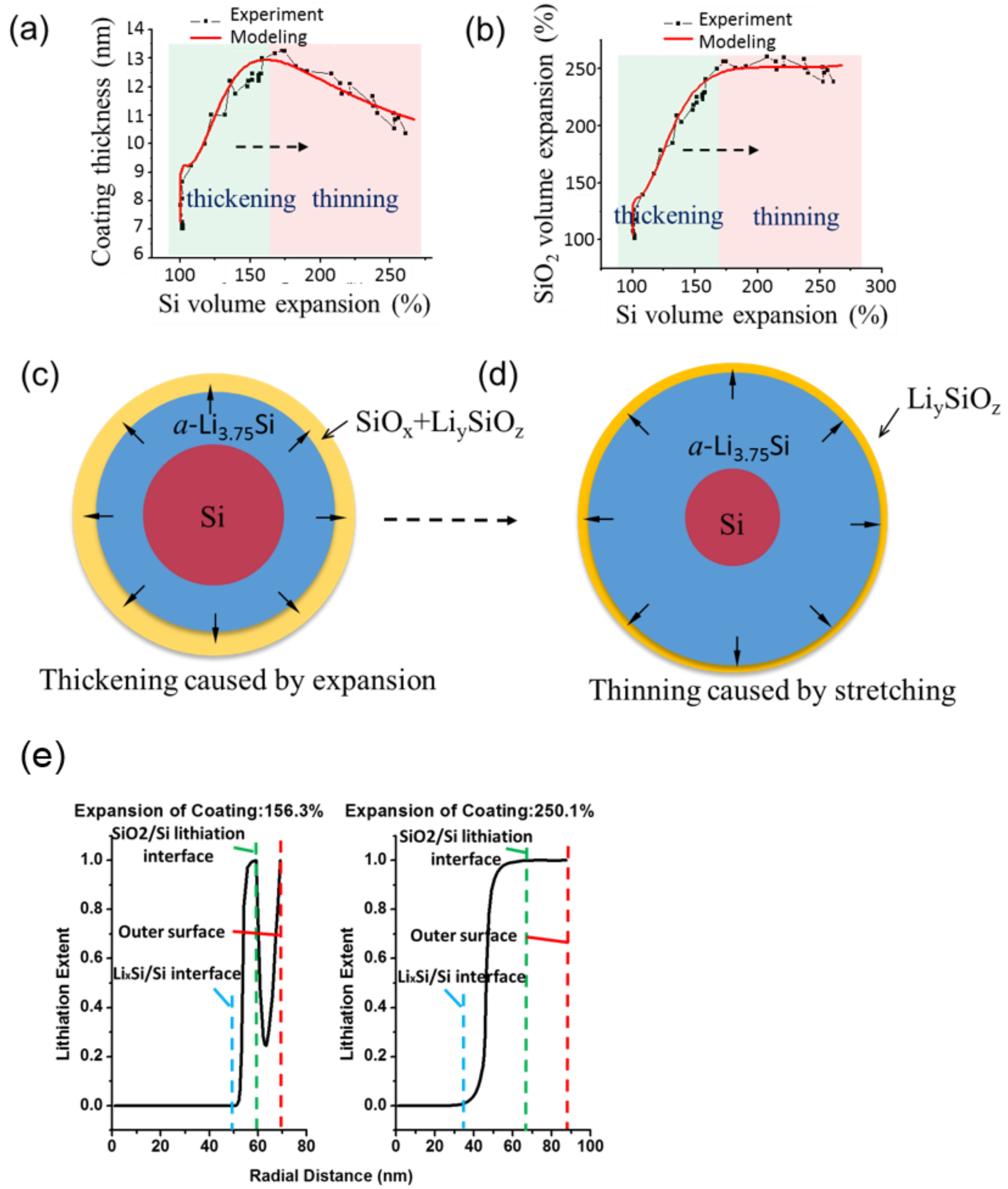

Figure 2.2 (a) Dynamic evolution of coating thickness during lithiation of Si with 7nm SiO2 coating. Coating thickens first, then thins after reaches a maximum value. (b) Volume expansion of coating during lithiation. (c) Thickening process due to expansion of coating itself. (d) Thinning process due to stretch from expanding Si after SiO_2 coating is fully lithiated. (e) Lithiation sates in both SiO_2 coating and Si core at two different lithiation stages.

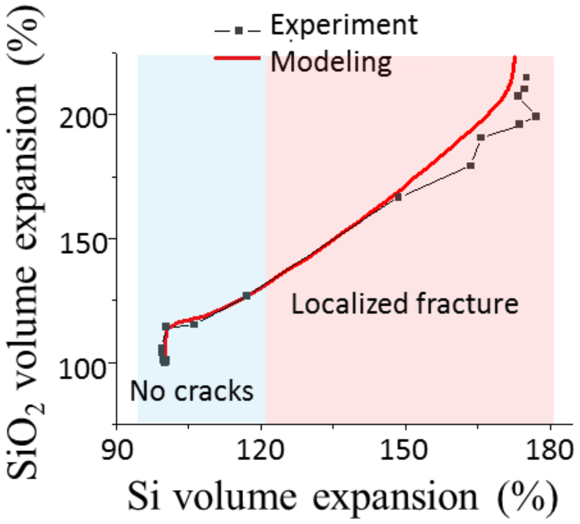

Figure 2.3 Lithiation of Si nanowire with 11 nm SiO_2 coating. The SiO_2 coating keeps expanding until fracture. With more significant stress limited effect, less Si is lithiated than the case with thinner coating.

coating, partially lithiated SiO_2 is more likely to fracture than fully lithiated SiO_2 under continuous stretch. In fact, this partial lithiation of 11 nm coating is partly attributed to the fact of it takes more time for thicker SiO_2 coating to lithiate. Therefore, lithiaition of Si nanowire would be relatively earlier in the case of thicker coating, which would then cause fracture.

The lithiation of Si/SiO_2 core/shell NW is a dynamic system, which involves the concurrent processes of lithiation of SiO_2 coating shell and Si core, as well as the interplay of their volume changes. Different from the previous reports, which mostly ignored this concurrent processes and isolated the properties of Si core with the surface SiO_2 coating, our work highlights the importance of considering the dynamic processes of the time-dependent phase transformation, mechanical properties and ionic conductivities in this system.

The phase transition of SiO_2 upon lithiation/delithiation is still controversial. Bulk SiO_2 cannot react with Li or the reaction rate is extremely slow, which is attributed to the intrinsic low electrical conductivity of SiO_2. Nano-sized SiO_2, especially these SiO_2 coated with conductive materials, can get lithiated, due to the increased electrical conductivity at nano-scale. Several lithiated products, such as Li_2O, $Li_2Si_2O_5$, Li_4SiO_4, Si and Li_xSi, were observed upon lithiation of SiO_2 in literature.[109-115] It was reported that the formation of $Li_2Si_2O_5$ and Li_xSi is reversible, while the formation of Li_4SiO_4 and Li_2O cannot be converted back to SiO_2, which contributes to the irreversible capacity loss of SiO_2-based LIBs.[114] Since the phase transformation and reaction products are reaction voltage dependent,[116] it is generally believed that the surface coating layer has mixture phases coexisted during the electrochemical lithiation of SiO_2. Recently, the in-situ TEM lithiation of pure SiO_2 thin layer on SiC NW revealed the process of phase transition to form crystalline Li_2O and Li_4SiO_4, without the evidence of $Li_2Si_2O_5$.[117] In our work, the surface layer is generally amorphous phase (except the poly-crystalline Li_2O phase), it is difficult to identify the exact phase composition at different lithiation stage. But it is believed that the Li content gradually increases during lithiation, which result in the time-dependent mechanical properties of the surface Li-Si-O layer.

Time-dependent mechanical behavior of electrochemically lithiated Si was recently studied by Zinn *et al*.[118] and Berla *et al*.[119] It was found that Young's modulus and the hardness of lithiated silicon decrease with increasing Li content, as the addition of Li to Si has an effect of elastic and plastic softening. Similarly, we believe that the addition of Li to SiO_2 can soften SiO_2 as well, as evidenced by the observed brittle to ductile transition of pristine SiO_2 upon lithiation. This observation is consistent with the modeling that found both the strength and elastic modulus significantly decrease with the increasing of Li concentration. Considering this time-dependent mechanical behavior of electrochemically lithiated SiO_2 is critically important in understanding the mechanical responses of the coating layers with different thicknesses. It is crucial for the surface layer to become soft enough before the accumulated strain from the volume expansion of inner core during lithiation reaches its critical fracture strain, in order to keep the intact of the surface coating. From the in-situ TEM observation, we found that 7 nm SiO_2 coating layer is the optimal thickness to keep the integrity of electrode. This in-situ result is in agreement with the ex-situ result showing that 7 nm SiO_2 surface coating gave the best electrochemical performance.[38]

Besides the mechanical viewpoint, Li ion conductivity of the surface coating layer is another important factor in achieving a high performance LIB. Various lithiated Li-Si-O structures can be formed upon lithiation of SiO_2 layer, inside which the Li ion diffusion can be controlled by Li vacancy hopping.[116] It was reported that the migration barriers decrease with increasing Li_2O concentration in lithium silicate glasses.[120] Particularly, Li_4SiO_4 is a good Li ionic conductor,[121] while the crystal structure of $Li_2Si_2O_5$ exhibits open tunnel along the c-axis,[122] which could also provide facile diffusion paths for Li ions. Thus, it is suggested that the Li-Si-O layer is susceptible to the diffusion of Li ions.

In summary, this work presents an in-situ TEM study of lithiation of Si NWs with different thicknesses of surface SiO_2 layers. Thickening of the surface layer upon Li ion insertion and thinning of the same layer under the volume expansion of lithiated Si core were observed. The overall thickness change of this layer (i.e. whether increasing or decreasing) is determined by the combination of the two effects. The concurrent processes indicate that the mechanical property and fracture response of the surface layer are time-dependent and lithiation-level (i.e. Li-content in this Li-Si-O layer) dependent. It was observed that 7 nm SiO_2 coating layer is the optimal thickness to keep the integrity of the Si/SiO_2 NW electrode. Our results not only provide the understanding of the mechanical properties and deformation behavior of lithiated SiO_2, but also shed lights on the optimum design of the surface coating on active materials.

2.1.4 Lithiation of a-Si nanotube with SiO_2 coating (Reprinted with permission from Ref.[123]. Copyright 2016 American Chemical Society)

Recently, Si-based anodes with hollow structures, including nanotubes[42, 124], porous nanowires and nanoparticles[125-127], have attracted a great deal of interest in the development of high-performance LIBs. The free space inside these hollow structures is expected to accommodate the volume change and thus reduce the outward expansion, so as to mitigate the degradation of Si nanostructures and SEI. However, the actual structure change and degradation of these hollow Si nanostructures during electrochemical cycling remain largely unexplored. On the other hand, surface coatings have been widely applied to the hollow Si nanostructures for constraining the volume expansion and/or serving as the artificial SEI[42, 128]. Among the various coatings, silicon oxide (SiO_x) has gained considerable interest for Si-based anodes due to easy fabrication via thermal treatment[37, 38, 42, 124, 129-131]. The SiO_x coating could mechanically confine the outward expansion of Si-based hollow structures and reduce the fracture of SEI, leading to an improved battery performance[42, 124]. However, it is still unclear to what degree the volume expansion of Si-based hollow nanostructures can be confined by the surface SiO_x layers, and whether or not the lithiation mechanism of Si nanostructures remain unchanged with the application of surface coatings. A clear understanding on the lithiation behavior of hollow nanostructures with surface coatings is critically important for the development of durable high-performance LIBs. To this end, the amorphous Si (*a*-Si) nanotubes with surface SiO_x layers provide a clean system to address the above questions.

In this work, we perform an *in situ* TEM study on the electrochemical lithiation behavior of individual *a*-Si nanotubes with different thicknesses of surface SiO_x layers. The *in situ* TEM experiment allows for a direct observation of the real-time lithiation process, as well as a precise measurement of geometrical changes during lithiation of *a*-Si nanotubes. Surprisingly, we find that no inward expansion occurred after the full lithiation of *a*-Si nanotubes with native oxides. Moreover, we show that increasing the thickness of SiO_x at the outer surface can facilitate mechanical confinement on the lithiated *a*-Si nanotubes, resulting in inward expansion. However, the SiO_x coating on the inner surface can serve as a mechanical barrier to hinder inward expansion. Furthermore, we discover that the sandwich lithiation mechanism and two-stage lithiation process of *a*-Si nanotubes remained unchanged with the increasing thickness of surface coatings. In addition, our chemomechanical modeling reveals the mechanistic origin of geometrical changes in the lithiated *a*-Si nanotubes, highlighting the critical role of anisotropy of lithiation-induced chemical strains.

Figure 2.4 shows the *in situ* TEM results of electrochemical lithiation in an *a*-Si nanotube with native oxides. Prior to lithiation, the inner and outer diameters of the *a*-Si nanotube were 330 and 280 nm, respectively (Figure 2.4a). Both the inner and outer surfaces were covered with a thin layer of native oxide, with thickness less than 2 nm

(Figure 2.4b). By applying a -3 V potential, lithiation first initiated from the outer surface and proceeded radially by inward movement of a sharp interface that separated the dark *a*-Si reactant with the light-gray amorphous Li_xSi (*a*-Li_xSi) product, indicating the operation of a two-phase mechanism of lithiation. After a while, a radial lithiation also started from the inner surface and proceeded by outward movement of a two-phase boundary (Figure 2.4d). As a result, *a*-Li_xSi alloys formed on both the outer and inner surfaces, yielding a sandwich structure of *a*-Li_xSi/*a*-Si/*a*-Li_xSi (Figure 2.4d). This is consistent with the previous TEM observation of sandwich lithiation in an *a*-Si layer coated on a carbon nanofiber[132]. It is also interesting to note that the lithiation of the *a*-Si nanotube is a two-stage process[92]. That is, after the first-stage sandwich lithiation completely consumed the *a*-Si layer, the resulting volume expansion was only ~ 172% (Figure 2.4e), suggesting the formation of an intermediate *a*-Li_xSi phase with $x \approx 2.3$. During the second-stage lithiation, the *a*-Li_xSi phase was further lithiated without a visible interface, indicating the operation of a single-phase mechanism of lithiation. At the end of the second-stage lithiation, the inner and outer diameters of the lithiated *a*-Si nanotube were 282 and 433 nm, respectively (Figure 2.4f). The corresponding volume expansion (relative to *a*-Si) was ~ 254%, close to the theoretical value (~ 270%) for the $Li_{15}Si_4$ phase. Figure 2.4c presents the inner (d_1) and outer (d_4) diameters of the lithiated *a*-Si nanotube as a function of time, which further corroborates the two-stage lithiation occurring in *a*-Si. It is seen that during the first-stage lithiation, the outer diameter d_4 increased significantly, while the inner diameter d_1 remained nearly constant. During the second-stage lithiation, d_4 kept unchanged for some time and then increased drastically, from 403 nm to 433 nm; meanwhile, d_1 still remained nearly constant. The two-stage lithiation of *a*-Si has been previously shown to have a significant impact on the morphological changes in lithiated *a*-Si electrodes[92]. In this work, we further study the effects of oxide thickness on the lithiation behavior of *a*-Si nanotubes.

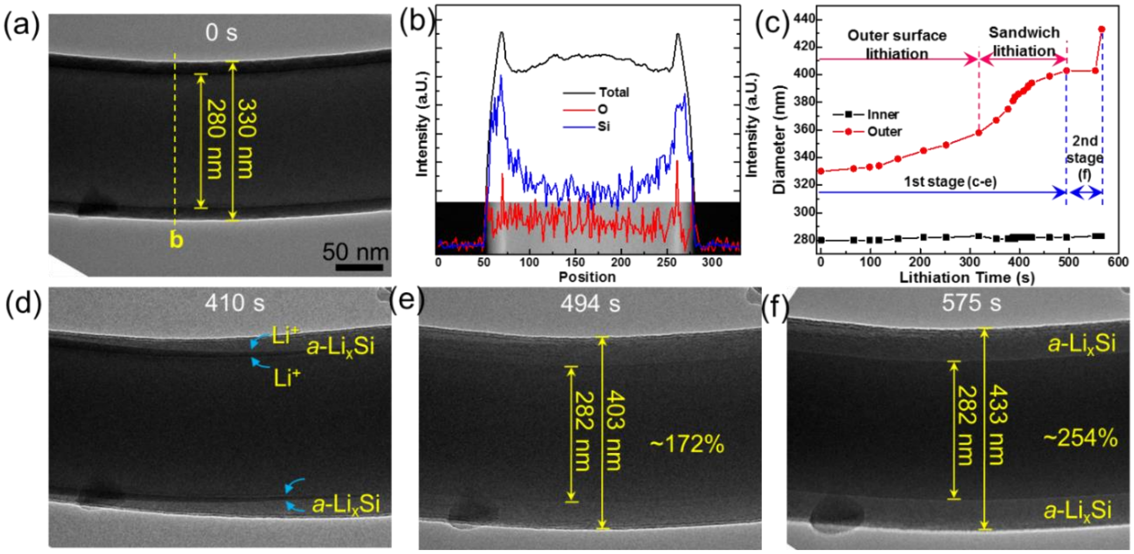

Figure 2.4. Lithiation of an *a*-Si nanotube with native oxide layers. (a) Pristine *a*-Si nanotube with native oxide layers, with inner and outer diameters of 330 and 280 nm, respectively. (b) The line scanning profile showing the element distributions along the radial direction of *a*-Si nanotube. The native oxide layers on both the inner and outer surfaces are less than 2 nm. (c) The lithiation kinetics of this *a*-Si nanotube, showing the evolutions of its outer (d_4) and inner (d_1) diameters as a function of the lithiation time. (d-f) The lithiation process of the *a*-Si nanotube with native oxide layers. A sandwiched lithiation structure of *a*-Li$_x$Si/*a*-Si/*a*-Li$_x$Si formed due to the lithiation from both inner and outer surfaces. No inward expansion was observed after the full lithiation.

The lack of inward expansion is entirely unexpected during the sandwich lithiation of *a*-Si nanotubes. This is because once lithiation started from the inner surface, both the lithiation product of *a*-Li$_{2.3}$Si near the outer surface and the unlithiated *a*-Si in the mid-layer would mechanically confine the lithiation-induced volume expansion near the inner surface, so that inward expansion is expected to occur to some degree. However, in eight *a*-Si nanotube samples studied in this work, no inward expansion was observed during the whole lithiation process. Moreover, the lack of inward expansion was also observed upon

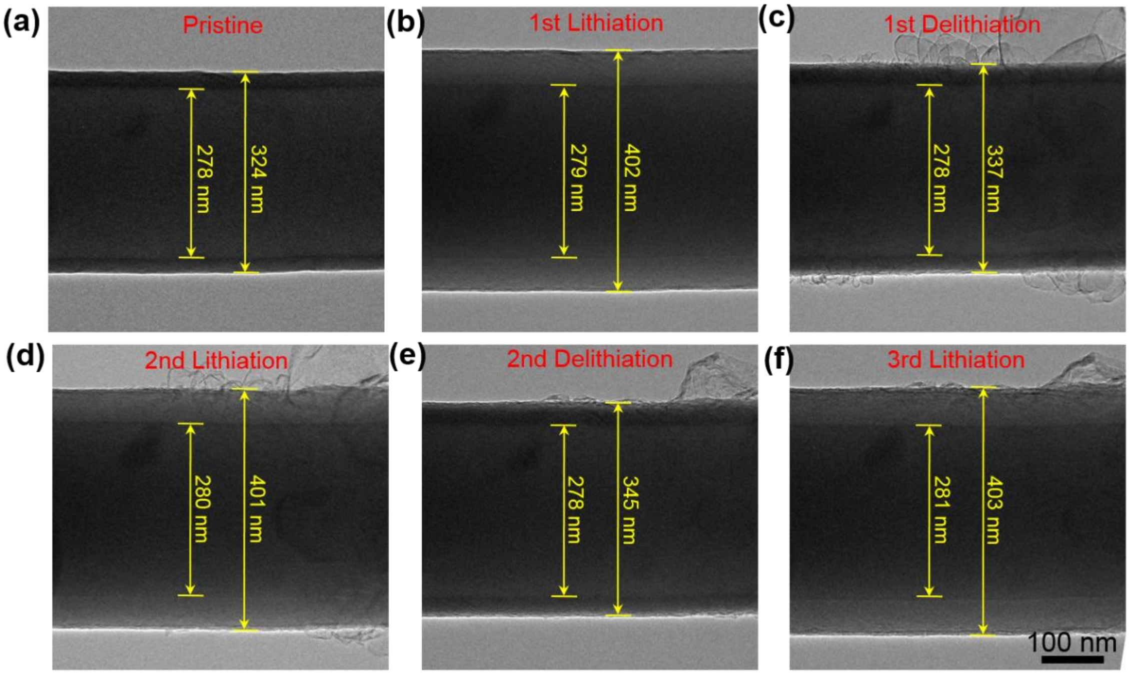

(a)
Pristine
278 nm
324 nm
(b)
1st Lithiation
279 nm
402 nm
(c)
1st Delithiation
278 nm
337 nm
(d)
2nd Lithiation
280 nm
401 nm
(e)
2nd Delithiation
278 nm
345 nm
(f)
3rd Lithiation
281 nm
403 nm
100 nm

Figure 2.5. Structural evolution of an *a*-Si nanotube with native oxides during lithiation and delithiation cycling. Reversible volumetric changes occurred during three cycles of lithiation and delithiation, without any inward expansion at the inner surface of the nanotube.

electrochemical cycling of *a*-Si nanotubes that produced reversible volumetric changes. As shown in Figure 2.5, no inward expansion occurred during three cycles of lithiation-delithiation in an *a*-Si nanotube with native oxides. Besides, significant volume expansions were also observed after lithiation of Si anodes with other hollow structures, such as porous Si nanowires and nanoparticles (Figure 2.6). Hence, understanding the origin of geometrical changes in *a*-Si nanotubes, particularly regarding to the lack of inward expansion, could have important implications for the application of hollow Si nanostructures.

To clarify the origin of lack of inward expansion in the lithiated *a*-Si nanotube, we develop a chemomechanical model to simulate the two-stage lithiation process in the nanotube, by taking into account the sandwich, two-phase lithiation during the first stage and the single-phase lithiation during the second stage. Figure 2.7a shows the setup of our 2D model, representing the cross section of an *a*-Si nanotube before lithiation. To reveal the dominant physical effect, here we neglect the thin layers of native oxides on the inner and outer surfaces of the nanotube. Figure 2.7b presents a schematic illustration of our

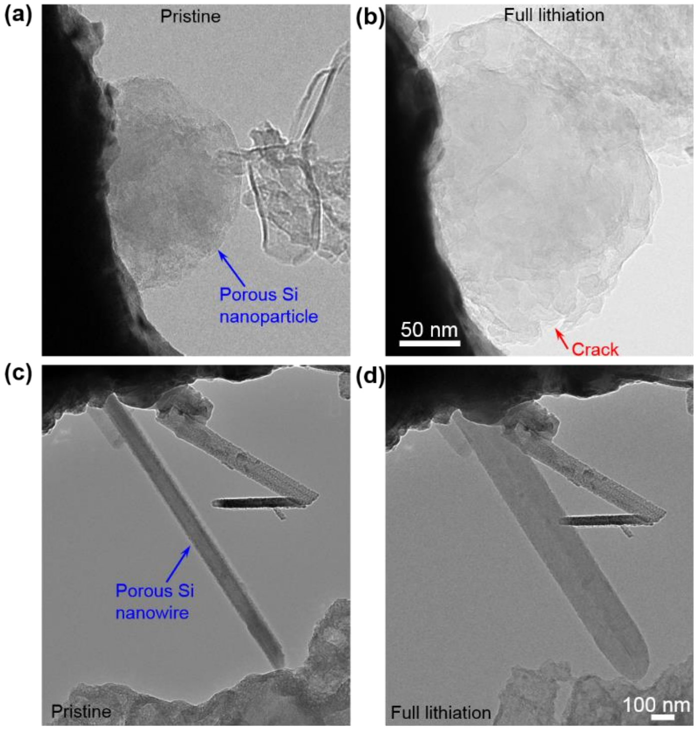
(a)
Pristine
Porous Si nanoparticle
(b)
Full lithiation
50 nm
Crack
(c)
Porous Si nanowire
Pristine
(d)
Full lithiation
100 nm

Figure 2.6 Significant volume expansion occurred after the lithiation of porous Si nanoparticles (a-b) and nanowires (c-d)

model during the first-stage lithiation, featuring a sandwich, two-phase process. To simulate this first-stage lithiation, we solved the non-linear diffusion equation with a lithium diffusivity depending on the local lithium concentration[4, 133]; in addition, we prescribed a saturated lithium concentration (corresponding to the product phase of *a*-$Li_{2.3}Si$) as the boundary condition at both the outer and inner surfaces of the nanotube, considering the fact that lithium diffusion is much faster on the surface than in the bulk of Si. Then we also simulated the second stage of single-phase lithiation by tuning the lithium concentration-dependent diffusivity[133]. To simulate the lithiation-induced deformation, we employed a rate formulation of the chemo-elastic-plastic constitutive relations[133], which is necessary to characterize the large strains involved during lithiation. In this formulation, the total strain rate $\dot{\varepsilon}_{ij}$, is taken to be the sum of three contributions, $\dot{\varepsilon}_{ij} = \dot{\varepsilon}_{ij}^{c} + \dot{\varepsilon}_{ij}^{e} + \dot{\varepsilon}_{ij}^{p}$. Here $\dot{\varepsilon}_{ij}^{c}$ is the rate of the lithiation-induced chemical strain and it is proportional to the rate of the normalized lithium concentration $\dot{c}$, $\dot{\varepsilon}_{ij}^{c} = \beta_{ij}\dot{c}$, where β_{ij} is the lithiation expansion coefficient and c varies between 0 (*a*-Si) and 1 (lithiation product $Li_{3.75}Si$); $\dot{\varepsilon}_{ij}^{e}$ is the elastic strain rate; and $\dot{\varepsilon}_{ij}^{p}$ is the plastic strain rate. The detailed material parameters are given in the Methods. In our simulations, the plane-strain condition was imposed, on the basis of TEM observation of negligible axial elongation during the entire lithiation process.

Figure 2.7c shows the simulation results of geometrical changes in the lithiated *a*-Si nanotube as a function of reduced time (t*), which are in close agreement with experimental measurements (*i.e.*, symbols in Figure 3c). Our chemomechanical simulations provide key insights into the origin of lack of inward expansion in the lithiated *a*-Si nanotube. That is, the anisotropy of lithiation-induced chemical strains critically governs the geometrical changes in lithiated *a*-Si nanotubes. While one tends to assign the isotropic volume expansion with associated isotropic chemical strains (*i.e.*, isotropic β_{ij}) to a lithiation process of *a*-Si, the geometrical constraints within the tube cross section on lithiation cause a symmetry breaking in the radial and hoop directions of the nanotube, resulting in a strong anisotropy in the chemical strains of lithiation. As shown by Hsueh and Evans[134], Huang *et al.*[133], and Liang *et al.*[135], the degree of anisotropy of chemical strains dictates the resulting elastic-plastic deformation, particularly regarding the outward versus inward radial displacement, in a structure with the curved geometry such as a cylindrical wire or spherical particle. As a result, the chemical strains with a large hoop component can produce the outward radial displacement at both the inner and outer surface of the nanotube, owing to the larger perimeter in the hoop direction at a larger radial distance. In contrast, the chemical strains with a large radial component can result in the inward displacement at the inner surface and the outward displacement at the outer surface for the nanotube, thus giving a balanced hoop tension and compression in the system. In the present study, we assigned the anisotropic chemical strains (see Methods), such that the modeling results agree closely with experimental measurements for both the first stage of two-phase lithiation and the second stage of single-phase lithiation. Hence, our chemomechanical model suggests that the lack of inward expansion at the inner surface of the lithiated *a*-Si nanotube with native oxides can be attributed to the anisotropic nature of lithiation-induced chemical strains in the curved configuration of a nanotube.

We next studied the effect of mechanical confinement from thick oxides by *in situ* TEM experiments, in order to examine to what extent the geometrical changes and particularly lithiation-induced outward expansion at the outer surface of the nanotube can be confined by coatings. Understanding the mechanical confinement of thick SiO_x coatings has practical implications for stabilizing the SEI as well as other types of coatings on the surface of nanotubes, so as to mitigate mechanical degradation and capacity fade in LIBs. In our experiments, the thickness of SiO_x layers can be controlled via thermal treatment of *a*-Si nanotubes in atmosphere for different durations. In order to clearly characterize the geometry of the nanotube with inner and outer oxide coatings, here we define the diameters of d_1, d_2, d_3 and d_4, respectively (Figure 2.8a), which involve the inner surface, the interface

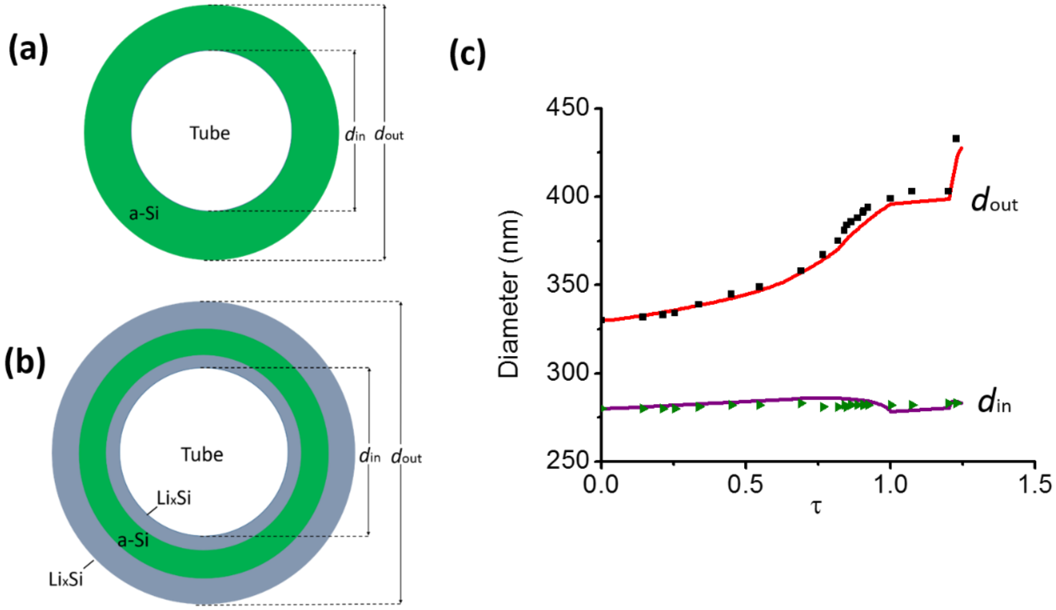

Figure 2.7. Chemomechanical modeling of the lithiation dynamics in an *a*-Si nanotube with native oxide. (a) Schematic of the model representing the cross section of an *a*-Si nanotube before lithiation. (b) Formation of a sandwich structure of *a*-Li_xSi/*a*-Si/*a*-Li_xSi during the first-stage lithiation. The inner and outer diameters of the *a*-Si nanotube are donated as d_1 and d_4, respectively. (c) Comparison between the experimental and simulation results of d_1 and d_4 as a function of reduced time t* during the two-stage lithiation. The reduced time t* is defined as the lithiation time normalized by the duration of the first-stage lithiation.

between the inner SiO_x and *a*-Si layers, the interface between the outer SiO_x and *a*-Si layers, and the outer surface. Figure 2.8b-f shows the lithiation behavior of an *a*-Si nanotube with 3 nm and 4 nm SiO_x on the inner and outer surfaces of the nanotube, respectively, which was obtained after oxidization in atmosphere at 500 ^{o}C for 1 hour (Figure 2.8b). This system is donated as 3‖4 nm $SiO_x/Si/SiO_x$ nanotube. Note that the inner surface layer of SiO_x is slightly thinner than the outer surface layer. This could be attributed to the higher hoop compression in the inner layer induced by oxidation than in the outer layer, causing the slower oxidation kinetics in the former. Figure 2.8c-f shows the lithiation process of the 3‖4 nm $SiO_x/Si/SiO_x$ nanotube. Before lithiation, the four diameters were 220 nm, 226 nm, 261 nm and 269 nm, respectively. The lithiation first initiated from the outer surface and then started from the inner surface, leading to a sandwich structure (Figure 2.8d), in consistent with the *a*-Si nanotube with native oxides (Figure 2.4). Moreover, lithiation of this 3‖4 nm $SiO_x/Si/SiO_x$ nanotube also proceeded by a two-stage process, as shown by Figure 2.8c-f as well as by measurements of d_1 and d_4 as a function of time during lithiation in Figure 2.9. After the first-stage lithiation, d_1, d_2, d_3 and d_4 changed to 207 nm, 213 nm, 307 nm and 316 nm, respectively, with a volume expansion of ~ 187% in the *a*-Si layer (Figure 2.8e). After the second-stage lithiation, the four diameters further evolved to 204 nm, 212 nm, 323 nm and 332 nm, respectively, giving a total volume expansion of ~ 259% in the *a*-Si layer (Figure 2.8f). It is interesting to note that a pronounced inward expansion occurred at the inner surface during the lithiation of this 3‖4 nm $SiO_x/Si/SiO_x$ nanotube, as manifested by the change of d_2 from 226 nm before lithiation to 212 nm after full lithiation.

To confirm the inward expansion in nanotubes with thick oxides, we further studied the lithiation behavior of an *a*-Si nanotube with 4 nm and 6.5 nm SiO_x on the inner and outer surfaces respectively (donated as 4‖6.5 nm SiO$_x$/Si/SiO$_x$ nanotube), as shown in Figure 2.8g-i. Similar to the nanotube with native oxides (Figure 2.4-2.5) and the 3‖4 nm SiO$_x$/Si/SiO$_x$ nanotube (Figure 2.8b-f), lithiation of the 4‖6.5 nm SiO$_x$/Si/SiO$_x$ nanotube followed the same reaction pathway, *i.e.*, the sandwich lithiation mechanism and two-stage

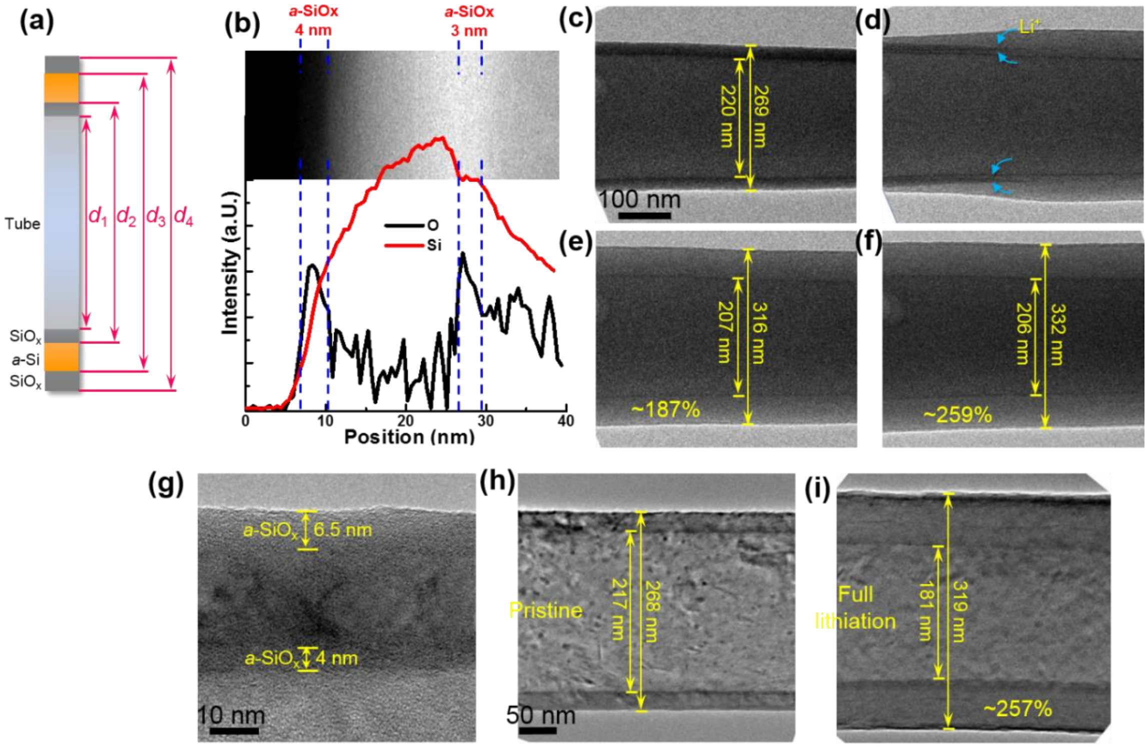
(a)
Tube
d_1
d_2
d_3
d_4
SiO$_x$
a-Si
SiO$_x$
(b)
a-SiOx
4 nm
a-SiOx
3 nm
Intensity (a.U.)
O
Si
0
10
20
30
40
Position (nm)
(c)
220 nm
269 nm
100 nm
(d)
Li$^+$
(e)
207 nm
316 nm
~187%
(f)
206 nm
332 nm
~259%
(g)
a-SiO$_x$
6.5 nm
a-SiO$_x$
4 nm
10 nm
(h)
Pristine
217 nm
268 nm
50 nm
(i)
Full
lithiation
181 nm
319 nm
~257%

Figure 2.8. Lithiation of two *a*-Si nanotubes with different thicknesses of oxide coatings. (a) Schematic of the four diameters of d_1, d_2, d_3 and d_4 in an SiO$_x$/Si/SiO$_x$ nanotube before lithiation, which involve the inner surface, the interface between the inner SiO$_x$ and *a*-Si layers, the interface between the outer SiO$_x$ and *a*-Si layers, and the outer surface, respectively. (b-f) In situ TEM lithiation of an *a*-Si nanotube with 3 nm and 4 nm SiO$_x$ on the inner and outer surfaces, respectively (donated as 3‖4 nm SiO$_x$/Si/SiO$_x$ nanotube). (b) The line scanning profile showing the thicknesses of the inner and outer SiO$_x$ layers in the SiO$_x$/Si/SiO$_x$ nanotube. (c-f) Time-lapse TEM images of lithiation of the 3‖4 nm SiO$_x$/Si/SiO$_x$ nanotube. (d) Lithiation initiated first from the outer surface and then from the inner surface, leading to a sandwich lithiation structure. (g-i) Lithiation of an *a*-Si nanotube with 4 nm and 6.5 nm SiO$_x$ on the inner and outer surfaces, respectively (donated as 4‖6.5 nm SiO$_x$/Si/SiO$_x$ nanotube). (g) High-resolution TEM (HRTEM) image showing the thicknesses of SiO$_x$ layers on the inner and outer surfaces. (h-i) TEM images of the 4‖6.5 nm SiO$_x$/Si/SiO$_x$ nanotube before and after lithiation.

lithiation process (Figure S3). It is noted that the values of d_2 for 3‖4 nm and 4‖6.5 nm $SiO_x/Si/SiO_x$ nanotubes were similar before lithiation; however, after full lithiation, d_2 decreased from 226 nm to 212 nm for the 3‖4 nm nanotube (Figure 2.8c-f), but from 225 nm to 199 nm for the 4‖6.5 nm nanotube (Figure 2.8g-i), suggesting that a more inward expansion of the inner surface occurred in the nanotube with thicker SiO_x on the outer surface. These results show that the volume expansion mode of *a*-Si nanotubes can be effectively changed by varying the thickness of surface coatings.

Previously, lithiation of Si nanotubes with the only outer SiO_x coating has been studied by *ex situ* experiments and simulations[42, 124], in which the lithiation-induced outward expansion at the outer surface of Si nanotubes was claimed to be completely confined as the thickness of surface SiO_x increased. However, continual confinement was not observed during the lithiation of $SiO_x/Si/SiO_x$ nanotubes studied here, as shown in Figure 2.10. In this case, the *a*-Si nanotubes were oxidized at 500 ^oC for 6 hours, with 6.5 nm and 9 nm SiO_x layers formed on the inner and outer surfaces respectively (donated as 6.5‖9 nm $SiO_x/Si/SiO_x$ nanotube, Figure 5b). During *in situ* TEM experiment, a high voltage (~ 20 V) had to be applied to initiate the lithiation, indicating that the thicker SiO_x coating becomes less conductive to electrons and/or lithium ions. During lithiation, the outer SiO_x layer was first lithiated, accompanied by a thickness increase from 9 nm to 12 nm (Figure 2.10d). This process led to an outward expansion at the outer surface of this nanotube. Finally, a concurrent lithiation process occurred in the Si/SiO_x system, i.e. both the outer and inner SiO_x layers were lithiated, and their thicknesses reached to 14 nm and 10 nm respectively after full lithiation (Figure 2.10c); meanwhile, a sandwich structure formed during the first-stage lithiation of the *a*-Si layer, which was followed by the second-

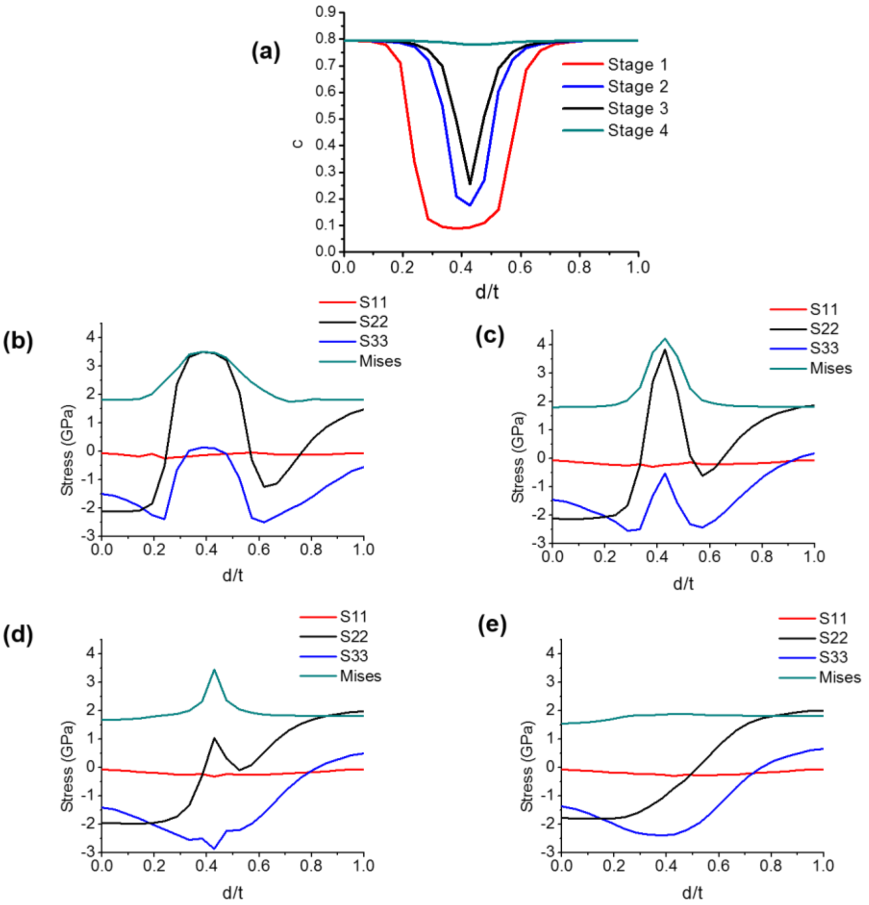

Figure 2.9. Chemomechanical simulation results of the sandwich two-phase lithiation in an a-Si nanotube, after lithiation starts at the inner surface. (a) Radial distribution of the normalized Li concentration c (i.e., Li2.3Si corresponds to c = 0.8) at four characteristic stages. The symbol of d denotes the distance from the inner surface of the nanotube, and t is the thickness of the nanotube wall. (b-e) Corresponding radial distributions of stresses at four stages, S11 and S22 are respectively the radial and hoop stress in the cross section, and S33 is the axial stress in the nanotube. All the distributions are plotted on the undeformed configuration using ABAQUS, so as to facilitate comparison between different stages.

stage lithiation of the *a*-Li$_x$Si phase resulting in a total volume expansion of ~220% for *a*-Si (Figure 2.10e-f). After full lithiation, the diameters d_1, d_2, d_3 and d_4 changed to 175 nm, 195 nm, 278 nm and 305 nm, respectively, as opposed to 187 nm, 202 nm, 231 nm and 249 nm before lithiation. A limited inward expansion occurred at the inner surface after the lithiation of 6.5‖9 nm nanotube (Figure 2.10a-f). This result implies that the inner SiO_x layer of SiO_x/Si/SiO_x nanotube can serve as a mechanical barrier to hinder the inward expansion of the *a*-Si layer. The hindrance effect increases significantly with the thickness of inner SiO_x layer. Thus, the inner SiO_x layer should be minimized during fabrication, so as to enable an effective mechanical confinement from the SiO_x coating at the outer surface of the nanotube. To quantify the confinement effect of the outer SiO_x layer on lithiation of *a*-Si nanotubes, the percentage contributions of inward and outward expansions to the total volume increase of the fully-lithiated *a*-Li_xSi alloy were further calculated based on the measured diameter changes after lithiation. The oxide layers were excluded from this calculation. After lithiation, the contribution of outward expansion can be calculated by $[(d_3^L/2)^2 - (d_3^I/2)^2]/[(d_3^L/2)^2 - (d_2^L/2)^2] \times 100\%$, and the contribution of inward expansion by $[(d_2^I/2)^2 - (d_2^L/2)^2]/[(d_3^L/2)^2 - (d_2^L/2)^2] \times 100\%$, where d_2^I and d_3^I respectively denote the values of d_2 and d_3 before lithiation, d_2^L and d_3^L after full lithiation; while the volumetric contribution from the initial *a*-Si layer is nearly a constant, with a theoretical value of 27% ($[V_{a-Si}/V_{Li_{3.75}Si}] \times 100\%$, where V_{a-Si} and $V_{Li_{3.75}Si}$ are the volumes of *a*-Si and $Li_{3.75}Si$ phase, respectively). The results are plotted in Figure 2.10g, which shows that the confinement effect on outward expansion (represented by the decreasing red curve and increasing black curve) can increase markedly with the increasing thickness of the outer SiO_x layer, and the maximal confinement is achieved in *a*-Si nanotubes with the 6.5 nm outer SiO_x layer. However, a transition occurs as the thickness of the outer SiO_x layer further increases, due to the increasing hindrance effect of the thicker inner SiO_x layer.

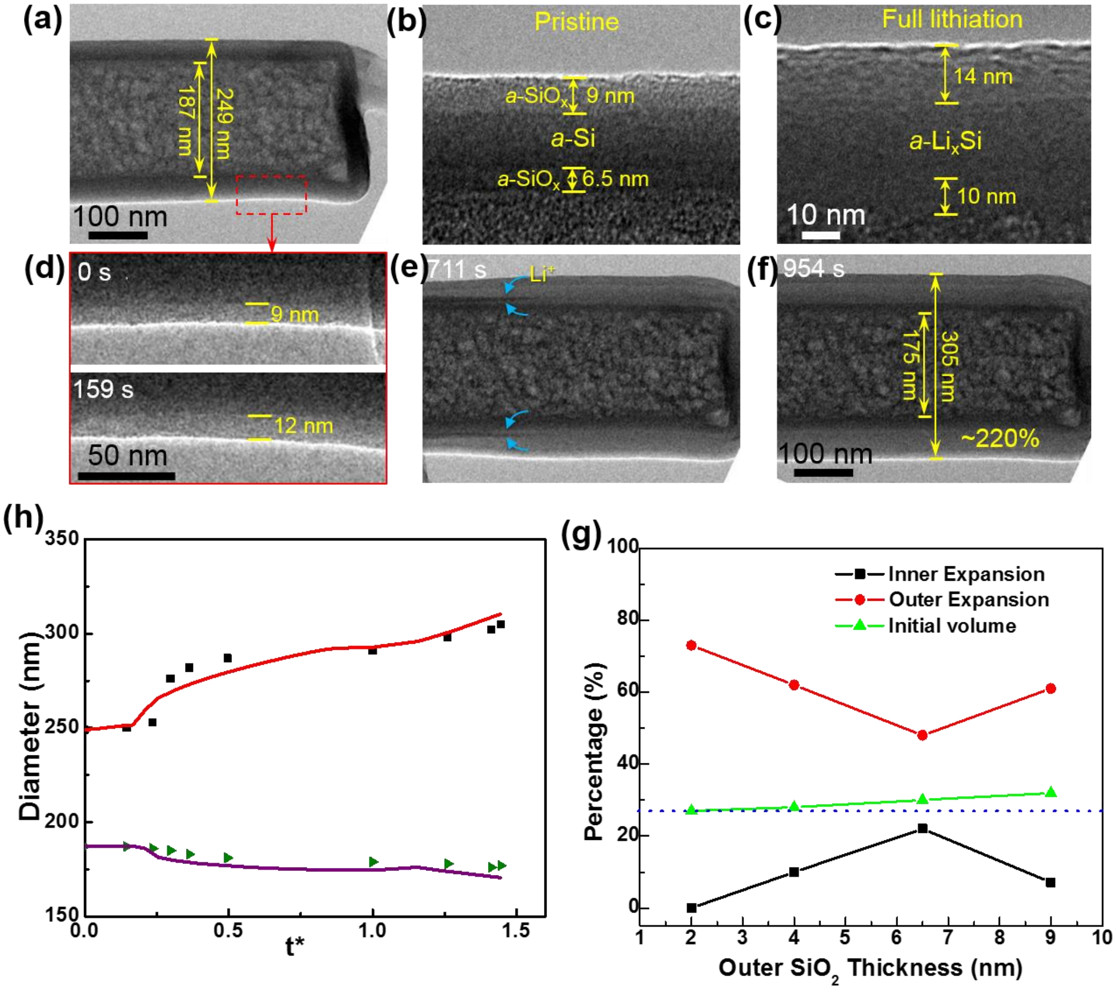

Figure 2.10. Lithiation of an *a*-Si nanotube with oxide coatings thicker than those in Figure 2.8. (a) The pristine 6.5‖9 nm SiO_x/Si/SiO_x nanotube. (b) HRTEM image showing the thickness of the inner and outer SiO_x layers before lithiation. (c) HRTEM image showing the thickness of the lithiated inner and outer SiO_x layers after full lithiation. (d) The outer SiO_x layer was first lithiated, accompanied by a thickness increase from 9 nm to 12 nm. (e-f) TEM images showing the first-stage lithiation, resulting in a sandwich lithiation structure, and the second-stage lithiation, resulting in a total volume expansion of ~ 220% (relative to *a*-Si).

Moreover, these results indicate that a more inward expansion at the inner surface could be achieved in each case if there was no SiO_x on the inner surface. Based on the chemomechanical model described earlier, we further perform simulations to understand the mechanical confinement effect of thick oxides by considering the case of 6.5‖9 nm

$SiO_x/Si/SiO_x$ nanotube. Here our model accounted for the sandwich lithiation mechanism and two-stage lithiation process, as well as the lithiation of SiO_x at both the outer and inner surfaces. We used the experimentally measured value of lithiation-induced volume expansion in SiO_x (~ 82%), which is much smaller than that of *a*-Si (~ 270%). Figure 2.10h shows the modeling results of both the outer and inner diameters of the $SiO_x/Si/SiO_x$ nanotube as a function of time, which are in close agreement with the experimental measurements (*i.e.*, symbols in Figure 2.10h). Hence, our chemomechanical modeling provides a direct support to experimental observations; namely, the lithiated thick SiO_x layer can effectively impose mechanical constraints so as to reduce the outward expansion at the outer surface and correspondingly produce the inward expansion at the inner surface in lithiated $SiO_x/Si/SiO_x$ nanotubes.

To summarize, our *in situ* TEM experiments have revealed the lithiation behaviors of individual *a*-Si nanotubes with different thicknesses of surface oxide layers. The results confirmed the earlier observation of a two-stage lithiation process in *a*-Si, involving the sandwich, two-phase lithiation during the first stage and the single-phase lithiation during the second stage. More importantly, the real-time, high-resolution TEM imaging enables a precise measurement of geometrical changes during lithiation of *a*-Si nanotubes. Our results unambiguously show that the outward expansion at the outer surface of the lithiated *a*-Si nanotubes can be effectively confined by increasing the thickness of the outer SiO_x coating; minimizing the thickness of the inner SiO_x coating can facilitate a more effective confinement by the outer SiO_x coating. Revealing such a mechanical confinement effect has practical implications for stabilizing the SEI and other types of coatings on the nanotube surface, so as to mitigate the mechanical degradation and associated capacity fade in LIBs. Moreover, our *in situ* experimental and modeling results provide new insights for the design of Si-based hollow anodes as follows. Firstly, the lithiation-induced volume expansion (*i.e.*, outward expansion at the outer surface) and resultant mechanical degradation of Si-based anodes can hardly to be fully alleviated in hollow structures, due to the anisotropic nature of chemical lithiaion strains in curved tubes and particles. This has been demonstrated by the lithiation behaviors of *a*-Si nanotubes shown in Figures 2.4 and 2.5 as well as porous Si nanowires and nanoparticles in Figure 2.6. Secondly, for hollow structures with the active surface coatings, such as SiO_2[37, 38, 42, 124, 129-131], Al_2O_3[128] and carbon[136-138], the lithiation-induced outward expansion cannot be fully constrained due to the fact that lithiation of the active surface coatings usually occurs before that of active Si, thereby resulting in outward expansion (Figure 2.8 and Figure 2.10). This is in contrast to the earlier results from *ex situ* experiments and simulations, which claimed that the outward expansion of Si nanotubes were fully confined by the active surface coatings[42, 124]. On the other hand, for hollow structures with the inactive surface coatings (*e.g.* metals[139]), the outward expansion at the outer surface could be effectively suppressed due to the mechanical confinement of the surface coating that is thick enough. Thirdly, the surface coatings such as thermal oxides do not alter the lithiation mode of *a*-Si anodes as well as the resultant total volume expansion after full lithiation. For all of *a*-Si nanotubes studied here, their lithiation mechanisms were not affected by surface coatings. Finally, since SiO_x has poor conductivity and low capacity than Si[140], a systematic study on the thickness effects of SiO_x is necessary for Si nanotube-based anodes in full battery cells, in order to achieve the optimal combination of high capacity and mechanical stability. In addition, our chemomechancial modeling, in conjunction with *in situ* TEM experiments, also reveal the critical role of anisotropy of lithiation-induced chemical strains in the geometrical changes of lithiated Si. Overall, this work not only provides new insights into the degradation of nanotube anodes with or without surface coatings, but also sheds light on the optimal design of novel hollow structures for high performance lithium-ion batteries.

Methods

Sample preparation and *in situ* lithiation experiment

The *a*-Si nanotubes were obtained via the following steps. The *a*-Si/carbon nanofiber (*a*-Si/CNF) nanocomposites were prepared by coating *a*-Si onto CNFs using a chemical vapor deposition (CVD) method (Applied Sciences Inc.)[132, 141]. The thickness of *a*-Si layers were about ~ 20-25 nm after 30 min coating. Then the *a*-Si/CNF nanocomposites were heated in air at 500°C for 2 h to remove the CNF core. TEM observations showed that the CNF had been completed removed, and the STEM line-scan analysis indicated that a negligible native SiO_x layer (less than 2 nm) formed on both the inner and outer surfaces of *a*-Si nanotubes, due to the low thermal treatment temperature and short treatment time[139]. To obtain thicker SiO_x layers, the *a*-Si nanotubes were further oxidized for longer time in air.

The *in situ* electrochemical experiment was conducted inside TEM by using a nanoscale battery, which consists of a working electrode of an individual *a*-Si nanotube, a counter-electrode of bulk Li metal and a solid electrolyte of naturally-grown lithium oxide (Li_2O). The detailed setup and procedure of the *in situ* TEM experiments have been documented in our previous publications[92, 132, 142].

Chemomechanical modeling

We have adapted a chemomechanical model[92] to simulate the two-stage lithiation process in a-Si nanotubes, involving the sandwich, two-phase lithiation during the first stage and the single-phase lithiation during the second stage. To implement our chemomechanical model[92], anisotropic lithiation expansion coefficient β_{ij} need to be determined. In the case of the a-Si nanotube with native oxides, the experimentally measured volume expansions of $(V_1 - V_0)/V_0$ and $(V_2 - V_0)/V_0$ at the end of the first-stage and second-stage lithiation are respectively about 172% and 252%, where V_0 is the initial volume of a-Si, and V_1 the volume after the first-stage lithiation and V_2 the volume after the second-stage lithiation. The corresponding logarithmic volume strains are respectively calculated as $\epsilon_{V1} = \log\left(\frac{V_1}{V_0}\right) = 1.00$ and $\epsilon_{V2} = \log\left(\frac{V_2}{V_1}\right) = 0.26$. We assume all the chemical strains occur in the cross section of the nanotube. For the first-stage lithiation, we take the anisotropic lithiation expansion coefficients in the radial and hoop directions as $\beta_r = 0.93$ and $\beta_\theta = 0.07$, so that $\beta_r + \beta_\theta = \epsilon_{V1}$; other components of β_{ij} are zero. For the second-stage lithiation, we take $\beta_r = 0.24$ and $\beta_\theta = 0.02$, so that $\beta_r + \beta_\theta = \epsilon_{V2}$. The same set of parameters are used in our chemomechanical modeling of 6.5‖9 nm SiO_x/Si/SiO_x nanotube. Additionally, the experimentally measured volume expansion of the lithiated SiO_x layer is about 82%, corresponding to a logarithmic volume strain of about 0.60. We take $\beta_r = 0.51$ and $\beta_\theta = 0.09$ for the lithiated SiO_x layer.

2.1.5 Lithiation of Ge/Si/Cu nanowire in lithium ion battery

Tremendous efforts have been devoted to mitigate the electrochemically-induced mechanical degradation of Si electrodes[3]. In recent studies, several effective material and electrode design strategies have been demonstrated for alleviating Si degradation during cycling. For example, reducing the feature size of Si particles and wires to the nanoscale can avert cracking and fracture[23, 27]. Creating hollow space in Si particle shells and tubes can reduce outward expansion during lithiation, thereby alleviating mechanical damage and regeneration of SEIs[28-31]. Besides engineering the geometry of Si electrodes, coatings of carbonaceous materials[32-34], metals[35, 36], oxides[29, 37-40] or conducting polymers[41] are often used. Coatings can enhance electrical transport, thus improving both the rate performance and uniform utilization of active Si. Meanwhile, coatings can impose mechanical confinement, alleviating the degradation of Si. However, one drawback of these coatings is that the specific capacity is usually reduced, due to their low Li storage capacity relative to Si. Nonetheless, these studies have pointed to a promising route of engineering the high-performance Si electrodes through a synergetic integration of small feature size, hollow space, conductive and high-capacity coating.

Here we report the fabrication and testing of a new architecture of composite Cu/Si/Ge nanowire (NW) anodes for LIBs. Figure 2.11a shows a schematic of this composite electrode consisting of Cu/Si/Ge NW arrays grown on a substrate of porous Ni foam, and each Cu/Si/Ge NW has a core of Cu segments and a Si/Ge bilayer shell (Figure 2.11b). This architecture effectively integrates several of the aforementioned design attributes for high performance. Specifically, the nanoscale geometry of NWs enables facile strain relaxation, and the sufficient free space between NWs facilitates volume accommodation during lithiation/delithiation cycling. Metallic Cu segments in the core enhance electron transport, while the hollow space between Cu segments accommodates Si deformation during cycling. Moreover, the outer Ge shell serves as an active high-capacity coating, since Ge has a high volumetric capacity (7366 AhL^{-1} for $Li_{15}Ge_4$, second to Si with 8334 AhL^{-1} for $Li_{15}Si_4$) and a high gravimetric capacity (1384 $mAhg^{-1}$ for $Li_{15}Ge_4$ which is about four times that of the commercial graphite)[143, 144]. Compared with Si, Ge has both a higher electrical conductivity (two orders of magnitude higher than Si) and a higher Li-ion diffusivity (more than 400 times higher than Si)[145]. Hence, the active Ge coating on Si can significantly enhance the rate capability relative to a pure Si electrode while maintaining a high specific capacity. More intriguingly, Si and Ge have different characteristic reaction voltages with Li. As a result, the Si/Ge composite electrode can exhibit a previously unknown reaction mechanism of co-lithiation/co-delithiation, which is unraveled by our *in situ* transmission electron microscopy (TEM), electrochemical testing (e.g., cyclic voltammetry), and chemomechanical modeling. This unique co-lithiation/co-delithiation in active Si and Ge enables an effective accommodation of large volume changes during cycling and thus enhances the damage tolerance of Cu/Si/Ge NWs. Therefore, thanks to the above favorable attributes of the Cu/Si/Ge NW array architecture, this composite electrode exhibits superior performance and long-cycle stability relative to both the Si/Ge thin-film electrode and the Si NW (or NT) electrode (Figure 2.11c). Our findings in this work offer crucial insights into a rational design of high-performance LIBs.

Figure 2.11 shows the schematic of fabrication of Cu/Si/Ge NW arrays on a porous Ni foam (see Methods). A pre-cleaned porous Ni foam (0.5 mm thick) was used as an electrically conducting substrate. A thin Cu layer (2 μm thick) was deposited onto the Ni foam by e-beam evaporation. CuO NWs (about 30 nm in diameter) were grown on the surface of the Cu layer by thermal oxidation in air. An inner shell of Si (60 nm thick) and an outer shell of Ge (30 nm thick) were sequentially sputter-coated on the surface of CuO

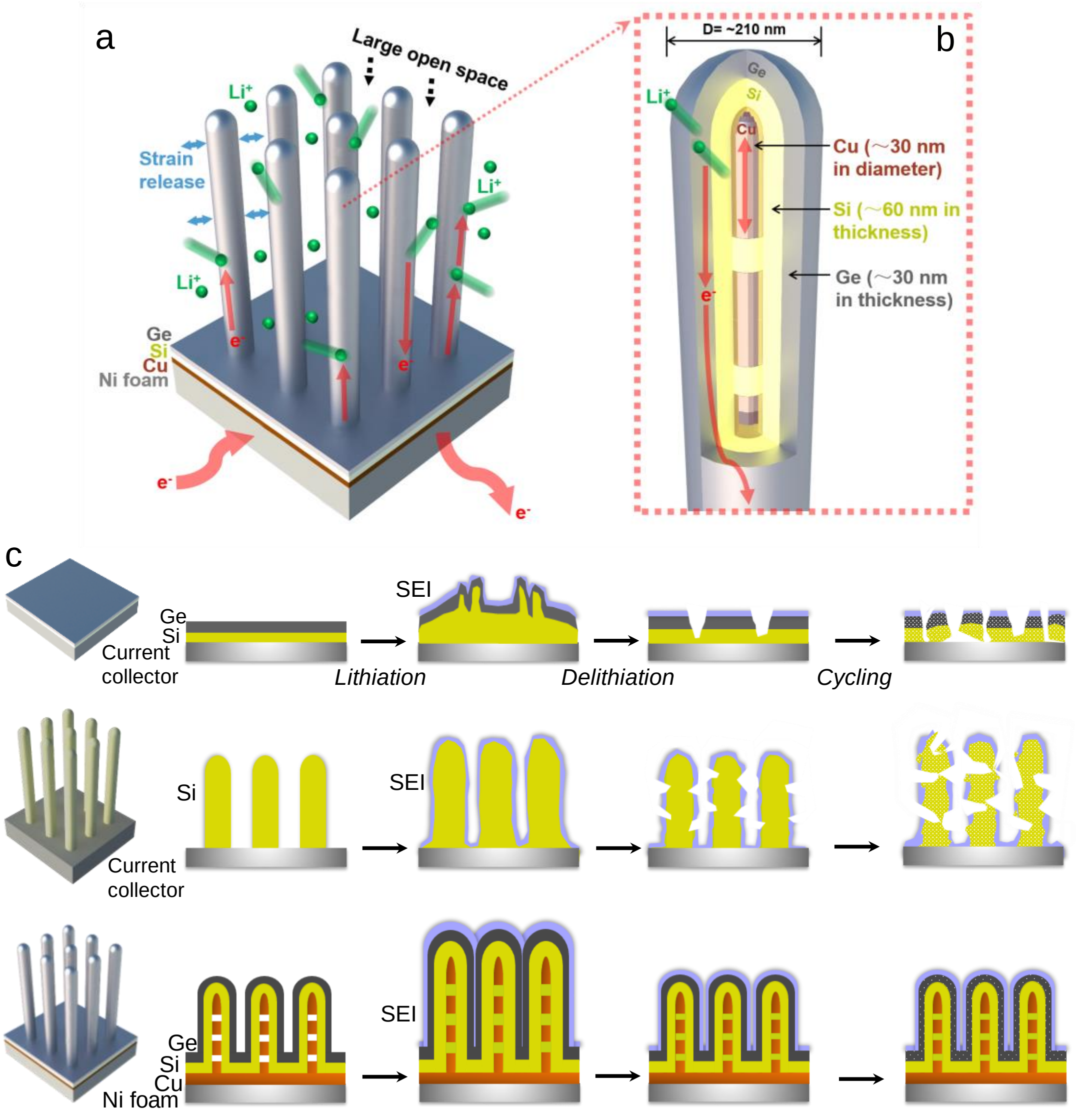
a
Large open space
Strain release
Li+
Ge
Si
Cu
Ni foam
e-
b
D= ~210 nm
Ge
Si
Cu
Cu (~30 nm in diameter)
Si (~60 nm in thickness)
Ge (~30 nm in thickness)
c
Ge
Si
Current collector
SEI
Lithiation
Delithiation
Cycling
Si
Current collector
SEI
Ge
Si
Cu
Ni foam
SEI

Figure 2.11. Schematic illustration of a high-performance Cu/Si/Ge nanowire (NW) electrode. a, The Cu/Si/Ge NW array was grown on a Ni foam substrate, and **b,** each NW had a core of Cu segments and a Si/Ge bilayer shell. **c**, The favorable design features, in conjunction with the synergy of active Si and Ge through dynamic co-lithiation/co-delithiation, enable long-cycle stability in the Cu/Si/Ge NW electrode, while the Si/Ge thin-film electrode and Si NW (or NT) electrode are prone to mechanical degradation in both active components and SEIs during cycling.

NWs. As-fabricated CuO/Si/Ge NWs were annealed in H_2/Ar to reduce the CuO cores, resulting in Cu core segments enclosed by a bilayer Si/Ge shell. Individual Cu/Si/Ge NWs had an average diameter of about 220 nm. Figure 2.12a-c show the scanning electron microscopy (SEM) images of a CuO/Si/Ge NW array on a porous Ni foam. These NWs have uniform geometry. The free space between NWs can be tailored to facilitate both electrolyte penetration and volume accommodation during lithiation/delithiation cycling. Figure 2.12d-e show the TEM images of an individual Cu/Si/Ge NW with a Si/Ge bilayer shell enclosing a core of Cu segments. The high resolution TEM (HRTEM) image in Figure 2.12f indicates that the Si/Ge bilayer is amorphous, which is verified by selected area electron diffraction (SAED, inset of Figure 2.12f) and further confirmed by x-ray diffraction (XRD) measurement. Figure 2.12g presents the scanning TEM (STEM) image of a Cu/Si/Ge NW along with energy dispersive spectroscopy line scanning profiles, confirming the bilayer structure with the outer Ge and inner Si shells enclosing Cu core segments. The elemental distribution of a Cu/Si/Ge NW was further analyzed by energy dispersive x-ray (EDX) spectroscopy mapping (Figure 2.12h). Evidently, Cu is locally confined in the core region, while Ge and Si are distributed over the outer and inner shells, respectively. To compare with the Cu/Si/Ge NW electrode, we also fabricated the Cu/Si NW electrode without Ge coating and the Si/Ge bilayer thin-film electrode without Cu. These two reference electrodes were grown directly on a porous Ni foam under similar conditions as the Cu/Si/Ge NW electrode.

The Cu/Si/Ge NW electrode exhibited a superior performance with large capacity, high rate capability and long cycle stability. The initial discharge and charge capacities were 3273 and 2373 $mAhg^{-1}$ at a low rate of 0.2C ($1C = 2\ Ag^{-1}$), respectively (Figure 2.13a). The corresponding first-cycle Coulombic efficiency was 72.5% (Figure 2.13b), which was higher than 51.8% from the Cu/Si NW electrode. At this rate, a capacity of 1500 $mAhg^{-1}$

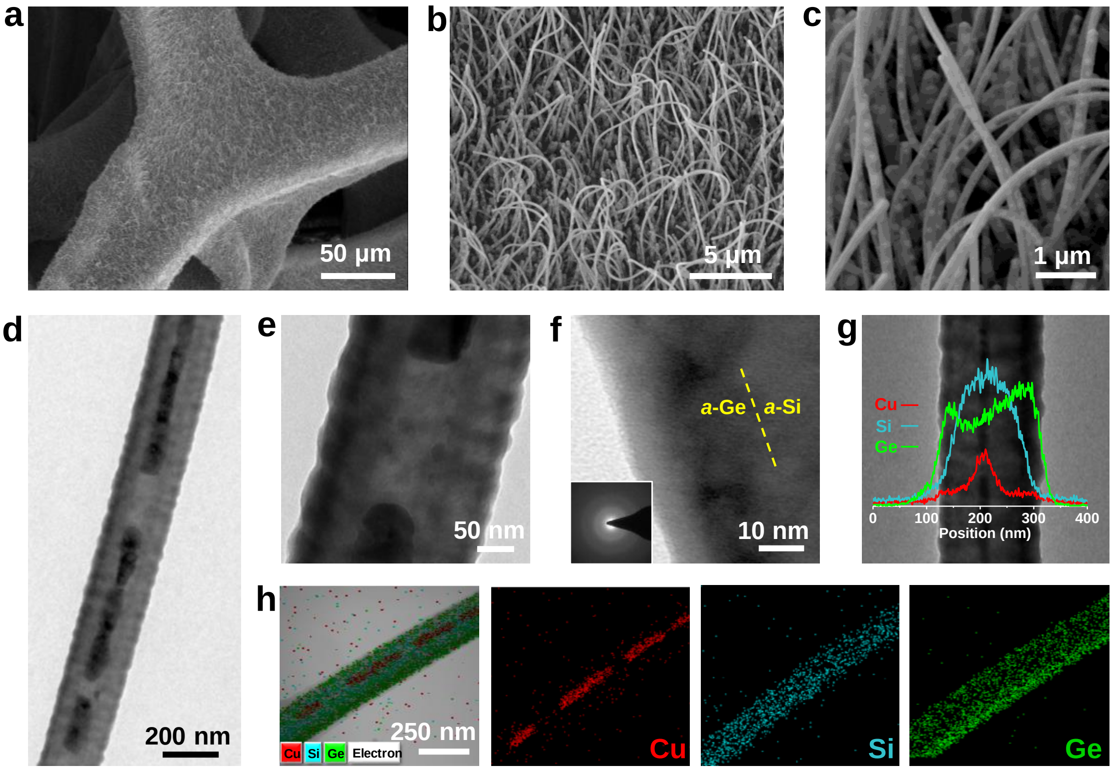
a
50 μm
b
5 μm
c
1 μm
d
200 nm
e
50 nm
f
a-Ge
a-Si
10 nm
g
Cu
Si
Ge
0
100
200
300
400
Position (nm)
h
250 nm
Cu
Si
Ge
Electron
Cu
Si
Ge

Figure 2.12. Characterization of the Cu/Si/Ge NW electrode. a-c, SEM images of Cu/Si/Ge NW arrays grown on a Ni foam. d-e, TEM image of a single Cu/Si/Ge NW, f, HRTEM image of the Si/Ge bilayer with corresponding SAED pattern (inset). g, STEM image of a Cu/Si/Ge NW, with corresponding EDX scan-line spectra and h, STEM mapping.

was maintained for the Cu/Si/Ge NW electrode after 100 cycles (with ~ 70% capacity retention from the 2nd to the 100th cycle). It was comparable to 1615 mAhg^{-1} from the Cu/Si NW electrode, indicating a high specific capacity. In contrast, the capacity of the Si/Ge thin-film electrode faded rapidly, retaining only 857 mAhg^{-1} after 100 cycles (~ 40% capacity retention from the 2nd to the 100th cycle). Moreover, the Cu/Si/Ge NW electrode exhibited an outstanding long-cycle performance, retaining a specific capacity of 1523 mAhg^{-1} (~ 81% capacity retention) after 3000 cycles at a high cycling rate of 2C (Figure 2.13c). In contrast, the Cu/Si NW electrode had a marked capacity decay, retaining only

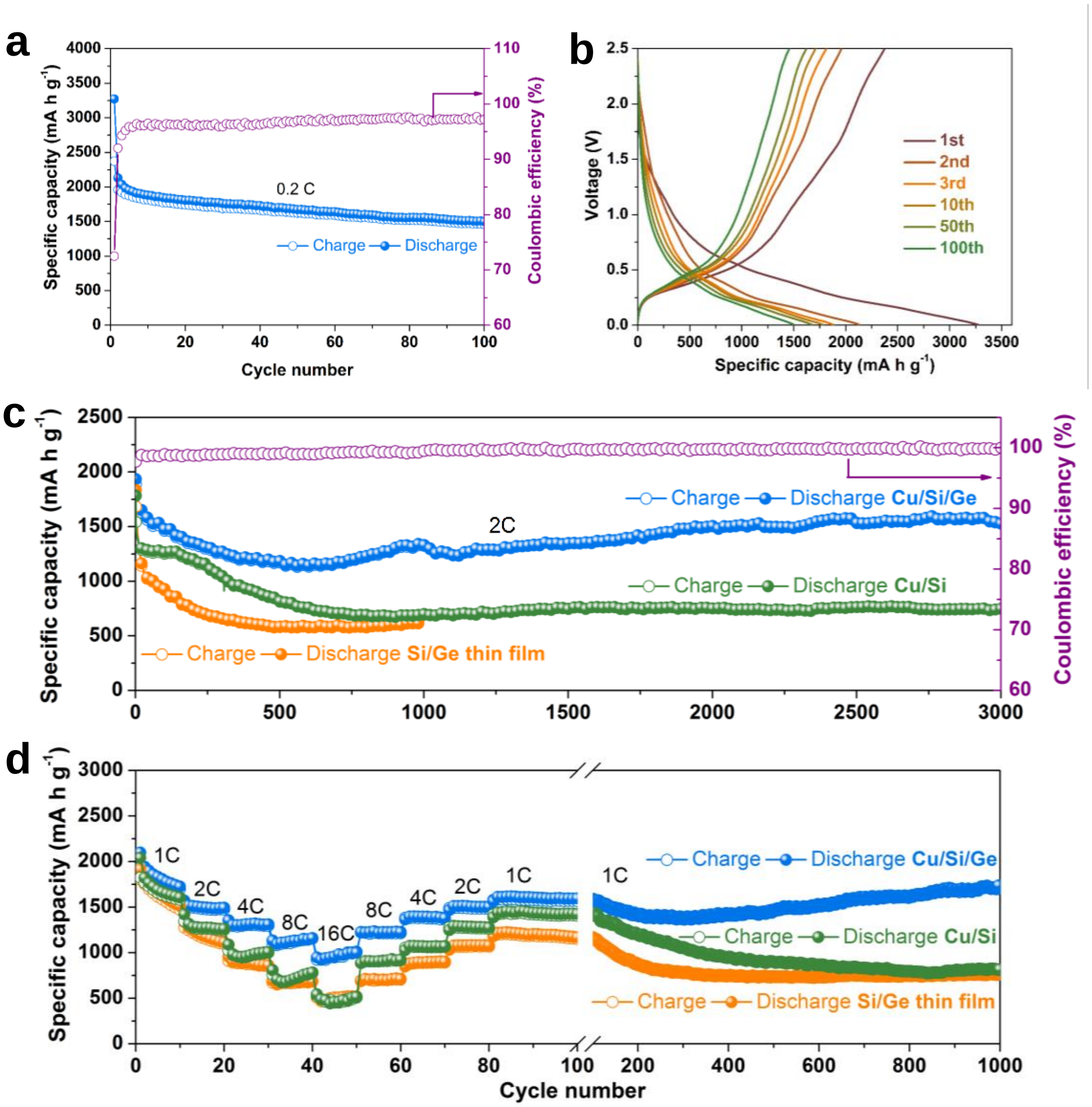

Figure 2.13. Electrochemical performance of the Cu/Si/Ge NW electrode. a, Capacity performance at a slow rate of 0.2C. b, Corresponding galvanostatic charge–discharge profiles at different cycles. c, Long-cycle performance for Cu/Si/Ge NW, Cu/Si NW and Si/Ge thin-film electrodes at 2C; all the electrodes were first tested at 0.2C for two cycles and then subjected to long-term cycling. d, Comparison of specific capacity of Cu/Si/Ge NW, Cu/Si NW and Si/Ge thin-film electrodes at various C rates (from 1C to 16C) for 100 cycles and then 1C for another 900 cycles; all the electrodes were first tested at 0.2C for two cycles and then under rate testing.

745 mAhg^{-1} of the initial 1542 mAhg^{-1} (~ 48% capacity retention) after 3000 cycles. The capacity of the Si/Ge thin-film electrode decayed even faster, retaining only 628 mAhg^{-1}

of the initial 1683 mAhg^{-1} after 1000 cycles (only ~ 37% capacity retention).

The Cu/Si/Ge NW electrode also exhibited an excellent rate performance with long-cycle stability (Figure 2.13d). A high charge capacity of 1010 mAhg^{-1} was measured at a high rate of 16C after 10 cycles, almost twice higher than that of the Cu/Si NW electrode (506 mAhg^{-1} at 16C). The capacity retention (~ 60%) of the Cu/Si/Ge NW electrode was also better than that of the Cu/Si NW electrode (~ 33%) and the Si/Ge thin-film electrode (~ 35%) from 1C to 16C. More interestingly, even at a rate up to 16C, the lithiation potential of the Cu/Si/Ge NW electrode still showed a sloping profile between 0.5 and 0.005 V, consistent with a previous report of lithiation-induced formation of amorphous Li_xSi (a-Li_xSi) and Li_xGe (a-Li_xGe)[146, 147]. Furthermore, the Cu/Si/Ge NW electrode exhibited superior cycle stability, retaining a capacity of 1728 mAhg^{-1} (~ 89% capacity retention) after initial 100 cycles at rates ranging from 1C to 16C and additional 900 cycles at 1C. This result demonstrates that the Cu/Si/Ge NW electrode possesses an exceptional ability to retain a high capacity after charge/discharge at high rates. In comparison, the capacities of the Cu/Si NW and Si/Ge thin-film electrodes fade rapidly, retaining only 816 mAhg^{-1} (~ 45% capacity retention) and 761 mAhg^{-1} (~ 42% capacity retention) after 1000 cycles, respectively.

The superior performance of the Cu/Si/Ge NW electrode can be attributed to the beneficial effects of small feature size, hollow space, a conductive metallic core, and a high-capacity coating, as discussed in the Introduction. We stress that while Ge is much more expensive than Si from the standpoint of practical applications, the Ge/Si bilayer shell can serve as a model system for studying the effect of dynamic reactions and particularly the synergy of active components (*i.e.*, Si and Ge in this work) in high-capacity composite electrodes on their long-cycle stability.

To understand the synergy of dynamic reactions in active Si and Ge, we performed *in situ* TEM and cyclic voltammetry experiments. Figure 2.14a shows the time-lapse TEM snapshots during lithiation of a single Cu/Si/Ge NW. During lithiation, the Cu/Si/Ge NW expanded in both the axial and radial directions. This contrasted with the dominant radial expansion with negligible axial elongation in Si NWs revealed by previous *in situ* TEM studies[4, 148]. At 240 s, the axial elongation and radial expansion were respectively 118% and 124~133% (measured for different radial cross-sections), resulting in a total volume expansion of 180~207% in the Si/Ge bilayer. Interestingly, the lithiated NW became bent. The distance between adjacent Cu segments increased with the overall elongation of the lithiated NW, thus providing additional internal space to accommodate the inward expansion of lithiated Ge/Si; the diameters of Cu segments remained nearly constant. Hence the unique segmental structure of Cu core is beneficial to reducing the outward swelling, thereby mitigating the mechanical degradation of lithiated Si/Ge and SEIs. During delithiation, the Cu/Si/Ge NW shrunk in both the axial and radial directions. As the lithiation and delithiation were repeated for several cycles, there was no observable mechanical damage such as cracking or fracture. Occasionally, the Cu/Si/Ge NW experienced a sudden change in contact with Li/Li_2O, leading to an abrupt variation in the expansion/contraction rate for a few seconds. Nonetheless, structural evolution of the Cu/Si/Ge NW was sufficiently robust and largely reversible without observable mechanical degradation in multiple lithiation/delithiation cycles.

To gain a deep understanding of lithiation/delithiation dynamics, we performed an in-depth analysis of *in situ* TEM images. The results revealed a novel mechanism of dynamic co-lithiation/co-delithiation in the Si/Ge bilayer shell. As shown in Figure 2.14b, the initial lithiation, referred to as stage I, occurred primarily in the outer Ge layer, while the inner Si layer remained nearly unlithiated. For example, the left image in Figure 2.14b displays a segment of the Cu/Si/Ge NW before lithiation, where the thicknesses of the outer Ge and inner Si layers were 39.2 nm and 52.5 nm, respectively. At the end of stage I (the middle image in Figure 2.14b), the thickness of the outer Ge layer was increased to 52.8 nm, indicating the ongoing lithiation therein. In contrast, the thickness of the inner Si layer remained nearly unchanged, implying that the Si lithiation had not started yet. Following stage I, both Ge and Si layers were co-lithiated simultaneously, referred to as stage II. Co-lithiation was evident from a concurrent increase of thickness in both the Ge and Si layers. For example, the right image in Figure 2.14b shows an intermediate state of stage II, where the thicknesses of the Ge and Si layers were increased to 74.6 nm and 82.5 nm, respectively. Figure 2.14c shows the measured thicknesses of Ge, Si and Si/Ge layers as a function of time. It is seen that the incubation period without lithiation initially lasted for about 80 s; stage I of lithiation of Ge spanned between 80s ~ 190s; and stage II of co-lithiation of Ge and Si between 190s ~ 250s. Similarly, delithiation also experienced a two-stage process, *i.e.*, the initial delithiation of the outer Ge layer was followed by the subsequent co-delithiation of both the Si and Ge layers. To understand the *in situ* TEM results of two-stage lithiation/delithiation, we performed cyclic voltammetry (CV) and galvanostatic charge-discharge measurements with a standard coin cell configuration. Figure 2.14d shows the CV curves of the Cu/Si/Ge NW electrode measured at a scan rate of 0.1 mVs^{-1}

over the potential window of 0.005–2.5 V versus Li/Li$^+$. It is seen that a peak occurs at 0.55 V during the first discharge process, but disappears in subsequent cycles, suggesting this peak can be attributed to the formation of SEIs[149]. In Figure 2.14d, a peak occurs at 0.35 V in the first discharge process. There is no corresponding peak in the CV curves of

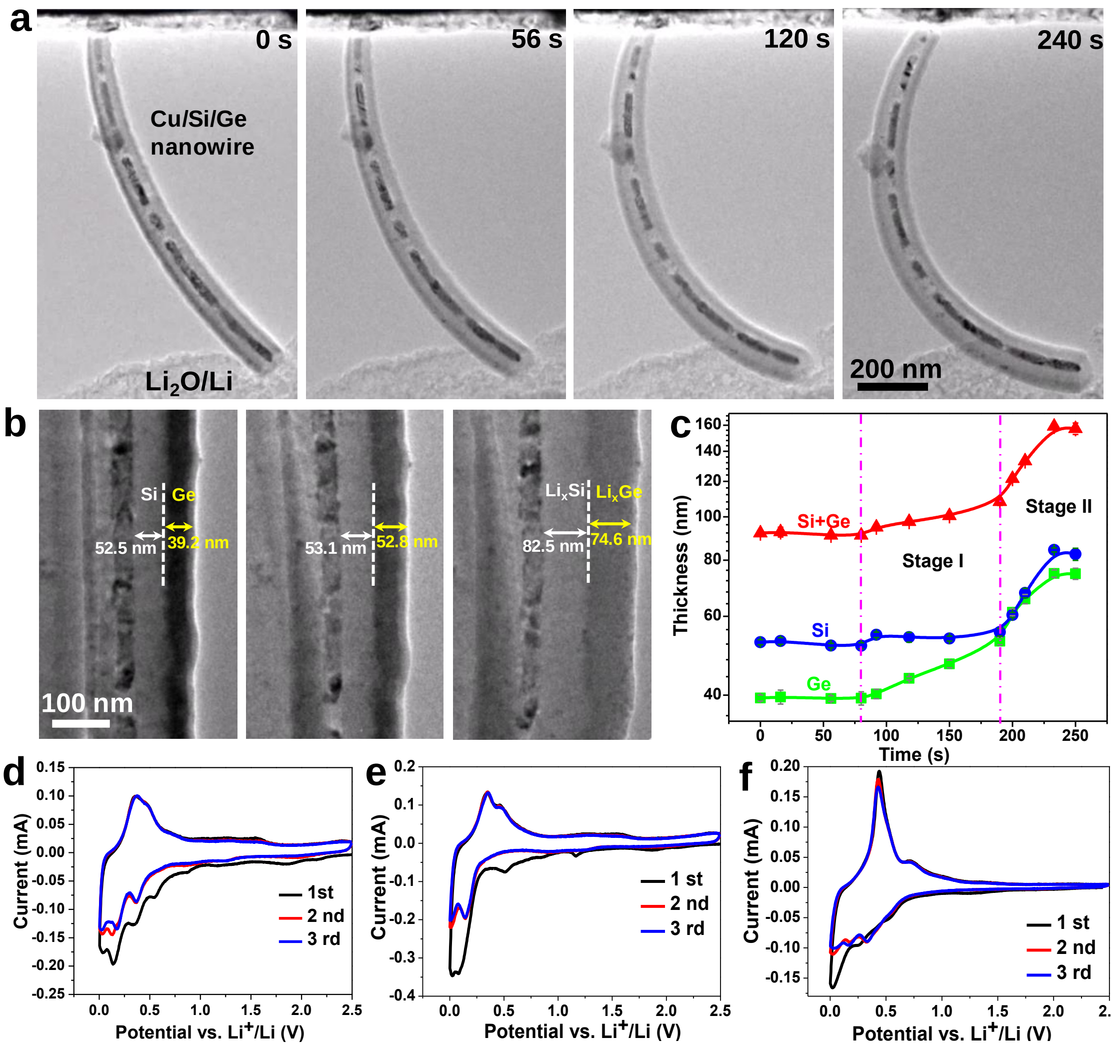

Figure 2.14. *In situ* TEM and cyclic voltammetry (CV) experiments. a, Time-lapse TEM images of lithiation of a single Cu/Si/Ge NW. b, Magnified TEM images showing the thicknesses of the Si/Ge bilayer shell as a function of time during lithiation, and c, corresponding quantitative measurements showing the thickness changes of Si/Ge bilayer shell as a function of lithiation time. d-f, CV curves for the Cu/Si/Ge NW, Cu/Si NW, and Cu/Ge NW electrodes during the first three discharge/charge cycles, respectively.

both the Cu/Si NW electrode (Figure 2.14e) and the Si thin-film electrode[146],

while a similar peak occurs in the CV curves of the Cu/Ge NW electrode (Figure 2.14f) measured in this work and the Ge thin-film electrode in a previous study[147]. So such a peak should correspond to the conversion of *a*-Ge to *a*-Li_xGe, suggesting that Ge first reacts with Li without Si involved. This is consistent with our *in situ* TEM observation of stage I of lithiation of Ge only. Previous *in situ* TEM experiments[26, 92] showed that the lithiation of *a*-Si occurred in a two-phase process through migration of a sharp phase boundary, resulting in *a*-Li_xSi ($x \sim 2.5$). The peak at 0.35 V in the CV curve also indicates that the initial lithiation of *a*-Ge occurs at a characteristic voltage, suggesting a possible two-phase lithiation in the outer layer of Ge and the resulting formation of *a*-Li_xGe.

In Figure 2.14d, the following two peaks arise at 0.14 V and 0.03 V, respectively. These two peaks are also observed in the CV curves of both the Cu/Si NW electrode (Figure 2.14e) and the Cu/Ge NW electrode (Figure 2.14f). Hence, they should correspond to co-lithiation of Li_xGe and Si, as observed in our *in situ* TEM experiments. It should be emphasized that these characteristic peaks are also observed during the second and third cycles, suggesting that a similar reaction pathway of two-stage lithiation persists beyond the first cycle. Moreover, during the first charge of the Cu/Si/Ge NW electrode (Figure 2.14d), two anodic peaks at 0.38V and 0.47 V are observed. However, these two peaks are not sharp and also somewhat overlap. Based on *in situ* TEM observations, they should correspond to stage I of delithiation of *a*-Li_xGe and stage II of co-delithiation of *a*-Li_xSi and *a*-Li_xGe, respectively. During subsequent charging processes, all peaks were reproducible, indicating the operation of the same reaction mechanisms. In addition, recall that Figure 2.13b presents the galvanostatic charge-discharge profiles of the Cu/Si/Ge NW

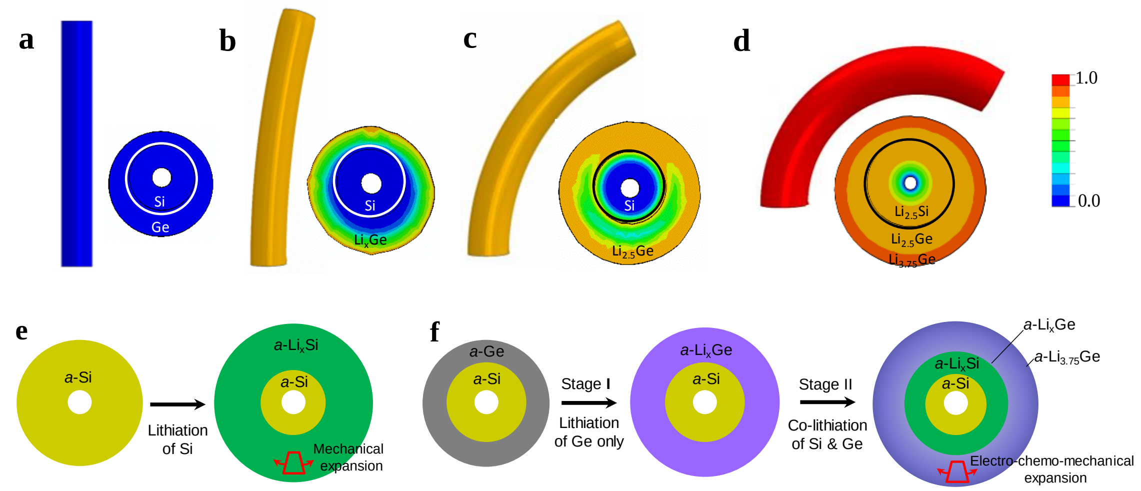
a
b
c
d
Si
Ge
Si
Li_xGe
Si
$Li_{2.5}Ge$
$Li_{2.5}Si$
$Li_{2.5}Ge$
$Li_{3.75}Ge$
1.0
0.0
e
a-Si
Lithiation of Si
a-Li_xSi
a-Si
Mechanical expansion
f
a-Ge
a-Si
Stage I
Lithiation of Ge only
a-Li_xGe
a-Si
Stage II
Co-lithiation of Si & Ge
a-Li_xGe
a-$Li_{3.75}Ge$
a-Li_xSi
a-Si
Electro-chemo-mechanical expansion

Figure 2.15. Chemomechanical effects of lithiation of a Si/Ge NT. a-d, Chemomechanical simulation snapshots showing progressive bending (left) and the cross-sectional distribution of the normalized Li/Ge concentration (right) in a Si/Ge NT during stage I of lithiation of Ge only and stage II of co-lithiation of Si and Ge. e, Illustration of dominant *mechanical* expansion near the surface during lithiation of a Si NT. f, Illustration of *electrochemical*-mechanical expansion associated with insertion of active Li near the surface during co-lithiation of a Si/Ge NT.

electrode tested at 0.4 Ag^{-1} between 2.5 and 0.005 V. The observed plateaus in the first discharge curve are in accordance with the CV results and associated reaction steps.

To understand the above *in situ* TEM results, we performed the chemomechanical modeling of lithiation in a bilayer Si/Ge nanotube (NT) (see Methods). Our model was focused on elucidating the origin of bending deformation in the lithiated Si/Ge NT. From *in situ* TEM images (Figure 2.14a), we observed that the cross-sectional thicknesses of both the Si and Ge layers were non-uniform. This implies that the centers of both the Si and Ge shells did not coincide, and also deviated from the nominal center of the whole Si/Ge NT. Figure 2.15a-e show the simulated snapshots of two-stage lithiation in a bilayer Si/Ge NT with an eccentricity of 0.125 (see Methods), which was assigned based on the TEM image (Figure 2.14a). In our simulations, the bending deformation arose during stage

I of lithiation of Ge and continued to increase during stage II of co-lithiation of Ge and Si. Hence, a key insight from our chemomechanical modeling is that the observed bending deformation during *in situ* TEM was caused by the eccentricity of Cu/Si/Ge NWs, leading to a non-uniform lithiation in the NW cross section. As a result, the axial elongation became non-uniform within the cross section, causing the bending deformation in the lithiated Si/Ge NW.

The dynamic co-lithiation/co-delithiation in active Si and Ge has important implications for mitigating the lithiation-induced degradation in large-volume-change electrode materials. It has been recently recognized that lithiation of *a*-Si occurs via a two-phase mechanism[26, 92], i.e., migration of a sharp react front (i.e., phase boundary) between the *a*-Si reactant and the *a*-Li_xSi (x ~ 2.5) product. Behind the react front, the *a*-Li_xSi product undergoes little further lithiation as *a*-Si is being consumed by a sweeping reaction front. The similar CV curves between *a*-Si and *a*-Ge suggest that the two-phase lithiation likely occurs in *a*-Ge as well. It is known that the abrupt change of Li concentration across the react front can result in a large local volume change[92]. In the case of a flat react front, the large local volume change at the reaction front will have little mechanics effects on the *a*-Li_xSi product left behind. However, in the case of *a*-Si wire or particle, the reaction front is curved[92]. As a result, *a*-Li_xSi behind the reaction front will suffer large mechanical deformation, particularly stretching in the hoop direction (Fig. 2.15e), as the reaction front migrates toward the center of the *a*-Si wire or particle and thereby pushes out the *a*-Li_xSi product[133]. The large mechanical stretching in *a*-Li_xSi behind the reaction front is one of the major causes of the electrochemically-induced mechanical degradation in large-volume-change electrode materials such as *a*-Si[3, 133].

In contrast, during co-lithiation of the Si/Ge bilayer shell, the lithiation-induced volume expansion in the inner Si layer can be accommodated by the concurrent co-lithiation in the outer Ge layer. In other words, the material addition through electrochemical Li insertion in the outer Ge layer, as opposed to pure mechanical stretching, serves to accommodate the volume expansion being produced in the inner Si layer. Therefore, the electrochemically active outer Ge layer in the case of the Si/Ge bilayer (as illustrated in Figure 2.15f) should be more tolerant against mechanical degradation than the electrochemically inactive outer layer, e.g., an "outer Si layer" in the case of pure Si NW or NT (as illustrated in Figure 2.15e). The above beneficial effects of dynamic co-lithiation in the Si/Ge bilayer should hold during co-delithiation and hence during lithiation/delithiation cycling. In addition to the benefits of dynamic co-lithiation/co-delithiation, both the metallic Cu core and the Ge outer layer (as opposed to the Si NW) can enhance electronic/ionic transport in the Cu/Si/Ge NW electrode. As a result, lithiation/delithiation would be more uniform in the Cu/Si/Ge NW electrode than the pure Si NW one. The above factors can collectively contribute to mitigating the electrochemically-induced mechanical degradation, thereby enhancing the long-cycle structural stability of the Cu/Si/Ge NW electrode during cycling.

To demonstrate the enhanced long-cycle stability in the Cu/Si/Ge NW electrode, we examined the electrode structures after 3,000 charge/discharge cycles with *ex situ* SEM and TEM imaging. Figure 2.16a shows that the NW arrays were retained without drastic morphological changes. They also remained in close contact with the current collector. At the individual NW level, Figure 2.16b shows that the hollow space between Cu segments in the core was filled with extruded Si. While the outer Ge layer experienced volume expansion during lithiation, there is no obvious cracking therein. Moreover, the outer Ge layer appeared as the highly porous sponge composed of interconnected ligaments of *a*-Ge. Such spongy Ge has been shown with beneficial effects on accommodating the volume changes[144], so as to mitigate the mechanical degradation under lithiation/delithiation cycling. More importantly, the inner Si layers appeared to remain coherent and did not turn into a fluffy structure. This can be reasonably attributed to the protection of the outer Ge layer, which was retained due to their capability of effective accommodation of volume changes during Si lithiation/delithiation through the unique dynamic co-lithiation/co-delithiation mechanism of Ge and Si layers. In contrast, the Cu/Si NW exhibited drastically structural changes, resulting in a highly fluffy morphology (Figure 2.16c). Compared to the Cu/Si/Ge NW (Figure 2.16b), Figure 2.16d shows that the surface of the Cu/Si NW became rougher, the structure became more fluffy with pores between grains on the edges, and the diameters of Cu/Si NW arrays appeared to be larger, which indicates more irreversible changes. Additionally, the core of Cu segments disappeared (Figure 2.16d), which indicates the dissolution of Cu possibly by electrolytes due to the poor structural integrity of Cu/Si NWs.

To demonstrate the applicability of our electrode to practical applications, we assembled a full cell with a Cu/Si/Ge NW anode and a $LiCoO_2$ cathode. When tested with this full-cell configuration, the Cu/Si/Ge NW electrode exhibited a reversible capacity of 1037 $mAhg^{-1}$ (based on the weight of active materials in the anode) after 50 cycles (with 80% capacity retention) at a current density of 0.5 Ag^{-1} as well as a high rate performance of 709 $mAhg^{-1}$ after 10 cycles at 10 Ag^{-1} with capacity retention of 51% from 0.2 to 10 Ag^{-1} Moreover, the as-assembled full cell can power red light-emitting diodes (LEDs) with a

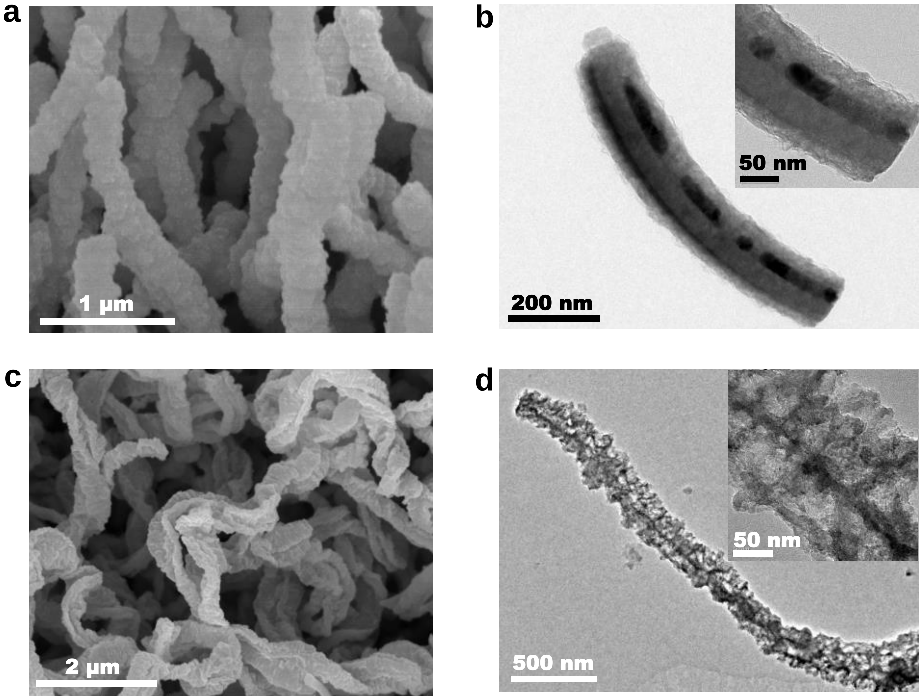

Figure 2.16. Comparison of microstructural changes in the Cu/Si NW and Cu/Si/Ge NW electrodes after 3000 cycles at 2C. a, SEM image of a Cu/Si/Ge NW array. b, TEM image of a single Cu/Si/Ge NW. c, SEM images of a Cu/Si NW array. d, TEM image of a single Cu/Si NW.

working voltage of 2 V, indicating that the Cu/Si/Ge NW electrode could be potentially used in practical devices.

To summarize, our Cu/Si/Ge NW electrode architecture has integrated several favorable attributes for high performance: small feature size, interior hollow space, a conductive core, and a high-capacity and high-conductivity outer coating. More importantly, the synergy of active Si and Ge contributes to the outstanding capacity, rate capability, and long-cycle stability of this composite electrode. We find that the Si/Ge bilayer shell exhibited a novel dynamic reaction mechanism of co-lithiation/co-delithiation in Si and Ge, which effectively accommodate the large volume changes during cycling.

This previously unknown reaction mechanism is vital to improving the tolerance to electrochemically-induced damages, thus dramatically enhancing the long-cycle structural stability and performance of the electrode. More importantly, this work demonstrates a promising pathway of harnessing the synergic reaction dynamics of multiple active components to enhance the performance of heterogeneous composite electrodes for next generation Li-ion batteries.

Methods

Fabrication of CuO nanowires on Ni foam. A Ni foam (0.5 mm thick, surface density of about 420 gm^2, 40-50 pores per centimeter, purity > 99.99%, Changsha Lyrun New Materials Co. Ltd.) was used as the conducting substrate. This foam was cleaned in alcohol by ultrasonic for 10 min, adequately rinsed with alcohol and distilled (DI) water, and blow-dried by compressed air. Then it was placed inside a conventional electron beam evaporation system (JunSun EBS-500). After the vacuum level in the chamber reached 1.6×10^{-6} Torr, a Cu layer was deposited onto the Ni foam by e-beam evaporation. This sample was furnace-heated for 12 hours at 400 °C in static air for growing CuO NWs. After heating, the furnace was cooled down naturally to room temperature.

Synthesis of CuO/Si/Ge nanowire arrays on Ni foam. Si and Ge was deposited on the surface of CuO NWs grown directly on a Ni foam (circular disk with a diameter of 14 mm) by sputtering of a 99.999% pure Si target and a 99.999% pure Ge target at a working pressure of 3 Pa. Firstly, sputtering of Si was performed with an Ar working gas of 70 sccm and power of 300 W for 300 seconds. Then the power of Si target was turned off and the power of Ge target of 300 W was turned on. Ge sputtering with an Ar working gas of 70 sccm lasted for 295 seconds, while the sample was rotated with a speed of 20 r min^{-1}. The mass loading of Si/Ge was about 0.15-0.18 mg cm^{-2}, which was determined by measuring the CuO NW arrays on a Ni foam substrate on a microbalance (Mettler Toledo XS3DU with an accuracy of 1 µg) before and after sputtering. The compositions of the CuO/Si/Ge film with different ratios of Si and Ge can be readily adjusted by changing the sputtering time of Si and Ge. The substrates were kept at room temperature.

Synthesis of Cu/Si/Ge NW arrays on Ni foam. The as-fabricated CuO/Si/Ge NW samples were annealed at 300 °C in H_2/Ar (95% Ar and 5% H_2) for 8 hours to reduce the CuO cores with a flow rate of 60 sccm, so as to transform CuO /Si/Ge NW arrays into Cu/Si/Ge NW arrays, which were then naturally cooled to room temperature.

Material characterization. Cu/Si/Ge NW arrays were characterized by field emission SEM (Hitachi S4800 FESEM), TEM (FEI Tecnai G2 20 TEM) and X-ray diffraction (Rigaku Ultima IV). To observe the electrode surface morphology after cycling, the cell was disassembled and the electrodes were rinsed with dimethyl carbonate in an argon-filled glove box so as to remove the electrolyte. Then, they were dried at 80°C in a vacuum oven. For *ex situ* TEM studies, the electrode material was scraped off from the Ni foam substrate and the powder was recovered in a glove box and dispersed in ethanol. A drop of suspension was deposited on a Cu grid.

Electrochemical testing. Coin-type half cells (CR2025), assembled in an argon-filled glove box (MBRAUN, LABmaster 100, Germany), were used to evaluate the electrochemical performance of as-synthesized Cu/Si/Ge NW arrays grown on a Ni foam as a working electrode without the use of any binder or conductive agent. The counter and reference electrodes were Li metal foil (15 mm in diameter), and the electrolyte solution was 1 M $LiPF_6$ (EC:DMC:EMC = 1:1:1, in volume). The cells were charged and discharged over a voltage range of 0.005–2.5 V (versus Li^+/Li) at room temperature by using the Land CT2001A system (Wuhan, China). Cyclic voltammetry (CV) was performed on a four-channel multifunctional electrochemical work station (VersaSTAT MC, America), and scanning was conducted from 2.5 V to 0.005 V versus Li/Li^+ at a rate of 0.1 mV s^{-1}. The full cell was designed with a N/P ratio of 1:1.3; the cathode and anode areal capacities were 0.26 mAh cm^{-2} and 0.2 mAh cm^{-2}, respectively. The cathode electrode was fabricated by mixing 80 wt% commercialized lithium cobalt oxide (LCO) with 10 wt% carbon black as a conducting agent and 10 wt% polyvinylidene fluoride dissolved in N-methyl-2-pyrrolidone (NMP) as a binder to form a slurry, which was then spread onto an Al foil current collectors and dried under vacuum at 80 °C for 24 hours. CR-2025 coin-type cells were assembled in a glove box filled with argon gas. The electrolytes and separator in the full cell were the same as those in the half-cell described above. Electrochemical analysis of the full cell was carried out in the voltage window between 2.0 and 3.9 V. All electrochemical tests were performed using a Land CT2001A system (Wuhan, China).

***In situ* TEM**. Supplementary Fig. 10 shows the schematic of *in situ* nano-battery testing via TEM[4]. Cu/Si/Ge NWs were loaded on a Pt tip and then connected to Li/Li_2O on a W tip. The native Li_2O on the Li surface served as a solid electrolyte. Lithiation of an individual Cu/Si/Ge NW started when a negative voltage was applied to the Pt end, while delithiation initiated upon reversing the sign of the voltage bias.

Chemomechanical modeling. We simplified the Cu/Si/Ge NW system as a nanotube (NT) with a Si/Ge bilayer shell and without Cu segments in the core. Despite this simplification, the simulated inward displacement was reasonably small at the inner radius of the lithiated Si shell, consistent with *in situ* TEM observations. The center of the Si shell deviates from that of the Ge shell. The extent of deviation is quantified with eccentricity, which is defined as ratio of the distance between centers of Si and Ge shells over the radius of Ge shell. In our simulations, the eccentricity was taken as 0.125, and the radius ratio of Si and Ge shells was 1.2 over 2. In addition, the length of the Si/Ge NT was 16 times the diameter of the Ge shell, consistent with geometries in the TEM images. Our chemomechanical model incorporated the key features of two-stage lithiation from *in situ* TEM, i.e., stage I of lithiation of Ge only and stage II of co-lithiation of both Ge and Si. To simulate lithiation within the Si/Ge bilayer, we adopted an earlier model of two-phase lithiation of *a*-Si[92]. The detailed model setup and material parameters are described in the Supplementary Materials.

2.1.6 Lithiation of Si nanoparticle coated with SiO_x

Previously, we have discussed about the effect of coatings on Si nanowire, Si nanotube and Ge/Si/Cu nanowire. In this section we will focus on another typical Si based anode, namely, Si nanoparticle. Similarly, dramatic volume changes (~ 300%) of Si nanoparticles occur during lithiation/delithiation, which can cause severe cracking and pulverization of Si anodes[3, 22-24], as shown in Figure 1.4b. An effective way to suppress the

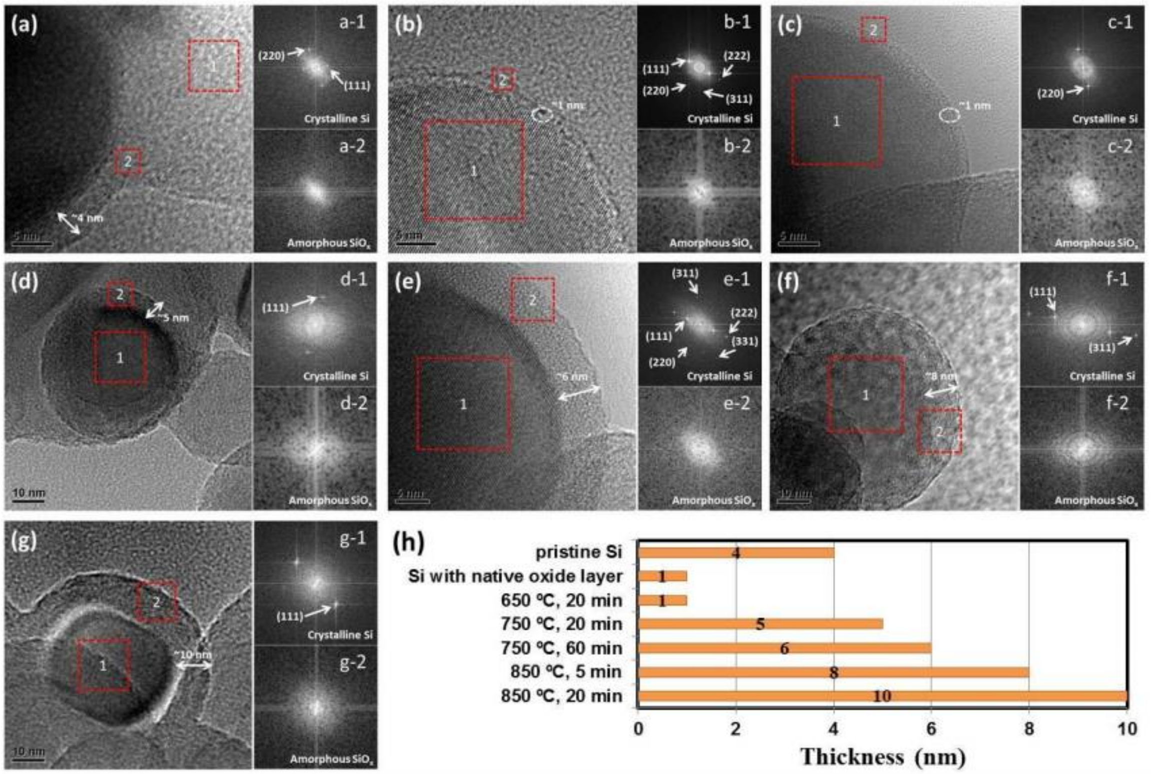
(a)
a-1
(220)
(111)
Crystalline Si
a-2
Amorphous SiO$_x$
~4 nm
5 nm
(b)
b-1
(111)
(222)
(220)
(311)
Crystalline Si
b-2
Amorphous SiO$_x$
~1 nm
5 nm
(c)
c-1
(220)
Crystalline Si
c-2
Amorphous SiO$_x$
~1 nm
5 nm
(d)
d-1
(111)
Crystalline Si
d-2
Amorphous SiO$_x$
~5 nm
10 nm
(e)
e-1
(311)
(222)
(111)
(331)
(220)
Crystalline Si
e-2
Amorphous SiO$_x$
~6 nm
5 nm
(f)
f-1
(111)
(311)
Crystalline Si
f-2
Amorphous SiO$_x$
~8 nm
10 nm
(g)
g-1
(111)
Crystalline Si
g-2
Amorphous SiO$_x$
~10 nm
10 nm
(h)
pristine Si
Si with native oxide layer
650 °C, 20 min
750 °C, 20 min
750 °C, 60 min
850 °C, 5 min
850 °C, 20 min
4
1
1
5
6
8
10
0
2
4
6
8
10
Thickness (nm)

Figure 2.17 The TEM images of Si nanoparticles with different oxidation treatment. The coating thickness from (a) to (g) and the corresponding treatment methods are shown in (h). (a) Pristine Si nanoparticles; (b) Si nanoparticle with native oxide layer about 1 nm thick; (c) Si nanoparticle treated under 650 ºC for 20 min, resulting in 1 nm coating thickness; (d) Si nanoparticle treated under 750 ºC for 20 min, resulting in 5 nm coating thickness; (e) Si nanoparticle treated under 750 ºC for 60 min, resulting in 6 nm coating thickness; (f) Si nanoparticle treated under 850 ºC for 5 min, resulting in 8 nm coating thickness; (g) Si nanoparticle treated under 850 ºC for 20 min, resulting in 10 nm coating thickness;

degradation is to deposit a layer of coating onto the anode. As argued in section 2.1.2, SiO_x is a good candidate to serve as clamping coating onto Si based anode. In this section, we will study the thickness effect of SiO_x on the lithiation behavior of Si nanoparticle.

As shown in Figure 2.17, the average size of Si nanoparticle is about 30 nm in diameter. With different treatment method, the SiO_x coating thickness was obtained ranging from 1 nm to 10 nm. The method to obtain different coating thickness is summarized as in

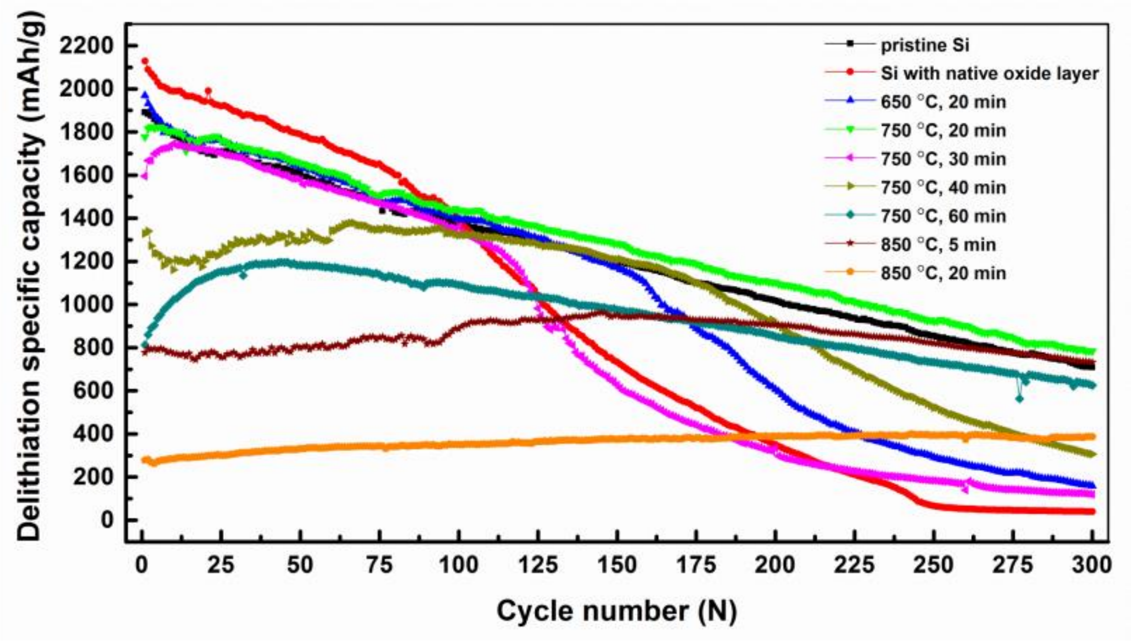

Figure 2.18 Cycle performances of Si nanoparticles anode coated different thickness of SiOx at discharge/charge current densities of 210 mA/g between voltage 5 mV and 2V.

Figure 2.17. Then the cycle performances of the prepared Si nanoparticle anode are shown in Figure 2.18. As we can see in Figure 2.18, when the coating becomes too thick, i.e. 10 nm, the performance of the anode is the worst, which has a specific capacity of only 200 mAh/g. However, when there is only native oxide layer on the Si anode, the decay of the capacity becomes fast. It turns out that when the thickness of the SiOx coating is 5 nm, the anode has the best performance, i.e. high specific capacity and slow capacity decay, which denotes the existence of optimal coating thickness when we have the desired performance.

To understand the mechanism behind the existence of optimal coating thickness, a chemomechanical model similar to that in section 2.3 is used to simulate the lithiation process of Si nanoparticles in finite element analysis software, Abaqus 6.13. To simplify the simulation, an asymmetrical model with circular shape is constructed. Furthermore, due to symmetry, only ¼ of the model needs to be considered, while symmetrical boundaries

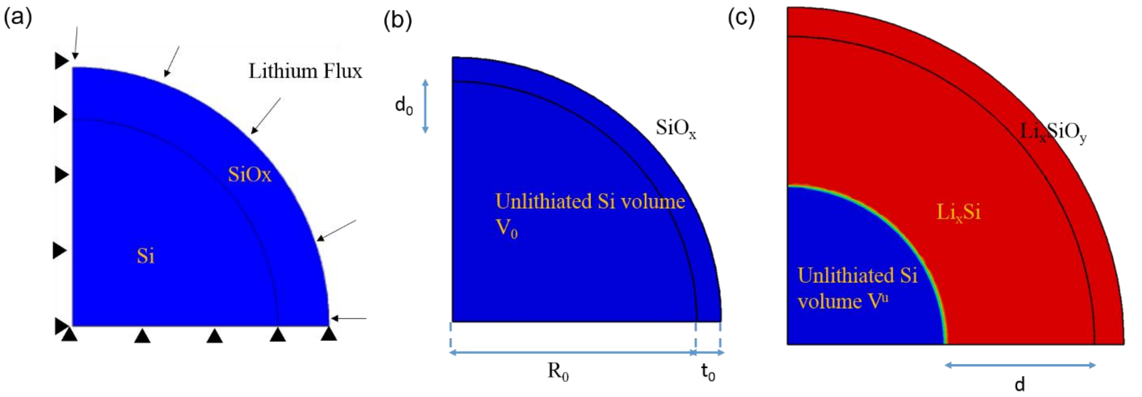

Figure 2.19 Model setup and parameter definitions in the model. (a) ¼ asymmetrical model with symmetrical boundary at x and y directions. The lithium flux is applied on the surface of SiO_x coating; (b) The initial radius of Si is defined as R_0, the initial thickness of coating is t_0 and the initial volume of Si is defined as V_0; (c) The final state of the Si and coating when the lithiation stops due to self-limit effect. The unlithiated Si is defined as V^u.

are applied on the cutting edges, as shown in Figure 2.19a. To be consistent with the expansion of about 245% at full lithiation. However, due to the lack of quantitative data of chemomechanical properties of lithiated Si and SiO_x coatings, the elastic modulus lithiated Si is simply interpolated between 100 GPa and 40 GPa, with pristine Si being 100 GPa and the yielding stress is also interpolated between 5 GPa and 1 GPa, with pristine Si being 5 GPa; the lithiated SiO_x has constant elastic modulus of 90 GPa. The conductivity of the SiOx coating is assumed to be constant and the conductivity of Si is assumed to be dependent on the lithiation state as well as the pressure, namely, $D = D_0 \exp(-\frac{\sigma_p \Omega}{RT})(3.9c - \frac{1}{(1-c)})$, where c is the lithium concentration, Ω is the activation volume of lithium diffusion, σ_p is the pressure and D_0 is a conductivity constant. To account for the self-limit effect, a maximum compressive pressure when the lithiation stops is chosen. Due to the lack of stopping criteria, the maximum pressure is chosen arbitrary, i.e. 2.5 GPa and 4.0 GPa are used to investigate the effect of self-limit.

As shown in Figure 2.20a, the fraction of unlithiated Si volume decreases as the coating thickness increases, due to the constraint effect of coatings, i.e. the thicker the coating is, the higher compressive stress will occur in the both the lithiated Si and unlithiated part, which will in turn slow down the lithium diffusivity until reaching the allowed maximum compressive stress. Also larger stopping pressure will lead to lower fraction of unlithiate Si, since larger stopping pressure would allow would allow more lithiation of Si anode with non-zero conductivity. On the other hand, although thinner coating impose less constraint onto the lithiation of Si anode, it results in larger hoop stress onto the surface of coating, as shown in Figure 2.20b. It is worthwhile to mention that the hoop stress is plotted here instead of the maximum hoop stress in the interface between Si anode and SiO_x coating, as shown in Figure 2.21b. This is due to the observation that most of the fracture in the coating occurs in the surface instead of in the interface. Correspondingly, a larger stopping pressure in the Si anode would also induce a larger hoop stress in the coating surface, due to larger volume expansion from the lithiation of Si anode. As a result, the competing effect from the coating fracture due to high tensile hoop stress and the low lithiation volume of Si anode due to the constraint from coating will lead to an optimal thickness of SiO_x coating, as depicted in Figure 2.20c, which corresponds to an optimal capacity and capacity decay rate. In general, when the coating thickness is too thin, then relatively large capacity can be reached initially (larger fraction of lithiation), as shown in Figure 2.19. However, high tensile stress induced in the coating surface is very likely to cause fracture in the coating, which will in turn no longer protect the SEIs and thus results in a fast decay of capacity. To the other limit, when the coating is very thick, then the tensile stress in the coating surface may be kept in a low enough level to fracture

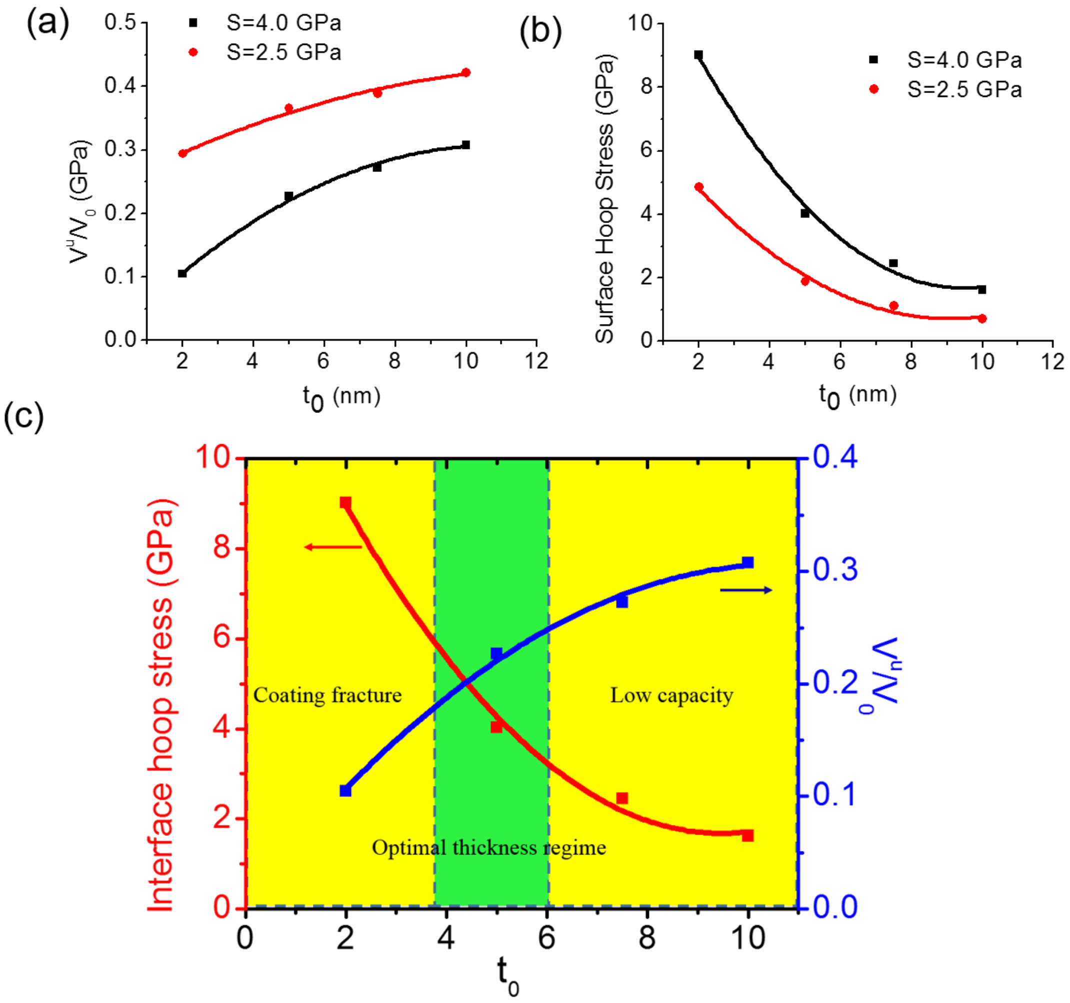

Figure 2.20 Competing effect from self-limit lithiation and coating fracture. (a) The percentage of unlithiated Si as a function of coating thickness t_0 at two different stopping pressures, namely 2.5 GPa and 4.0 GPa; (b) The hoop stress on the surface of lithiated SiO_x coating as a function of coating thickness t_0 when the lithiation stops at two different stopping pressures. (c) A competing effect from self-limit and coating fracture resulting in an optimal thickness regime for S = 4.0 GPa.

the coatings, thus the capacity decay is lower compared with the decay when the coating effect, as shown in Figure 2.20a. What's worse, although SiO_x coating also contributes to the capacity, the capacity of SiOx is lower than that of Si and the lithium conductivity of SiO_x would always limit the rate of the batteries. Therefore, an optimal coating thickness

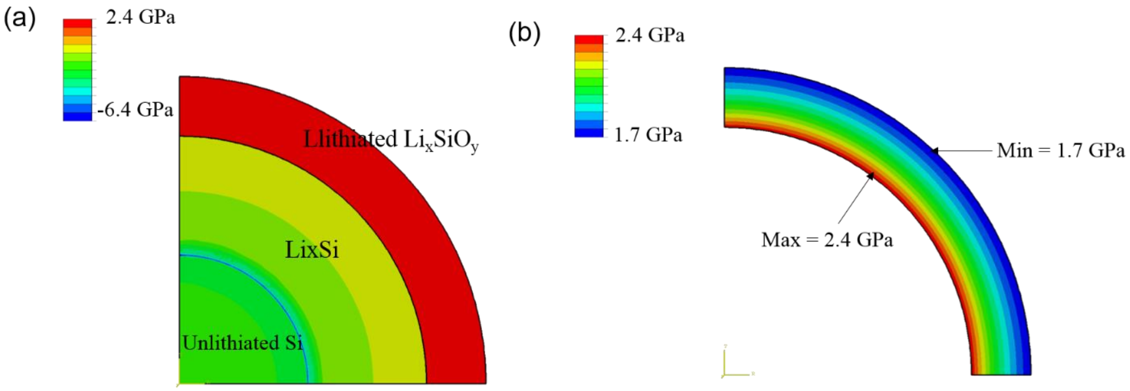

Figure 2.21 An example showing the hoop stress distribution. The Si anode has 20 nm in radius and the thickness of coating is 5 nm. (a) The hoop stress distribution of the whole model, showing the maximum stress occurs in the coating; (b) the hoop stress distribution of the SiO_x coating, showing the maximum stress on the interface between Si and SiO_x.

would not only protect the SEIs and thus alleviate the capacity decay, but also allows reasonable high usage of active materials and reasonable rate of charge/discharge.

To summarize, in the work, we studied the SiO_x coating effect on the performance of Si nanoparticle anode with mot in-situ TEM and chemomechanical model. Specifically, it is found that when too thin coating thickness would induce fracture on the coating surface and thus results in fast capacity decay; while the coating is too thick, the utilization of active material become low. Therefore, an optimal coating design would be neither too thin nor too thick, which can not only prevent the fracture of coating and reformation of SEIs during cycles, but also provide reasonable high utilization of Si anodes. Our work provides a guidance to the design of high performance lithium ion batteries with high capacity and long life.

2.2 Parallel cells and mixture cathode

2.2.1 Continuum model for parallel cell

The experimental setup is shown in Figure 2.22a. Two half cells (A and B) with NMC as cathode material are paralleled. The major difference between cell A and cell B is the amount of carbon black, which affects the electronic conductivity of cathode material. In cell A, carbon black takes up 5% of the total weight solid phase material in cathode, while cell B has 10% of carbon black in mass. For convenience, we denote the current through cell A and B as I^A and I^B respectively, and the total current under control as in Figure 2.22 b as I.

Basically, continuum model developed by Newman and coworkers[9, 52] is adapted here to develop the model for parallel cells. As followed, the main equations are reviewed.

$$i_2^A = -\kappa^A \nabla \Phi_{ele}^A + \frac{2\kappa^A RT}{F}\left(1+\frac{\partial f^A}{\partial \ln c^A}\right)(1-t_+^{\,0})\nabla \ln c^A \tag{2.7}$$

$$I^A - i_2^A = -\sigma^A \nabla \Phi_s^A \tag{2.8}$$

$$i_2^B = -\kappa^B \nabla \Phi_{ele}^B + \frac{2\kappa^B RT}{F}\left(1+\frac{\partial f^B}{\partial \ln c^B}\right)(1-t_+^{\,0})\nabla \ln c^B \tag{2.9}$$

$$I^B - i_2^B = -\sigma^B \nabla \Phi_s^B \tag{2.10}$$

$$I^A + I^B = I \tag{2.11}$$

$$\Phi_s^B(L^B) - \Phi_s^A(L^A) = 0 \tag{2.12}$$

In Equation (2.7)-(2.12), i_2^A and i_2^B denote the current in electrolyte, κ^A and κ^B are the ionic conductivity of electrolyte, Φ_{ele}^A and Φ_{ele}^B are the electronic potential in electrolyte (electrolyte potential), c^A and c^B are the effective electrolyte concentration, f^A and f^B the mean molar activity coefficient of electrolyte, t_+^0 the transference number of anion, σ^A and σ^B the electronic conductivity of active material, Φ_s^A and Φ_s^B the electronic potential in solid electrode (electrode potential), $\Phi_s^A(L^A)$ and $\Phi_s^B(L^B)$ are the electric potential at current collector of cathode side.

2.2.2 Preliminary results and discussion for parallel cell

Electronic conductivity of NMC cathode is assumed to be concentration dependent. Figure 2.22b shows an estimation of the dependence of electronic conductivity on the state of concentration (SOC), which is achieved via Electrochemical Impedance Spectroscopy (EIS). Generally speaking, the higher SOC is, the lower electronic conductivity, which is in agreement with previous study[150]. Figure 2.23c-2.23f shows the preliminary results for current distributions in the two paralleled cells with current ranging from C/5 to 2C, with the same cut off voltage of 4.4 V and 2.5 V. Two trends can be observed: 1) initially currents in cell A and cell B differs significantly due to the distinctions in electronic conductivity; however the two currents tend to converge as time goes on, and diverges after two currents cross; 2) currents in the two paralleled cells converge faster at lower rate. To understand the trends, models developed in part 2.2.1 are implemented in COMSOL 5.2. The simulation results are shown in Figure 2.23, which in general are in good agreement with that from experiments. To increase the accuracy of predictions of the model, the estimation of electronic conductivity should be improved. Also, since the resistance

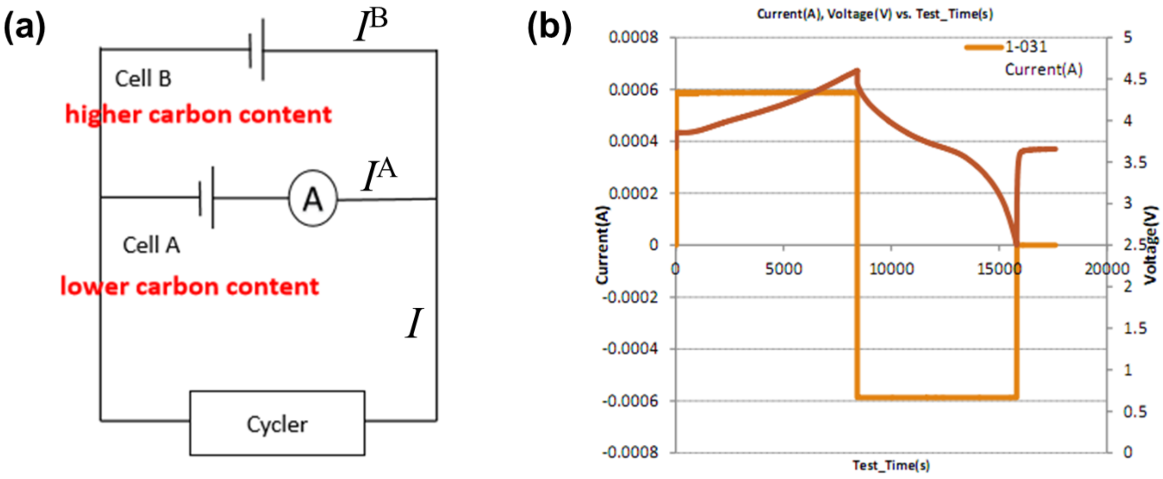

Figure 2.22 Experimental setup for parallel cells. (a) A schematic view of parallel cells. (b) Voltage variation with time, when current is controlled during charge and discharge process. The voltage cutoff is 4.4 V and 2.5 V, respectively.

coming from charge transfer is not easy to correlate with the ion diffusivity within the solid particles, more careful treatments should be considered in the future.

To understand the current distributions between the two cells, Figure 2.24 plots out the distribution of electrode potential, electrolyte potential, and electrolyte currents for both cells at 1C and 2C current loading at end of charge process. Through Equation (2.7)-(2.10), we can see that the total current in each cell is mainly determined by the gradient of electrode potential, electrolyte potential and electrolyte concentrations. And the electronic conductivity and ionic conductivity also play a role in the current distribution between the two cells. We notice that from Figure 2.24b and Figure 2.24c, there is no significant difference between the gradients of electrolyte potential or electrolyte concentration for the two paralleled cells. Thus to make things easier, we may only need to focus on the distribution of electrode potentials in the two cells. As shown in Figure 2.24a, at current loading of 1C or 2C, the cell with higher electronic conductivity leads to shallower gradient of electrode potential than that of lower electronic conductivity. On the other hand, higher current may also result in more inhomogeneous concentration distributions, which cause steeper gradient of electrode potential. However, as a matter of fact, before the currents in the two cells cross, the gradient of electrode potential would always steeper in cell of lower electronic conductivity, due to the potential constraint at the current collector. Once the currents in the two cell cross, the average SOC in the cell with lower electronic conductivity is still much higher than that in higher-electronic-conductivity cell, which indicates steeper electrode potential. This will thus lead to divergence of current in the two cells, as we can see in Figure 2.23c-2.23e.

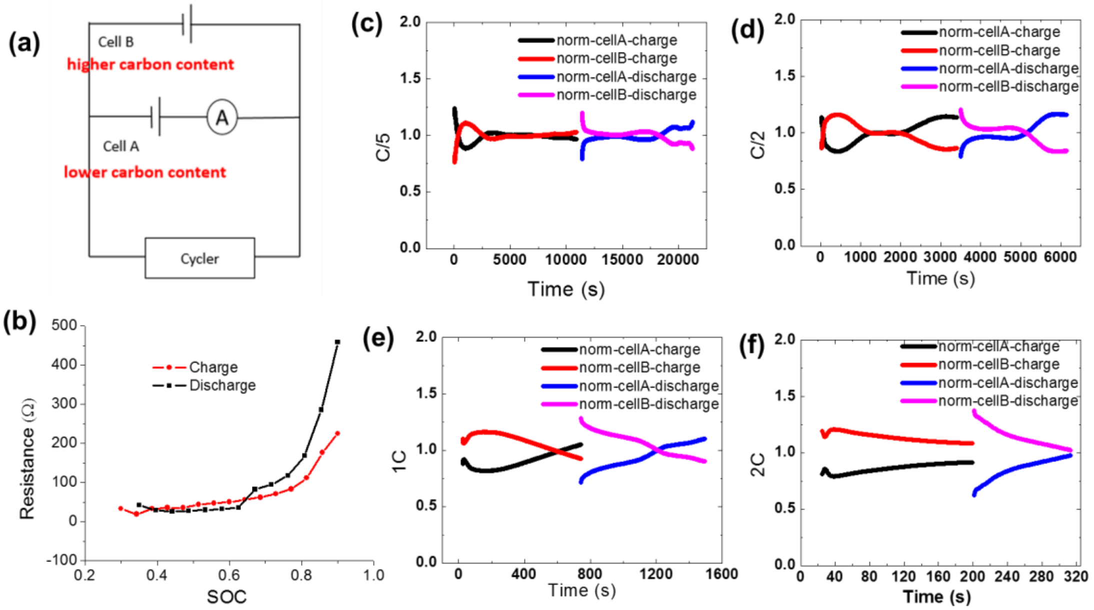

Figure 2.23 Preliminary results for current distributions with rate ranging from C/5 to 2C. (a) A schematic view of parallel cells. (b) EIS measurement of cell resistance as a function of SOC for both charge and discharge process. (c)-(f) Current distributions in cell A and cell B under rate of C/5, C/2, 1C and 2C, respectively.

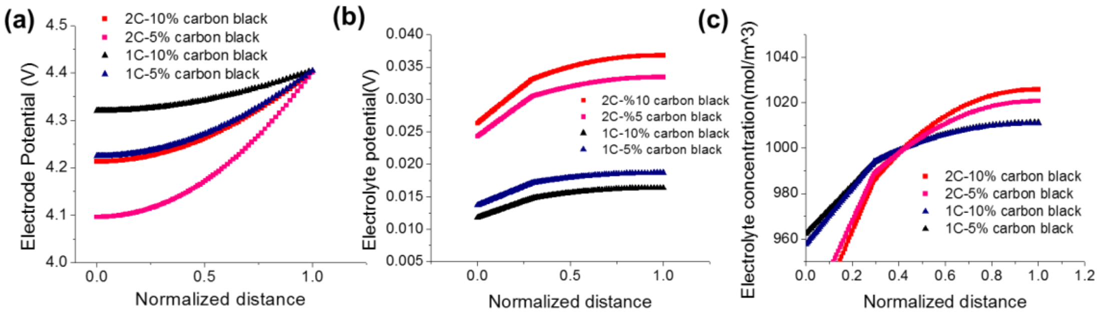

Figure 2.24 (a)-(c) Distributions of electrode potential, electrolyte potential and electrolyte concentrations at end the charge process.

2.2.3 Mixture cathode

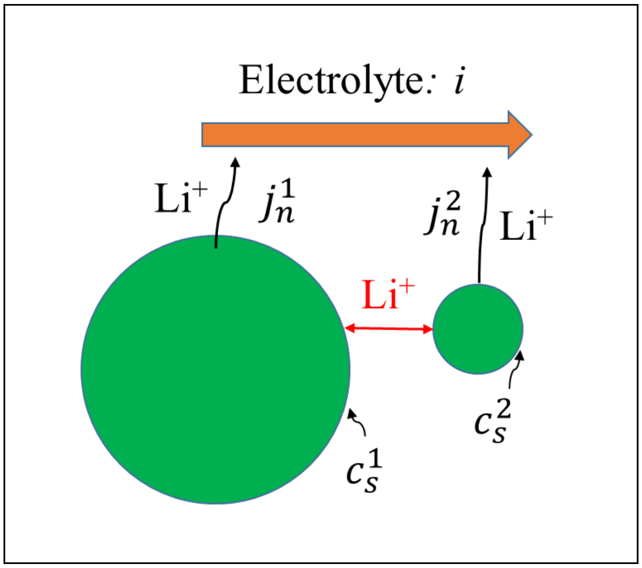

Figure 2.25 A schematic illustration of ionic exchange between two particles of different size.

In this part, model is in development. To account for the fact that bulk solid particles can exchange lithium ion with nano solid particles, the solid diffusion equations for both nano and bulk solid particles need to be modified. That is to say, except for the ion exchange between particle and electrolyte, the ion exchange at surface of the particles must account for the exchange between particles, as shown in Figure 2.25. The intended modification is shown as followed in Equation 2.13 and 2.14.

$$-D_s^i \frac{\partial c_s^i}{\partial r} = j_n^i + k^i f(c_s^1(R^1), c_s^2(R^2)) \tag{2.13}$$

$$\frac{\partial i_2}{\partial x} = \sum A^k i_n^k \tag{2.14}$$

In the right hand of Equation 2.14, ion exchange between particles are denoted with a function of surface concentration of the two sized particles. k^i is the constant coefficient accounting for the contact area between the two sized particles. Thus A^k, the exposure area to electrolyte, should be modified accordingly. f function and the corresponding coefficients need to be determined later through the integration with experiments.

CHAPTER 3. BARRIER LAYERS IN FLEXIBLE ELECTRONICS

Time-dependent cracking is crucial in determining the lifetime of devices, given that it may further decrease the allowable applied strains if held over long periods of time. In fact, Suo and co-workers demonstrated that time-dependent cracking of an elastic film made of a material that does *not* undergo any subcritical cracking (i.e., no environmentally-assisted cracking nor stress corrosion cracking) can occur if a viscous underlayer (i.e., a layer that undergoes creep) is present between the film and an elastic substrate [76-79]. The physical explanation relies on the following fact: as the underlayer creeps, the stress field in the field relaxes in the crack wake, resulting in a decreased constraint effect of the underlayer on the film and therefore an increased driving force for crack extension (i.e., the stress field around the crack tip intensifies). If over time the driving force exceeds a critical value, crack extension occurs; after some amount of cracking, the driving force is reduced due to a larger constraint effect of the underlayer that has not crept yet. The process can repeat itself, and a steady state crack velocity is attained. Clearly, a similar cracking scenario can occur for thin barriers on polymer substrates under tensile strains, depending on the viscous properties of the polymer. Here, we studied the time-dependent crack growth properties of SiN_x

coatings on polyethylene terephthalate (PET) substrates by considering both polymer creep and subcritical cracking of the SiN_x films. Figure 3.1a and 3.1b shows snapshots of cracking extension at 0.6% and 0.7% strain. Figure 3.1c shows the general setup for the experiments and loading scheme. A preliminary study on the relaxation behavior of PET is shown in Figure 3.1d, where only 5% strain relaxation is significant.

3.1 Elastic-viscoplastic model (*Reprinted with permission from Ref*[151]*. Copyright 2016 American Chemical Society*)

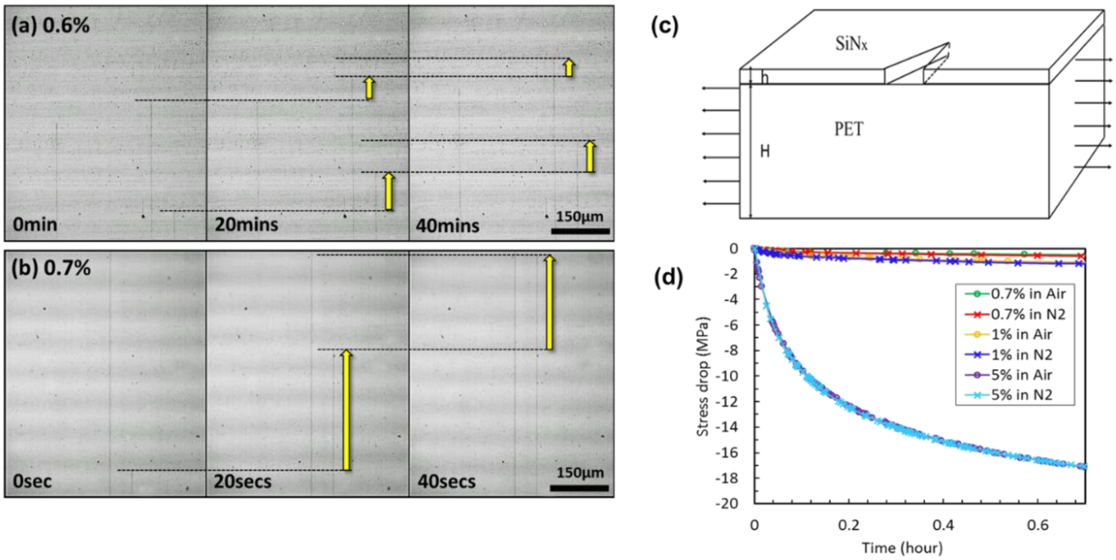

Figure 3.1 Example of time-dependent channel crack growth in 250-nm-thick SiN_x in air at strain values of (a) 0.6 and (b) 0.7%, respectively. (c) Schematic of the crack model. The SiN_x thin film is perfectly bonded to the PET substrate, h/H = 1/100. (d) Stress relaxation curve for PET at strain of 0.7%, 1% and 5% under air and N_2 conditions.

We evaluated the energy release rate for a long crack in a SiN_x thin film on a PET substrate by using the finite element package ABAQUS.[152] To this end, we adopted a linear elastic model for SiN_x and an elastic-viscoplastic model for PET. The latter allows us to account for plastic yielding and viscous relaxation that may occur in a highly deformed region of PET near the crack. In the 1D representation of a 3D elastic-viscoplastic model, the total strain rate $\dot{\varepsilon}$ is given by

$$\dot{\varepsilon} = \dot{\varepsilon}_{\mathrm{e}} + \dot{\varepsilon}_{\mathrm{p}} \tag{3.1}$$

Here, the elastic strain rate $\dot{\varepsilon}_{\mathrm{e}}$ is linearly proportional the stress rate $\dot{\sigma}$ according to: $\dot{\varepsilon}_{\mathrm{e}} = \dot{\sigma}/E_s$. The plastic strain rate $\dot{\varepsilon}_{\mathrm{p}}$ is given by a Cowper-Symonds overstress power law[152]

$$\dot{\varepsilon}_{\mathrm{p}} = D\left(\frac{\sigma}{\sigma_{\mathrm{Y}}(\varepsilon_{\mathrm{p}})} - 1\right)^{n} \tag{3.2}$$

where D and n are the material constants, $\sigma_{\mathrm{Y}}(\varepsilon_{\mathrm{p}})$ is the yield stress that depends on the total yield strain ε_{p}. We determined the viscoplastic parameters of PET by fitting both the tensile stress-strain curve and the stress relaxation curve from experiments, and obtained D = 80 hour^{-1}, n = 20 and $\sigma_{\mathrm{Y}}(\varepsilon_{\mathrm{p}}) = 50\mathrm{MPa}\times(1+1.74\varepsilon_{\mathrm{p}})$. Figures 3.2(a) and (b) show that the fitting curves are in close agreement with the experimental results of PET.

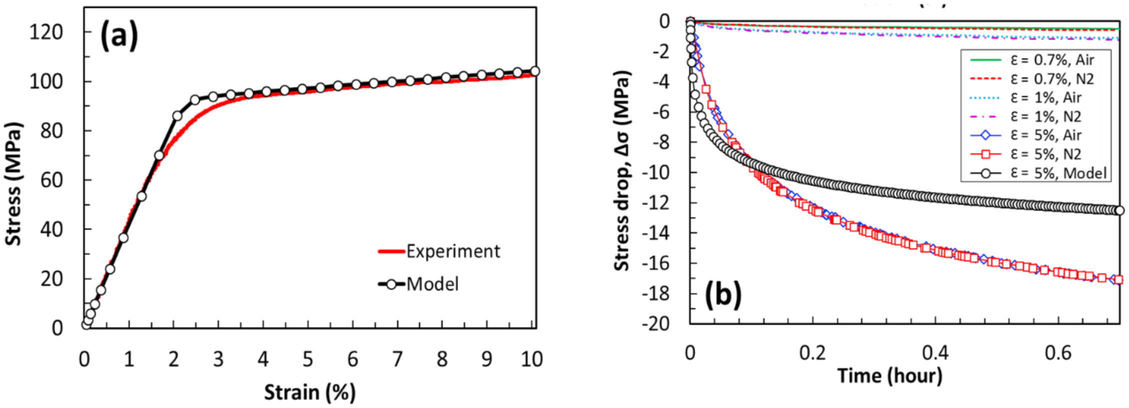

Figure 3.2 (a) Stress-strain curve of PET substrate. (b) Stress relaxation curves of PET substrate.

3.2 Time dependent cracking in SiN_x thin film within short time period (*Reprinted with permission from Ref*[151]*. Copyright 2016 American Chemical Society*)

Figure 3.3a and 3.3b shows the schematic of our finite element model for evaluating the steady state energy release rate G_{ss} of a long crack in a SiN_x thin film on a PET substrate.

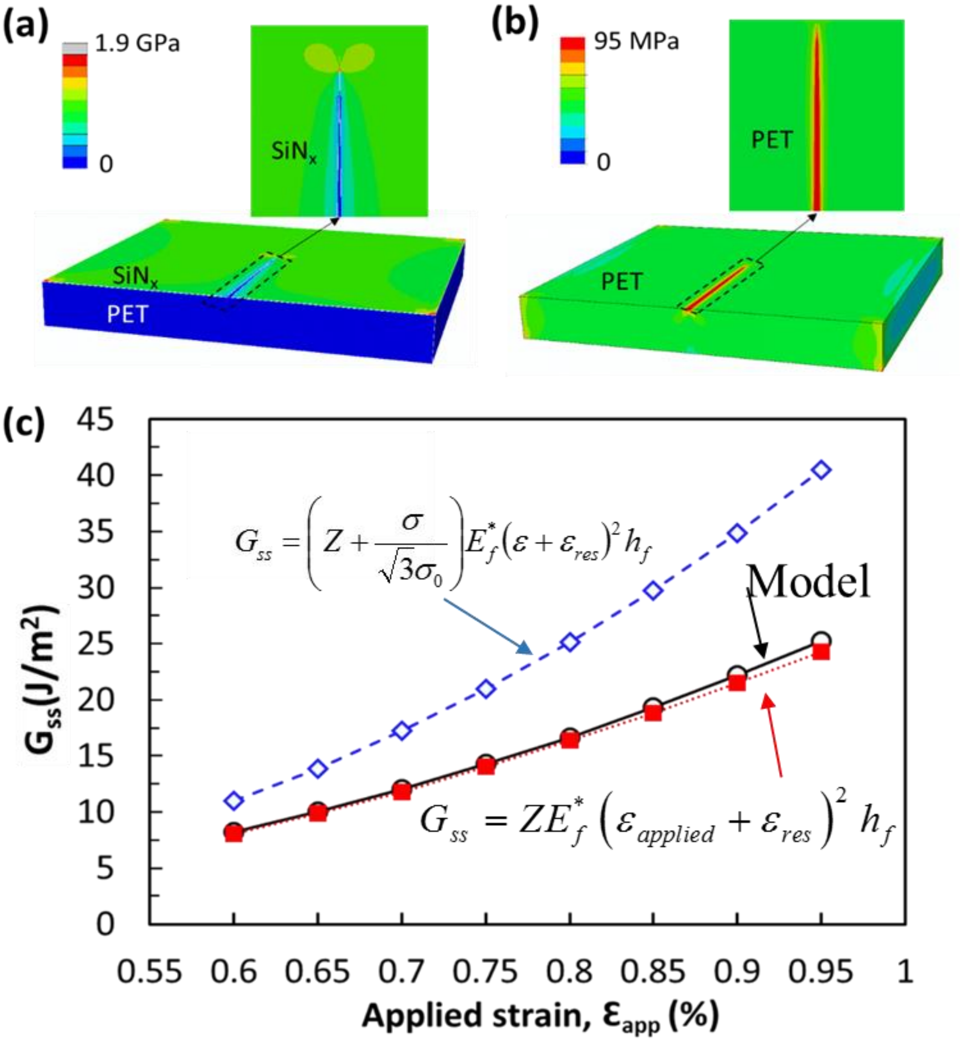

Figure 3.3. Finite element model and results. (a) The von Mises stress contour in SiN_x thin film and PET substrate (lower image) and magnified view of stress concentration around the crack tip in SiN_x thin film (upper image). (b) The von Mises stress contour in PET, where high stresses develop beneath the crack wake in PET. (c) Calculated G_{ss} versus ε_{app}, compared to Eqs. 3.3 and 3.6.

In this model, a 250-nm-thick SiN_x film is perfectly bonded with a 25-μm-thick PET substrate. The in-plane geometry of the film and substrate is $180 \times 180 \mu m$. The compressive residual stress in the SiNx is taken into account. A 90-μm-long wedge crack was created in the middle of the SiN_x thin film. We calculated the stress and strain distributions in the cracked system by imposing a displacement-controlled load on the substrate (corresponding to an applied strain rate of 0.027% s^{-1}), and then evaluated G_{ss} using the J-integral approach.[153]

To evaluate the driving force for cracking, a time-independent formula of driving force for multilayer cracking was used here for comparison[154]:

$$G_{ss} = \frac{Z\sigma^2 h_f}{E_f^*} = \frac{Z(\sigma_{applied} + \sigma_{res})^2 h_f}{E_f^*} = ZE_f^*(\varepsilon_{applied} + \varepsilon_{res})^2 h_f \tag{3.3}$$

where σ, $\sigma_{applied}$ and σ_{res} are the total, applied and residual stress in the film, respectively, $\varepsilon_{applied}$ and ε_{res} are the applied and residual strains in the film, E_f^* and h_f are the plane strain elastic modulus and thickness of the film, and Z is the dimensionless energy release rate which depends on the elastic mismatch, α, between the film and substrate:[66]

$$\alpha = \frac{E_f^* - E_s^*}{E_f^* + E_s^*} \tag{3.4}$$

where E_s^* is the plane strain substrate elastic modulus. Numerical models can provide the value for Z as a function of α.[66, 155, 156] The energy release rate G_{ss}, is related to the stress intensity factor K ahead of the crack by the following relationship:[157]

$$K = \sqrt{G_{ss} E_f^*} \tag{3.5}$$

with no sign of delamination. However, for a specimen tested at 0.7% for 5 days, the crack tip was observed to be several micrometers deep inside the PET substrate from the interface, suggesting cracking of the substrate for these long periods of time. In this study, we focus on the time- Equation 3.3 is only valid for the following conditions: the channel crack front width corresponds to the film thickness (i.e., the crack does not penetrate into the PET substrate, nor does it delaminates at the interface), the crack is isolated on a semi-infinite substrate, and both substrate and film exhibit a linear elastic behavior. Using cross-section SEM images, the crack tip was confirmed to sit at the film/substrate interface for a specimen tested at 0.7% for 30 minutes, dependent crack growth behavior over short periods of times (<30 minutes) for which the crack tip remains at the interface (i.e., Equation 3.3 is valid). Using the measured E_s^* and E_f^* values (see Table 3.1), the elastic mismatch is $\alpha = 0.934$, corresponding to the dimensionless energy release rate $Z = 13$.[156] Huang et al studied the effects of substrate finite thickness and channel cracks interactions on the driving force G_{ss}.[156] For $\alpha = 0.95$ (value similar to our bi-material system), they showed that the semi-infinite substrate case can be approximated for $H/h > 60$, a condition obtained for our 125-μm-thick PET / 250-nm-thick films ($H/h = 500$). G_{ss} is also largely unaffected by neighboring cracks as long as the normalized crack spacing, S/h, is larger than 150, which corresponds in our case to crack spacings S of 37.5 μm. A significant number of the cracks that we observed meet this criterion. Therefore we did not consider neighboring crack interaction in the calculation of G_{ss}. Figure 3.2a shows that the PET substrate deforms plastically for strains larger than 2.5%.

Table 3.1. Mechanical properties of PECVD SiN_x film and PET polymer substrate

mechanical properties (units)	PECVD SiN_x film	mechanical properties (units)	PET polymer substrate
E_f (GPa)	123 ± 5.8	E_s^* (GPa)	4.47 ± 0.25
ν_f	0.253	σ_0 (MPa)	90.6
E_f^* (GPa)	131 ± 6.2	D (hr^{-1})	80
ε_{res} (%)	- 0.15 ± 0.02	n	20
		σ_y (MPa)	$50\times(1+1.74\varepsilon_p)$

Although all the applied strains in this study are less than 1%, however the local strains in the PET ahead of the cracks in the SiN_x coating are much larger, and non-negligible local yielding likely occurs in the substrate. Hence, Equation 1 needs to be modified to account for the increase in driving force due to local yielding in the substrate, which Hu and Evans estimated to be:[158]

$$G_{ss} = \left(Z + \frac{\sigma}{\sqrt{3}\sigma_0} \right) E_f^* \left(\varepsilon + \varepsilon_{res} \right)^2 h_f \tag{3.6}$$

where σ is the stress in the coating ($\sigma = E_f \times (\varepsilon_{appl} + \varepsilon_{res})$) and σ_0 is the yield stress of the substrate (σ_0 = 90.6 MPa). Comparing Equation 6 to 1, the driving force G_{ss} is larger by 30 to 60% due to the local yielding of the substrate, as shown in Figure 3.3d for the range of studied applied strain. Finite element modeling was used to assess the accuracy of Equation 3.6. Figure.3.3b shows the von Mises stress contour in the system at an applied strain load of 0.95% with a compressive residual strain of ε_{res} = -0.15% in the SiN_x thin film (corresponding to 195 MPa residual stress). Stress concentration occurs near the crack tip in SiN_x, in spite of the constraint from PET underneath.[77] Figure 3.3c shows the von Mises stress contour in the PET at the same load. It is seen that high stresses develop in the PET beneath the crack wake. Under the 0.95% applied strain, the far-field stress in the PET is only about 40 MPa, while the stress in PET underneath the crack wake reaches 95 MPa, indicating that plastic yielding has occurred in this part of PET. Such local plastic deformation in PET arises due to the opening displacement of the crack face. And it in turn allows for a larger crack opening than that an elastic PET model would predict. This result underscores the importance of incorporation of plastic yielding in the model. Based on the crack-tip field, we obtained the corresponding $G_{ss} = 25.2$ N/m using the J-integral approach in ABAQUS. In comparison, the value obtained for this system using Equation 2.3.6 is $G_{ss} = 40.5\ \mathrm{N\ m^{-1}}$ (see Figure 3.3d). This discrepancy arises from the fact that the shear stress in the PET near the interface is non-uniform (from our finite element results) and hence the simplified shear lag model[158] with a constant interface shear yield strength is not applicable to the present case. In the following results, the modeling curve shown in Figure 3.3d is deemed more accurate and therefore used to evaluate G_{ss} as a function of the applied strains for the 250-nm-thick SiN_x films.

Figure 3.3b also shows significant amount of stress relaxation of the PET for strains of 5%, which is likely to occur locally ahead of the crack tips. As explained in the introduction, the creep of a viscous sublayer induces time-dependent crack growth in the film. Huang *et al.* studied analytically and numerically the increase in driving force with time for several crack geometries.[77] The numerical solutions only apply for thin viscous sublayers for which a shear lag model could be used. For thick viscous layers (as is the

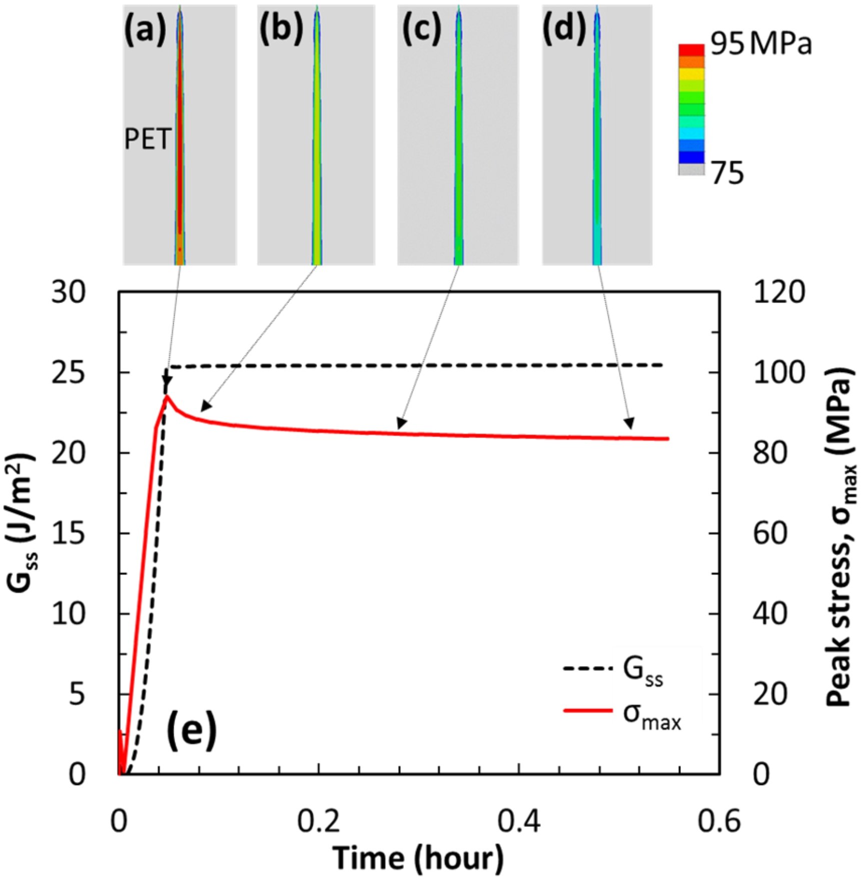

Figure 3.4 Time evolution of energy release rate and stress beneath the crack wake in PET. (a-d) The von Mises stress contour in PET at different times as indicated in (e), showing the viscous stress relaxation effect. (e) Peak stress in PET and corresponding energy release rate for film cracking as a function time.

case with our PET substrate), a 3D viscous flow problem needs to be solved numerically to calculate the driving force, which was done with our numerical model. Specifically, the simulated crack system was held at the applied strain of 0.95% for 0.5 hour. Figures 3.3a-d show the evolution of stress distribution in PET beneath the crack wake. Figure 3.3e shows the corresponding peak stress as a function of time, which drops from 95MPa at time $t = 0$ to 82 MPa at $t = 0.5$ hour. However, such viscous stress relaxation in PET has a minor influence on the increase of G_{ss} in the SiN_x thin film; as shown in Figure 3.4e, G_{ss}

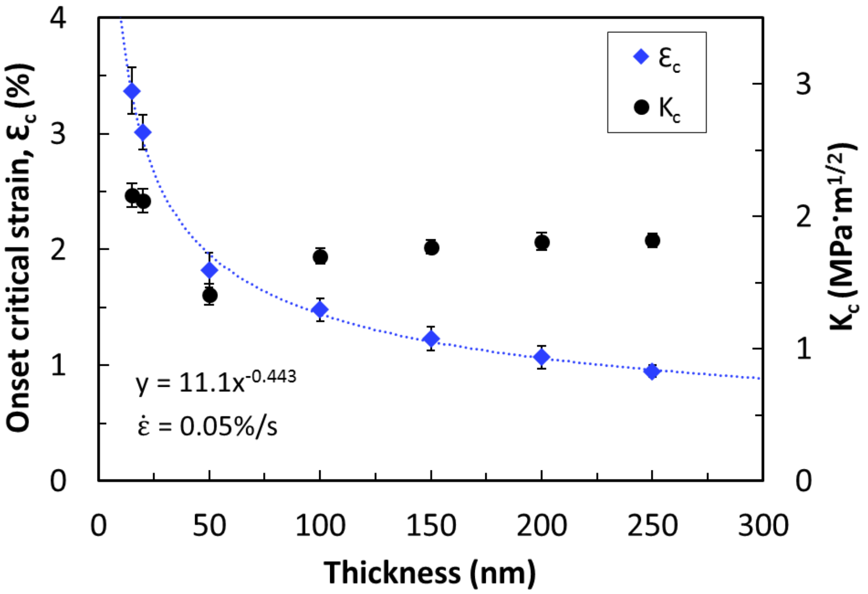

Figure 3.5. Influence of thickness on ε_c and K_c for SiN_x on PET substrate.

increases slightly from 25.2 N/m at *t* = 0 to 25.4 N/m at *t* = 0.5 hour. Therefore, the effect of viscous relaxation on G_{ss} is negligible at the low strain load less than 1% within the time scale of 0.5 hour.

Figure 3.6 shows the measured onset critical strain as a function of the applied strain rate in laboratory (humid) air and dry air environments. The results clearly show that ε_c is a function of both the applied strain rate and environmental condition. In humid air, the onset critical strain decreases from 0.95 ± 0.02 to 0.75 ± 0.03% by decreasing the applied strain rate from 10^{-1} to 3×10^{-4} %·s^{-1}, while in dry air, the corresponding decrease in onset critical strain was only from 0.95 ± 0.01 to 0.88± 0.03 %. The lower measured onset critical strains for lower strain rates suggest time-dependent crack growth (channel cracking) of existing cracks that would be on the order of the timescale for the test observation. As the strain rate is increased above 0.01 %.s^{-1}, the onset crack strain becomes independent of the environment. The effect of strain rate on the apparent onset critical strain is consistent with the study by Guan *et al.*,[86] and the effect of humidity on time-dependent crack growth is consistent with the study by Vellinga *et al.*[85] Both studies demonstrated environmentally-assisted cracking of the SiN_x coatings on PEN polymers. Here, the crack growth rates and behavior were further characterized as a function of applied strains (from 0.6 to 0.85%) / driving forces (see numerical model in Figure 3.3c for corresponding G_{ss}), in different environments (laboratory air, dry nitrogen, dry air). In our calculations, we ignored the effects of hygroscopic expansion on K. Based on a coefficient of hygroscopic expansion of 8×10^{-6} $\%^{-1}$ RH for our PET, we approximate an increase in applied strain of 0.024% from a dry environment to laboratory air (~30% RH). This results in a small decrease in the applied stress in the case of displacement-controlled tests in laboratory air compared to dry environments. The effect on Z (and therefore on the driving force) is deemed negligible (the elastic mismatch, $\alpha = 0.934$, increases by ~0.2% in laboratory air).

The in-situ crack growth observations confirmed a different behavior depending on the humidity content (no difference was observed between dry air and dry nitrogen). First of all, the number of growing cracks was significantly larger in humid air compared to dry nitrogen (see Figure 3.7b), with more than ten times more cracks in the humid environment at both 0.6 and 0.7% applied strains. The cracks were also observed to grow faster (by ~1 order of magnitude) in the humid environment. As shown in Figure 3.7a, the average measured crack growth rates were also highly sensitive to the driving force K (i.e., applied strain), thereby explaining the aforementioned strain rate effects on onset critical strain. For example, in humid air, the crack growth rate at $\varepsilon_{app} = 0.75\%$ ($K = 1.37$ MPa $m^{0.5}$) is ~58.7 ± 38.4 μm s^{-1}, which would explain the observed decrease in onset critical strain

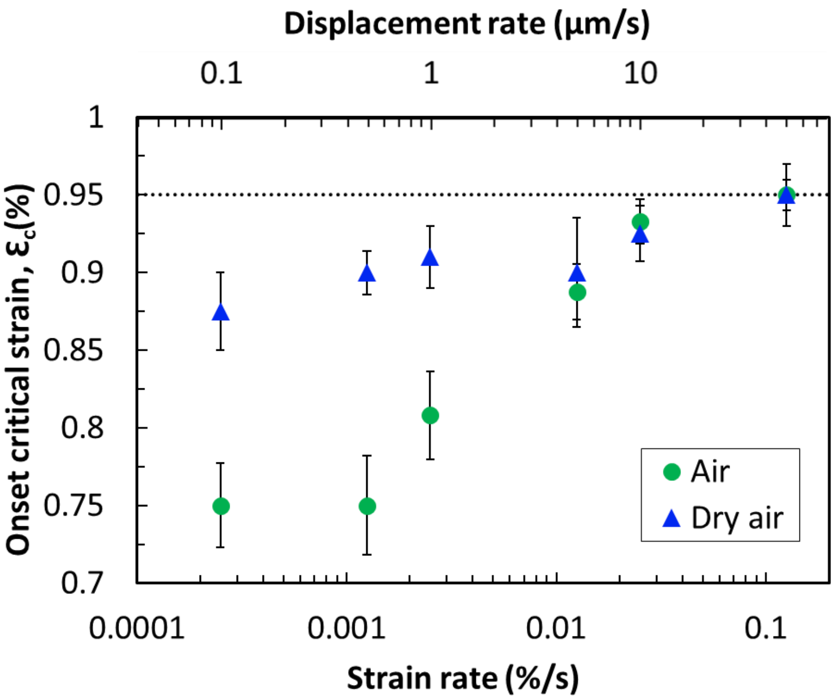

Figure 3.6. Effect of strain rate on onset critical strain of 250-nm-thick SiN_x in air and dry air at room temperature.

from 0.95 ± 0.02 % at an applied strain rate of ~0.1 % s^{-1} (corresponding to a displacement rate of 50 μm s^{-1}) to 0.75 ± 0.03% at an applied strain rate of ~3×10^{-4} % s^{-1} (corresponding to a displacement rate of 0.1 μm s^{-1}). A power law equation was used to fit the data in Figure 3.7a:

$$\frac{da}{dt} = C\left(\frac{K}{K_c}\right)^n \tag{3.7}$$

with the coefficients *C* and *n* listed in Figure 3.7(a) for the three investigated environments. These average rates were only calculated from growing cracks that were not interacting with particles present on the PET substrate before deposition. Figure 3.8 shows the measured length extension over time for four isolated cracks (two different strain levels in dry N_2 and laboratory air) that did not have particles in their path. This figure shows smooth crack growth at constant rates that are consistent with that shown in Figure 3.7a. However, the in situ microscopy observations revealed a drastically different channel crack growth behavior in films where large densities of contaminants/particles were present (the occurrence of these particles depends on the handling of the polymer substrate prior to deposition). In dry N_2, at applied strains of 0.85% (corresponding to stable crack growth of 11.6 ± 5.50 μm s^{-1} in the absence of particles), it was observed that cracks grew in an unstable manner from particles, after an incubation period. The cracks grew unstably until they reached other particles and were arrested. After another incubation period, the cracks would start again propagating in an unstable manner from the particles, until they reached again more particles, and the process repeated itself. The incubation period was measured to increase with decreasing applied strains (from ~250 ± 150s at 0.9% to 900 ± 650s at 0.75%). Importantly enough, this unstable crack growth behavior in the presence of particles was not observed when the tests were performed in laboratory air.

As mentioned above, time-dependent crack growth due to PET creep is unlikely to occur due to the minor effect of PET stress relaxation on the increase of G_{ss} within a timescale of 0.5 hr. Hence, we conclude that environmentally-assisted cracking of SiN_x governs the observed behavior in humid air. Given that the crack growth behavior is similar

chemically active species in the crack growth process (and not oxygen). It is possible that traces of water in the dry environments (~2 ppm) and/or adsorbed water at the surface of the PET polymer before the coating deposition could lead to some amount of environmentally-assisted cracking in these environments. The results also strongly suggest that the presence of water vapor affects the initiation of channel cracks. While a similar

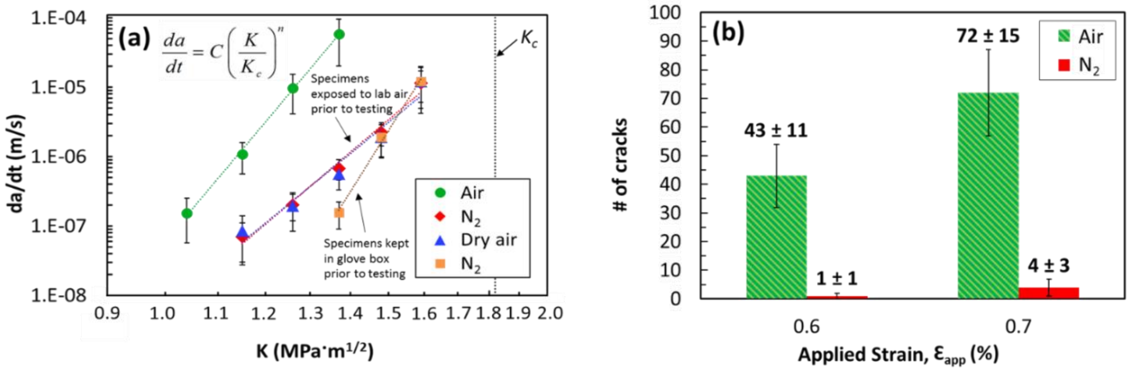

Figure 3.7 (a) Measured crack growth rates of 250-nm-thick SiN$_x$ as a function of stress intensity factor in air (green circle), nitrogen (red diamond) and dry air (blue triangle) and (b) density of cracks in air and in nitrogen measured 30 minutes after first observed crack.

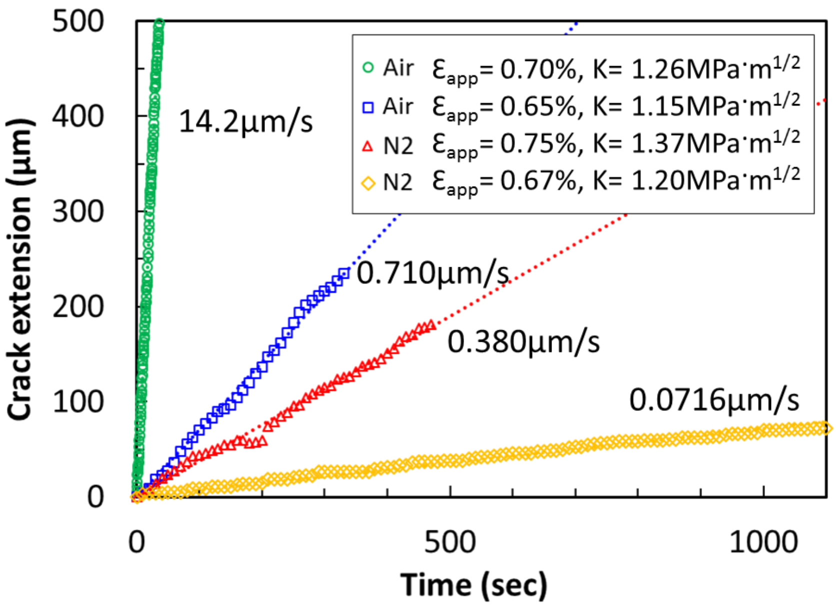

Figure 3.8. Crack extension as a function of time.

crack growth rate (~100 nm·s^{-1}) is measured in humid air at an applied strain of 0.6% (K = 1.0 MPa m$^{0.5}$) and in dry N$_2$ in humid air at 0.7% (K = 1.3 MPa m$^{0.5}$) (see Figure 3.7a), the average measured number of cracks is 43 in air vs 4 in N$_2$ (see Figure 3.7b). A possible explanation is that the environment accelerates the subcritical growth of surface flaws into channel cracks. It is important to keep in mind that Equation 3.1 and 3.6 only apply to the growth of long channel cracks, not their initiation. An underlying assumption often made to use these equations is that the long channel cracks are initially present in the coatings. If it was the case, there should not be ten times more channel cracks in air than in dry N_2 for similar channel crack velocities. Instead, it is more likely that smaller defects, such as surface flaws, are present. These surface flaws are initially surrounded by the hard SiN_x (for example, assume a semi-elliptical surface flaw with a depth less than the coating thickness). When exposed to the environment, these surface flaws may grow in a self-similar fashion thanks to environmentally-assisted cracking until they reach the interface and transition to a channel crack.

The issue of nucleating vs propagating a channel crack may also explain the observed environment-dependent crack growth behavior in the presence of particles (described above). In dry N_2, unstable crack propagation starting from particles occur after an incubation period that increases with decreasing applied strains, a behavior that is not observed in humid air (only stable crack propagation was observed in this environment). A possible explanation is that, as a channel crack is arrested at a particle, polymer relaxation occurs (at a larger rate due to the particle's stress concentration effect), leading to an increasing stress field. Since the channel crack is not present on the other side of the particle (from where the channel crack arrested), it needs to be nucleated. It is possible that the stress required to nucleate the channel crack is, under these conditions, larger than the stress required to propagate the channel crack; hence, once the channel crack is nucleated, the driving force G_{ss} is larger than G_c and unstable crack propagation occurs. This explanation would be consistent with longer incubation periods that were measured for lower applied strains (as it would take more time for intensifying the stress field ahead of the particle). In humid air, unstable crack propagation from particles was not observed (meaning $G_{ss} < G_c$), which could be the result of fast, environmentally-assisted, nucleation of channel cracks, as explained above.

As a concluding remark, the time-dependent results described in this paper need to be restricted to short times (~30 minutes) after channel cracking is first observed. As mentioned at the beginning of the result section, our FIB cross-sections revealed cracking of the polymer at the location of channel cracks. Further study is therefore required to capture the evolution of driving force with time for channel crack propagation in the case of evolving substrate damage, and correlate it with the observed crack growth behavior under much longer time exposures (~days). This knowledge is also crucial to assess the long-term reliability of flexible electronics requiring thin film barriers.

In summary, we have found the use of onset critical crack strain at high strain rate to be insufficient to define the safe operating envelope against channel cracking for SiN_x barrier films on PET substrates, due to time-dependent crack growth. Specifically, it was shown that the channel crack growth in SiN_x barrier films can occur at strain levels 35% below the apparent onset critical crack strain due to environmentally-assisted crack growth. Based on testing 250-nm-thick films on 125-μm-thick PET, it was found that the crack growth rates were higher by a factor of 10 in humid air versus dry nitrogen. It was found that not only were crack growth rates higher in humid air exposure, but that the nucleation of additional channel cracks occurred resulting in also a higher crack density. The increase in channel crack density in humid air is believed to be related to environmental-assisted crack extension of small flaws in the SiN_x films. Numerical models were also instrumental in revealing that the effect of polymer relaxation during the displacement-controlled cracking tests only has a minor effect on time-dependent crack growth. Thus, an understanding of time dependent fracture and the actual loading condition for the barrier film (e.g., fixed strain for a curved device, or time dependent strain for foldable and rollable devices) is necessary to predict the overall safe loading conditions for barrier films for a given expected lifetime of a device. The analysis presented in this work is meaningful since mechanical testing observing time and environmentally dependent crack growth behavior has been performed for the first time in flexible barrier films and yields the appropriate crack driving force parameters and growth rates that can be used to better define the reliability of the coatings. We expect that this approach of testing can be widely used for other thin barrier films since we are able to make visualizations down to 15 nm in thickness.

Simulation methods: Due to stress concentration in both PET and SiN_x thin film, it is necessary to use delicately designed mesh to capture the concentration effect, as shown in Figure 3.9. In detail, the region around crack tip in SiN_x thin film is split into several circular cells, where very fine mesh is used. Also, PET right beneath the crack is also meshed separately from other part of PET. Initially, the width of the densely meshed PET

region is 2 times the crack opening. Furthermore, gradient mesh scheme is used in PET, so that the closer the region is to the crack, the denser the mesh will be. The calculation of energy release rate is based on the calculation of J-integral[159]. However, in our case, J-integral is not path-independent due to the shear force between SiNx and PET. Thus the contour chosen to perform the J-integral calculation should be as close to the crack tip as possible. Additionally, to avoid the stress singularity around the crack tip, the contour

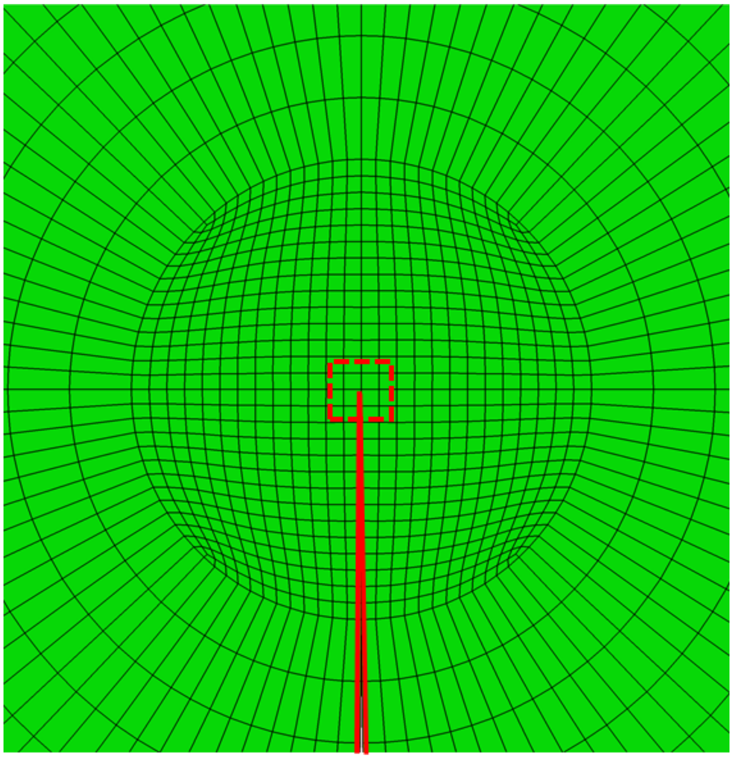

Figure 3.9. J-integral contour (red square) used for calculation of energy release rate of film cracking.

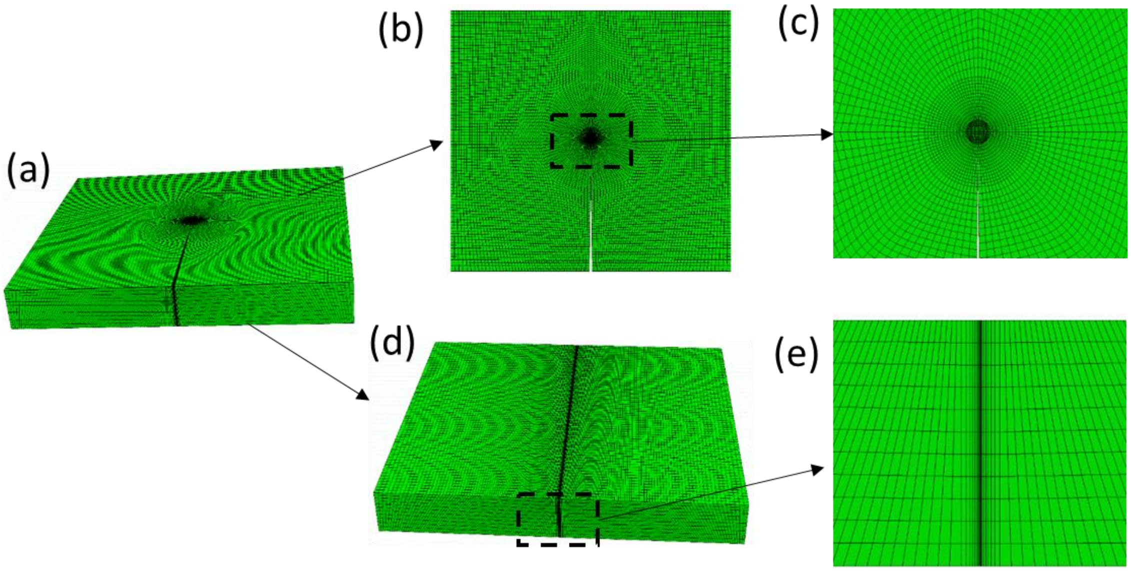

Figure 3.10. Finite element mesh of the crack model. (a) Global view of the mesh in the system. (b) Top view of the mesh of the system. (c) Magnified view of the mesh near the crack tip in SiN_x film. (d) Mesh of PET (e) Magnified view of the mesh in PET underneath the crack.

should not be too close to the crack tip. It turns out that the second contour around the crack tip would be an ideal choice for the calculation, as shown in Figure 3.9.

3.3 Time dependent cracking in SiN_x thin film in long time period

In section 3.2, we mainly focused on the short term behavior of the crack in SiN_x thin film sitting on PET substrate. However, the influence of substrate cracking on the long-term time-dependent subcritical cracking has not been studied. In this work, we further investigate the time-dependent environmentally assisted cracking in PECVD SiNx barrier films by testing over extended periods of time (i.e. days versus minutes in contrast to our previous study). Our experimental and numerical results help elucidate the effects of substrate cracking on the driving force (and therefore velocity) of channel cracks in PECVD SiNx barrier layers, which is key to predicting long term damage growth in barrier films under deformation. Specifically, our results highlight various scenarios of increasing, decreasing, or constant crack velocities depending on the substrate cracking configuration and distance to surrounding cracks (i.e. crack density). Details of the experiments and results are described in the following sections.

To test the cracking behavior under extended deformation, PET and PI samples coated with 250 nm of PECVD SiN_x were tested under tensile deformation and held at fixed strains. Crack growth rates were measured by in-situ optical microscopy. Figures 1(c) and (d) show SEM images of focused ion beam (FIB) cross sections of SiN_x on PET that were tested at an applied strain of 0.75% for 0.5 h and at 0.6% for 5 days, respectively. The critical onset strain for these films was found to be 0.95% ± 0.2%, and subcritical crack growth was observed for these specimens. The SEM images show no PET substrate cracking for the specimen held at 0.75% for 0.5 h (Figure 3.11(c.1) and (c.2)). This is consistent with the analysis in our previous study which occurred in a regime without substrate cracking. This is also consistent with constant rates of crack growth in SiN_x film measured during short times (~0.5h) after channel cracking was first observed. In contrast, as clearly shown in Figure 3.11 (d.1-2), FIB cross section images of the SiN_x / PET specimen exposed to atmospheric condition for 5 days revealed cracking into the PET substrate directly under the SiN_x channel crack. The depth of substrate cracking from the interface with SiN_x coating was about 8 μm or 32 times the film thickness. SEM images of a SiN_x/PI specimen held for 2 days at 0.75% reveal very little damage in the substrate, while a SiN_x/PET specimen tested under the same conditions reveal again significant substrate cracking. As will be shown in a later section, the crack growth rates for SiN_x on PI are fairly constant, unlike PET for which significant changes in crack velocities are observed over periods of days. It is therefore likely that the substrate damage is responsible for the observed changes in crack velocities, presumably via changing the driving force for crack extension (which influences crack growth rate based on Figure 3.11(b)). Finite element models were used to quantify the effect of substrate cracking on the driving force for crack extension, *G*, for appropriate crack geometries, in order to explain the various observed behaviors.

First, we studied the change in crack growth rate for an isolated propagating crack with substrate damage. Finite element modeling result shows that the change of driving force of crack growth is less than 1% if the crack spacing is greater than 135 µm (Figure 3.12c). Consequently, we analyzed the behavior of single cracks by ensuring a crack spacing of at least 135 µm (Figure 3.12a). This condition could only be obtained at low

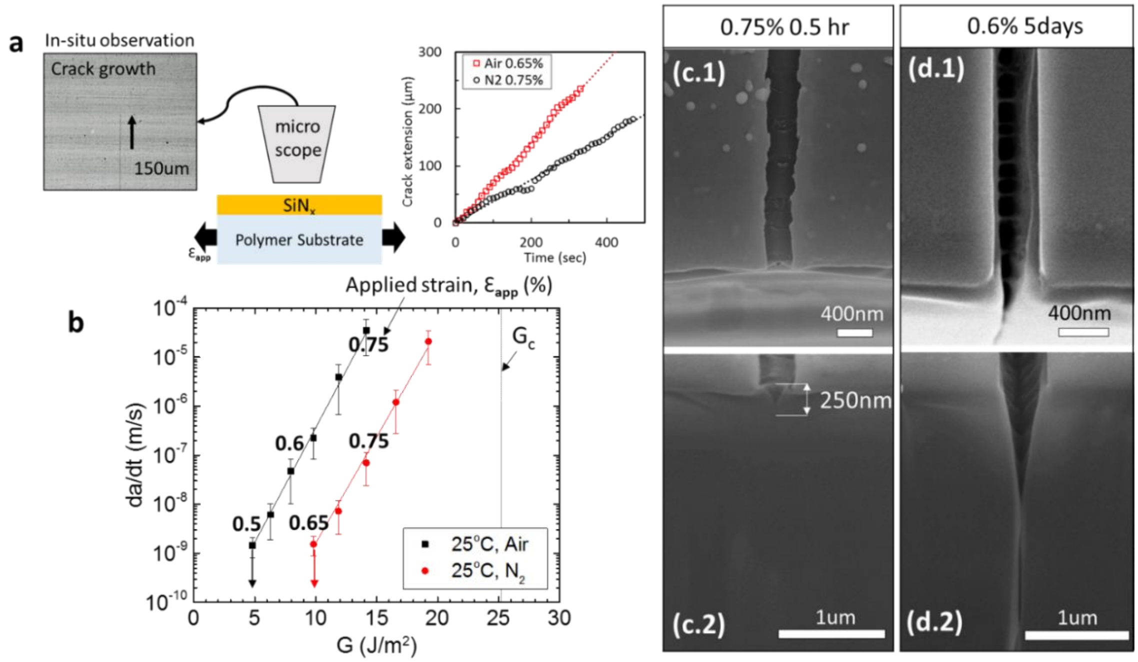

Figure 3.11. (a) Schematic illustration of in-situ microscopy of a SiN_x /PET sample kept at different applied strains, for optical imaging and measurement of channel crack growth and crack extension as a function of time. (b) Measured crack growth rate as a function of driving force G for a channel crack in a 250nm-thick SiN_x film in air and nitrogen, respectively. (c - d) SEM images of SiN_x / PET cross section (cut by FIB) showing the channel crack in the film as well as the substrate crack beneath the channel crack, under (c.1-2) applied strain 0.75% for half an hour and (d.1-2) applied strain 0.6% for 5 days.

applied strains since the crack density quickly increased at higher strains and introduced strong crack interaction effects. We applied the external-load-assisted channel crack growth technique [160] to accomplish this. Specifically, cracks were initiated quickly by pulling the sample to a strain of 0.75%, followed by a quick strain reduction in order to prevent large crack densities from forming and to find isolated non-interacting cracks. Based on modeling results (Figure 3.12b), the development of substrate cracking in the presence of an isolated crack is expected to increase the driving force due to loss of mechanical constraint to crack opening displacement, and therefore the crack growth rate increases (based on Figure 3.11b). Thus, an accelerating isolated crack should give

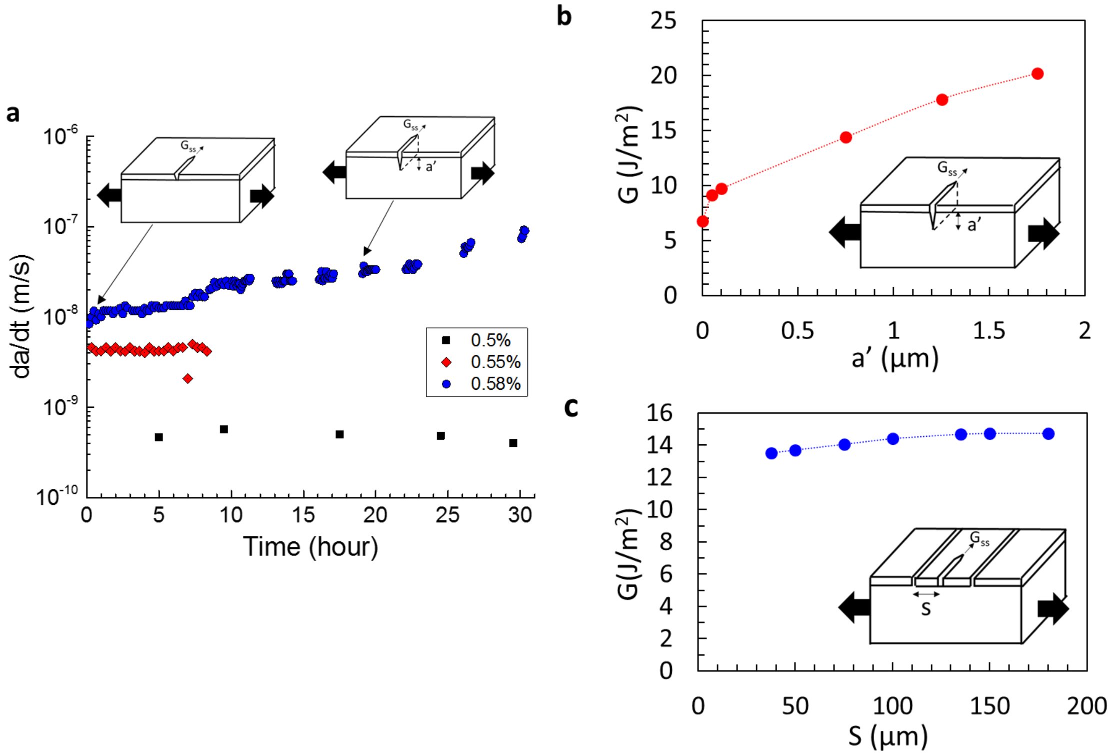

Figure 3.12. (a) Measured crack growth rate in SiN_x / PET at the applied strains of 0.55% and 0.58% in air. (b) Calculated driving force of an isolated crack as a function of substrate cracking depth a', when the applied strain is 0.58%. (c) Calculated driving force of a crack with spacing S to the neighboring long crack on its either side, when the applied strain is 0.75%.

evidence of cracking in the underlying substrate whereas steady state isolated cracking would be an indication of no substrate cracking. For low applied strains of 0.5% and 0.55%, the growth rates were measured to be constant throughout the long testing periods as shown in Figure. 3.12a, an indication that no substrate cracking developed. However, at ε_{app} = 0.58%, the growth rate increased from 8.3 nm/s to 100 nm/s over a period of 30 hours (see Fig. 2a), which is an indication of substrate damage. The corresponding increase in crack driving force is estimated to be 33.7% (from 7.03 to 9.40 J/m^2) from its characterized relationship with subcritical crack growth rates (Figure 3.11b). Based on Figure 3.12b (showing modeling results for $\varepsilon_{\text{applied}} = 0.58\%$), substrate cracking between 50 to 100 nm would be required to induce that increase in driving force. This amount of substrate damage in 30 hours is reasonable, given that no damage was observed for 0.5 and 0.55%, and that substrate cracking was observed at 0.6% for 5 days (see Fig. 3.11d.2).

Figure 3.13d shows the results of crack growth rate behavior over periods of time greater than 0.5h for which substrate damage is expected to play a role. For samples held at strains of $\varepsilon_{\text{app}} = 0.75\%$, 0.6%, 0.55% and 0.5%, the initial crack growth rates were 15010 ± 8560 nm/s, 159 ± 68 nm/s, 14.1 ± 7.5 nm/s and 1.6 ± 0.35 nm/s, respectively. For the larger rates, the cracks grow and quickly reach the edges of the specimen (width: 5 mm), thus the growth rates of different cracks are measured over 100 hours, especially at 0.75% and 0.6%. These rates decreased over the first ~30-40 h until they reached steady-state values of 50.0 ± 13.9 nm/s, 15.5 ± 5.93 nm/s, 3.74 ± 1.86 nm/s and 1.163 ± 0.394 nm/s, respectively. In the case of applied strain of 0.5%, the growth rate is fairly constant. The initial crack growth rates at each applied strain are in the range of the subcritical crack growth rates in v-G curve (i.e., crack velocity, v, versus the strain energy release rate, G) of SiN_x thin films as shown in our previous studies, measured for the first half an hour (Figure 3.11b). [160, 161] Average crack spacing is plotted as a function of time in Figure 3.13e, for tests performed at 0.6 and 0.75%. Along with the evidence of substrate cracking for these extended periods of testing (see Figure 3.11d), these data strongly suggest that the observed decreases in crack growth rates are related to increased crack interactions (smaller spacings between cracks for cracks that nucleate and grow in the later stages of the experiments, as more cracks have already propagated through the specimens' width). In addition, substrate damage keeps developing in channel cracks that have already propagated through the specimen’s width, hence varying amount of substrate damage can be present in neighboring cracks.

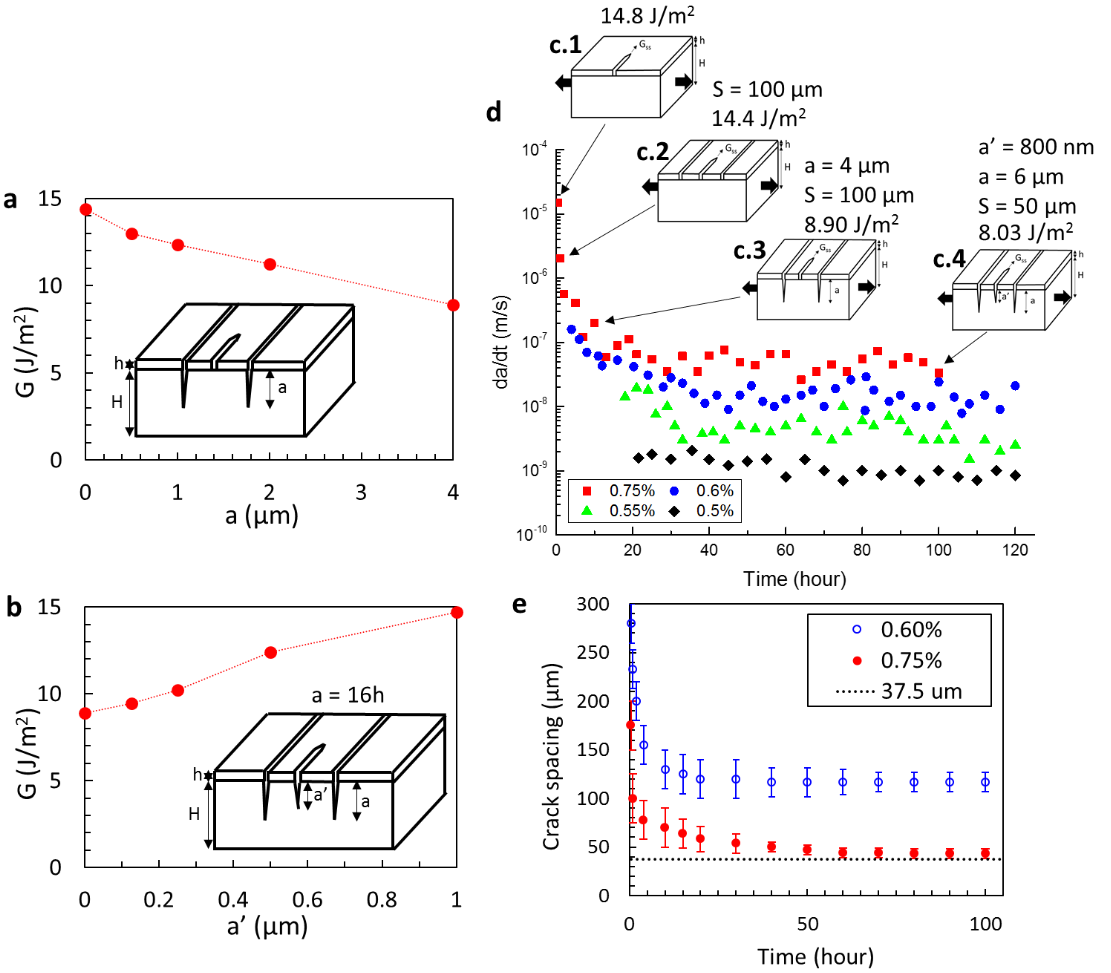

Figure 3.13. (a) Calculated driving force of a crack as a function of substrate cracking depth of neighboring cracks. (b) Calculated driving force of a crack as a function of substrate cracking depth a' in the presence of neighboring cracks with a fixed substrate cracking depth a. Both (a) and (b) were calculated under the applied strain 0.75%, residual strain -0.15%, crack spacing 100µm. (c) Schematics of different cracking modes in the SiN_x film and PET substrate, marked with the associated crack driving force, see text for details; crack spacing S, substrate cracking depth in neighboring cracks a, and in growing crack a’ are chosen for each case. (d) Measured time dependent crack growth rate of SiN_x / PET in air, while the applied strain was kept at 0.5, 0.55, 0.6, 0.75%, respectively. For the applied strain 0.6%, the last data point at 120 hours corresponds to the sample in Fig. 3.11d. (e) Crack spacing as a function of time at the applied strain of 0.75% and 0.6%, respectively.

Finite element analysis was conducted to provide further insight into the effects of substrate cracking on systems of interacting cracks. For this analysis, a strain of 0.75% was applied to the model where a single propagating crack is interacting with two adjacent cracks. The spacing of the cracks in the model was chosen to be either 50 or 100 μm, depending of the observed crack spacings (Figure 3.13e). Film and substrate thicknesses were 250 nm and 125 μm, respectively. To further explore the parametric space, additional calculations were done on a number of crack configurations (single versus multiple cracks, with and without substrate cracking) to elucidate their impact on crack driving forces (Figure 3.13a and 3.13b). Results show that substrate cracking in the two adjacent cracks reduces the driving force in the growing crack, as the depth into the substrate increases. The driving force decreases by 40% with the increase of substrate cracking depth in the neighboring crack up to 4 μm (Figure 3.13a). This is due to the loss of in mechanical constraint in the neighboring cracks as the substrate crack grows in the PET. This has the equivalent effect of closing the growing crack and reducing the energy dissipated for channel crack growth. Figure 3b shows the effect of substrate cracking on the growing crack when the neighboring cracks also induce substrate cracking. When substrate cracking under the growing crack was introduced (up to 1 μm in depth), the crack driving force increased up to 65% while substrate cracking depth in the neighboring cracks was kept at 4 μm (Figure 3.13b). The increase in driving force with substrate damage under the growing crack is consistent with the results in the previous section as shown in Figure 3.12b.

Based on the modeling results (Figure 3.12c and Figure 3.13a-b) and the measured evolution of crack spacing with time (Figure 3.13e), a possible scenario for the observed evolution of crack propagation rates can be presented as illustrated in Figure 3.13c, with four cases for samples held at 0.75%. The crack driving force value G was extracted from modeling and the corresponding growth rate was calculated from the *v-G* curve in Fig. 1b. Initially single channel cracks in SiN_x develop, and the modeling result predicts a driving force of 14.8 J/m^2 (Figure 3.13c1), corresponding to a crack growth rate of ~75μm/s based on Figure 3.11b. The growth rates for the first 30 mins are on the same order of magnitude, i.e. 15 ± 8.6 μm/s (Figure 3.13d). It should be noted that the cracks traverse the full width of the specimen in less than a few minutes, for example, 1 min for 75μm/s and 5 mins for 15μm/s, therefore the rates measured after ~0.5 h are for multiple interacting cracks. So the second case investigated in the scenario after an hour is channel crack growth with reduced crack spacing as depicted in Figure 3.13.c2. By adding two adjacent interacting channel cracks (crack spacing 100 μm), the driving force was reduced to 14.4 J/m^2, corresponding to a slight decrease in crack growth rates (~50 μm/s based on Figure 3.11b). Up to this part, substrate cracking is not taken into consideration as evident in the SEM image in Fig. 5b (free from the substrate damage in the PET substrate after an hour at strain 0.75%). However, over time, substrate damage develops first in the existing cracks, and the new growing cracks have a lower driving force due to the effect of substrate damage in the neighboring cracks as explained in Figure 3.13a, corresponding to the third case in Figure 3.13c.3. For example, the crack driving force was further reduced to 8.9 J/m^2 when a 4 μm crack was present in the PET under the neighboring cracks (Figure 3c.3, crack spacing 100 μm). This corresponds to a crack growth rate of ~119 nm/s (see Figure 3.11b) and is commensurate with the measured rate after 10 hours (see Figure 3.13d). At longer times, the cracks were observed to grow much more slowly (~50-100 nm/s), and it took more than 20 hours for cracks to traverse the specimen's width. Hence the growing cracks whose rates are measured for more than 30 h also undergo substrate cracking (Figure 3.13c.4). With 800 nm substrate cracking underneath the growing crack and 6 µm neighboring penetration into PET, the driving force is calculated to be 8.03 J/m^2. This last case of the scenario occurs when a steady-state growth rate is observed as shown in Figure 3.13d after ~30-40 h. This is the result of a balance between additional substrate cracking in the growing crack, i.e. increase of driving force (Figure 3.13a), and in the adjacent cracks, i.e. decrease of driving force (Figure 3.13b).

The effect of environment on the long-term crack growth rate behavior was also studied by performing experiments in dry nitrogen for long periods of time before switching to laboratory air. Figure 3.14 shows that crack growth rate evolution for a specimen tested in air at $\varepsilon_{app} = 0.75\%$ along with the evolution for two specimens tested at the same applied strain in dry nitrogen before switching to laboratory air after either 20 or 60 h. In dry nitrogen, the initial crack growth rate is two orders of magnitude lower than in the humid environment, which is consistent with Figure 3.11b, highlighting environmentally-assisted cracking. A decrease in rate is also observed in dry nitrogen, with a steady-state value reached after ~20 hours, but the magnitude of the decrease is much less than in air. This behavior is attributed to the fact that the density of cracks in N_2 is two orders of magnitude lower than in air (a few cracks in N_2 vs. hundreds of cracks in air), and therefore the effect of the interacting cracks (and their associated substrate damage) is much reduced compared to what was described in the previous section. After switching from N_2 to humid air after 20 and 60 h (for the two specimens shown in Figure 4), a large increase in the crack growth rate was observed (due to the impact of environmentally-assisted cracking), rising in both cases to rates similar to the initial rates for samples tested in humid air. The newly formed cracks after introducing air behave like a “fresh” specimen tested in air because of the very low density of cracks that formed in nitrogen. The ensuing decrease in crack growth rate is also very similar to that observed in specimens tested in air, suggesting a similar sequence of events described in the previous sections (see Figure 3.13c). Lastly, Figure 3.14 shows that the steady state rates in nitrogen are only one order of magnitude lower than that in air (while the initial rates were two orders of magnitude lower). The lower relative decrease in nitrogen may be simply due to the lower density of cracks in that environment (leading to lower decreases in driving force), although it is also possible that the humid environment induces more substrate damage that could lead to

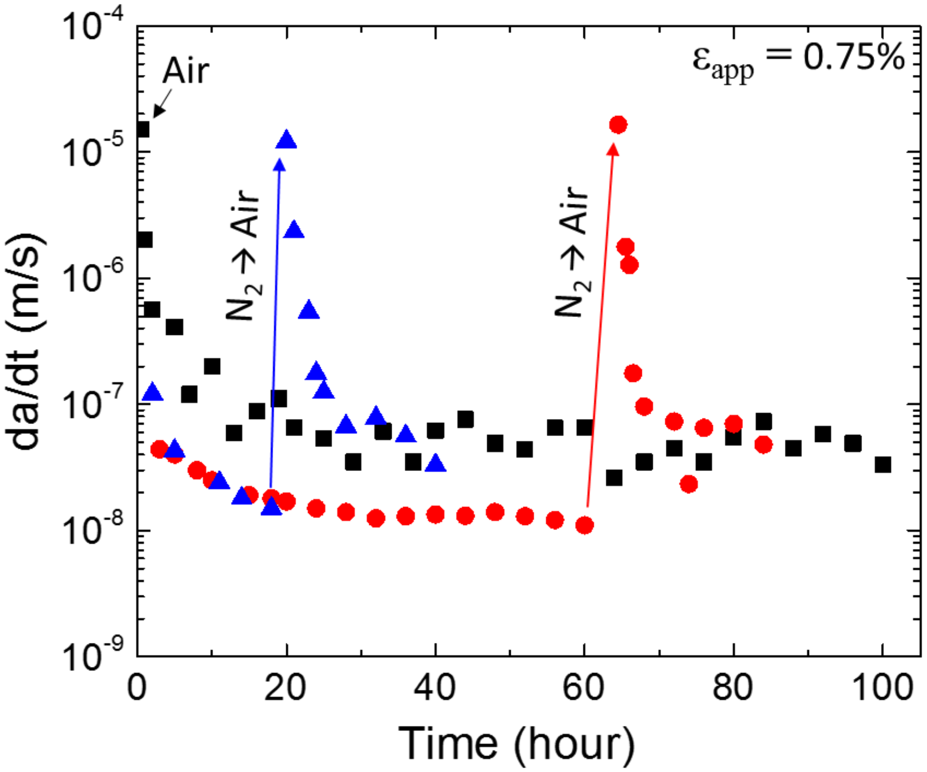

Figure 3.14. Crack growth rate behavior of SiN_x / PET at the applied strain of 0.75% subjected to change of environmental condition.

larger relative decreases in air.

Compared to PET, PI has a higher tensile strength (PI: 340 MPa, PET: 170 MPa by ASTM D882) and resistance to hydrolysis and thus should have greater resistance to substrate damage. Hence, the long-term evolution of crack growth rates in SiN_x on PI should be markedly different from that measured with PET, under same initial channel crack driving force, *G*. In order to test a SiN_x specimen on PI with the same initial G value, the Z parameter from Equation 3.4 was evaluated for PI. The moduli of elasticity of SiN_x and polymer substrates were determined by nanoindentation and uniaxial tensile testing, respectively. [160, 161] The modulus of PI was found to be 7.6 ± 0.17 GPa, higher than PET which has found to be 4.07 ± 0.12 GPa. The elastic mismatch between SiN_x and PI was $\alpha = 0.880$ and between SiN_x and PET was $\alpha = 0.934$, and the corresponding dimensionless energy release rates are $Z = 8.62$ and $Z = 11.8$, respectively. [162] Based on these values, a higher applied strain 0.1% was required for PI samples, i.e. 0.85%, to match the crack driving forces between PI (13.8 J/m^2) and PET (14.4 J/m^2 for PET at 0.75%). Hence for these two experiments, there is less than 5% difference in the initial driving force. In calculating *G* with Equation 3.3, the residual strain is also required. For residual compressive strains (as for PECVD SiN_x films), this can be quantified by first straining (in our case up to 0.8%, subcritical value of crack onset strain) a specimen to form a few channel cracks and then catching the applied strain while unloading at which the cracks start closing and become invisible. [161] Residual strains were found to be -0.15% for both PI and PET. As shown in Figure 3.15a, the decrease in crack growth rate with time for SiN_x

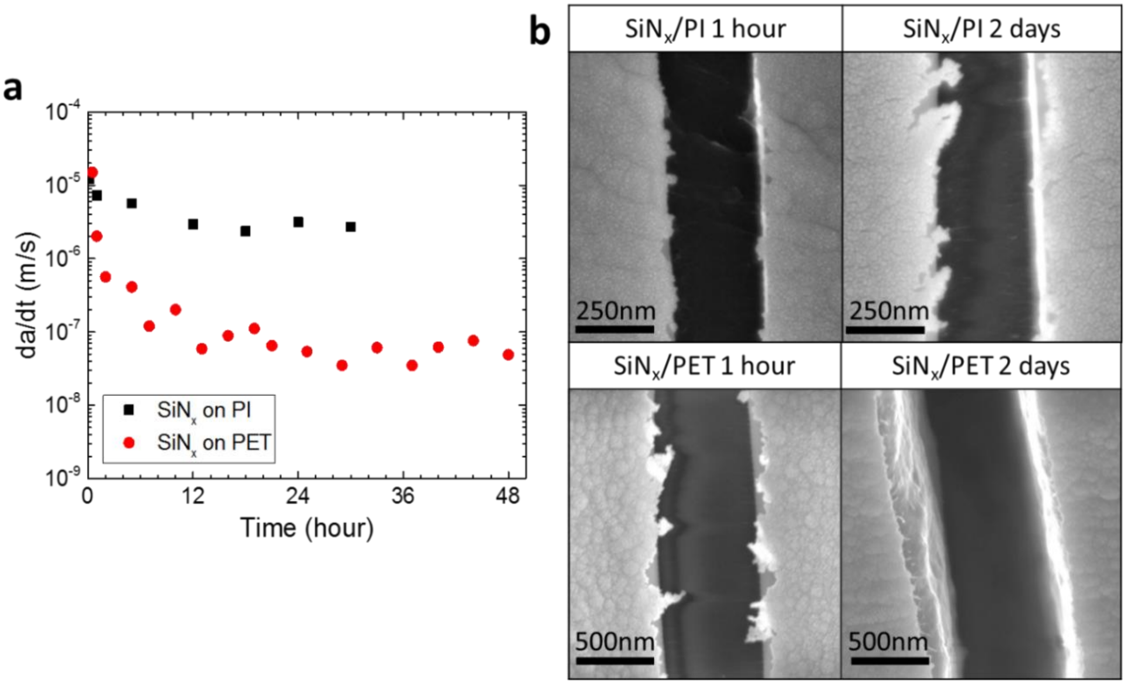

Figure 3.15. (a) Time-dependent crack growth rate behavior of SiN_x deposited on PET at the applied strain 0.75% versus on PI at the applied strain0.85%. (b) SEM images of SiN_x / PET and SiN_x / PI after 1 hour and 2 days passed, respectively.

/ PI was much less than that of SiN_x / PET. In SEM images, substrate cracking was not detected in both of PI and PET after one hour. However, after 2 days, crack penetration was observed in the PET as expected, whereas PI was still free from substrate cracking. A little decrease in crack growth rate of SiN_x / PI presumably came from inherent damage on the top surface of the substrate. It is important to note that, when both of the substrates are under the same value of applied strain, the number of cracks in SiN_x / PI was greatly decreased when compared to SiN_x / PET. For example, at the center of specimen after 2 days of testing, 255 ± 32 cracks were accumulated in SiN_x / PET while 21 ± 5 cracks were accumulated in SiN_x / PI. This certainly demonstrates that depositing barriers on substrates with high tensile strength and resistance to hydrolysis and substrate damage is one effective means of improving the reliability of barrier films under long-term mechanical loading.

In conclusion, in this work, we focused on the long-term behavior of environmentally-assisted subcritical cracking of PECVD SiN_x barrier films on polyethylene terephthalate (PET) and polyimide (PI) substrates. We measured the crack growth rates as a function of time under different applied strains using in-situ optical microscopy. The present experiments over longer periods reveal a regime where cracking also develops in the polymer substrate. Our combined in-situ microscopy and finite-element modeling results highlight the combined effects of neighboring cracks and substrate cracking on the crack growth rate evolution in the film. In most cases, the subcritical crack growth rates decrease over time by up to two orders of magnitude until steady-state rates are reached. However, increases in growth rate with time can occur in certain conditions, such as isolated cracks with increasing substrate damage. For SiN_x on PI, crack growth rates were found to be more stable over time due to the lack of crack growth in the substrate as compared to SiN_x on PET. These results provide a guideline to effectively improving the long-term reliability of flexible barrier layers through the use of a substrate possessing high strength and resistance to hydrolysis which limits substrate damage and thus reduces crack growth rates.

Numerical model and simulation method. PET was modeled as an elastic-viscoplastic material, while SiN_x a purely elastic material. For PET, the elastic strain rate $\dot{\varepsilon}_{\mathrm{e}}$ is linearly proportional to the stress rate $\dot{\sigma}$ as $\dot{\varepsilon}_{\mathrm{e}} = \dot{\sigma}/E_s$ where E_s is the elastic modulus; a Cowper-Symonds overstress power law was applied to calculate the plastic strain rate.

$$\dot{\varepsilon}_{\mathrm{p}} = D\left(\frac{\sigma}{\sigma_{\mathrm{Y}}(\varepsilon_{\mathrm{p}})} - 1\right)^{n'} \tag{3}$$

where *D* and *n*' are the material constants, $\sigma_{\mathrm{Y}}(\varepsilon_{\mathrm{p}})$ is the yield stress that depends on the total yield strain ε_{p}. These material properties are summarized in Table 1. Since no debonding was observed during experiments under subcritical loading, perfect bonding was assumed between the SiN_x thin film and PET substrate. Due to the large elastic mismatch between SiN_x thin film and PET substrate, large stress gradients may develop in PET parts underneath the cracks. To capture such large stress gradients in the PET substrate, a dense mesh scheme was employed for PET underneath the cracks, as shown in Figure 3.16. The growing crack in the PET substrate was modeled as an opening wedge. Penetration depth of the crack in the PET substrate can markedly affect the driving force of crack extension in the SiN_x thin film, due to a loss of substrate constraints. All the numerical simulations were performed using ABAQUS 6.13. [163]

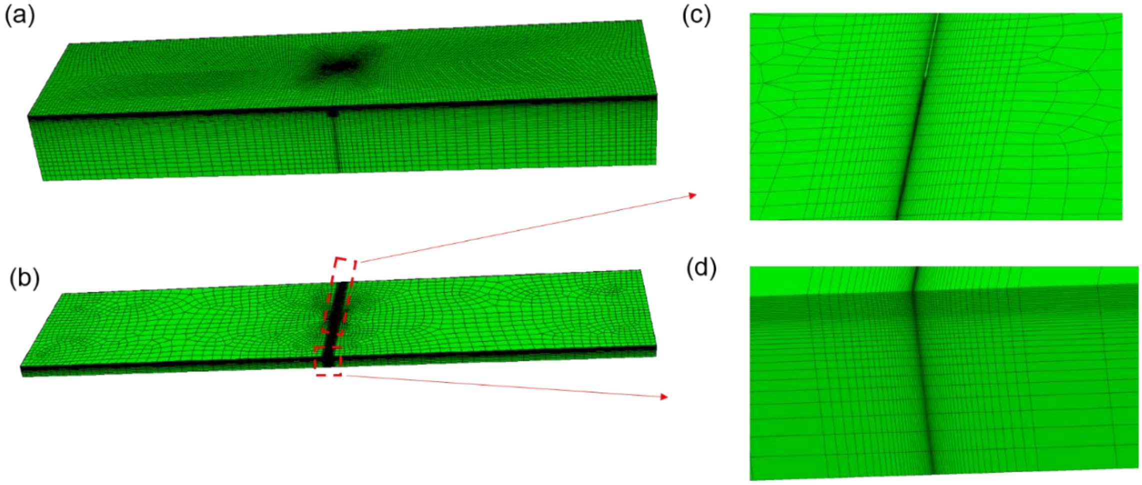

Figure 3.16 A general mesh schema used in calculating the driving force with finite element analysis. (a) A whole view of a meshed model, which is used to calculate the crack driving force of SiN_x thin film when neighboring substrate cracks are present. (b) A view of meshed middle layer of PET substrate which has thickness of substrate penetration depth. (c) A magnified view of the mesh on the top surface of (b). (d) A magnified view of the mesh in the side surface of (b).

CHAPTER 4. CONCLUSIONS AND FUTURE RESEARCH

4.1 Contributions

In this thesis, we mainly reveal the degradation mechanisms of advanced lithium ion battery electrode and barrier layers in flexible electronics through the integration of predictive modeling and experiments. The main contributions are summarized as below.

4.1.1 Contributions to the understanding of Si anode lithiation in lithium ion batteries

Based on the observations from in situ experiments and theoretical model in previous studies, a two phase model integrated with single phase model is developed to account for the lithiation process in Si anode, which can be anisotropic, two stage or stress dependent. Integrated with in-situ TEMs, this chemomechanical model shed lights on the understanding of the coating behaviors during lithiation/delithiation cycles and its effects on the performance of Si based anode, namely, Si nanowire, Si nanotube, Ge/Si/Cu nanowire and Si nanoparticles. The main results provide a guidance to design an applicable Si based anodes with coatings to deliver durable energies. Also the results help to gain unprecedented mechanistic insights into electrochemically-driven structural evolution process in the electrodes. In general, our modeling approach integrated with experiments can be applied to the mechanical characterization of a wide range of electrochemically driven devices for energy storage and conversions.

4.1.2 Contributions to revealing the mechanism behind the environmentally assisted thin film crack sitting on polymer substrates

The subcritical onset strain for barrier layers are found to be time dependent through the observation and measurements form experiments. To reveal the time dependent behaviors, an elastic-viscoplastic model has been developed and implemented to account for the time dependent stress relaxation and yielding of the polymer substrate under tensile loading. Besides, different cracking modes of the thin film has been proposed to account for the thin film crack interactions and substrate cracking, which are found to impact on the time dependent behavior of thin film crack propagation. The main results from this work elaborates on the mechanisms behind the time dependent behavior of thin film cracking and shapes the old view of subcritical onset strain being time independent. Furthermore, this work provides guidance to the design of a more reliable barrier layer which can resist time-dependent and environmental assisted cracking.

4.2 Future research

It has been shown previously that SiO_x coating has been an effective way to alleviate the degradation of Si based anode during the process of lithiation/delithiation, the detailed mechanical and chemical properties of lithiated SiO_x and its compositions remains a mystery. In addition, the current SiO_x coating has a low charge/discharge rate; and both SiO_x and its corresponding lithiated part are brittle according to current limited observations. Therefore, a cheap, more compliant and more conductive coating may be desired for better development of Si based anode in lithium ion batteries. In the two phase model, although we have accounted for the pressure dependence of lithium conductivity in Si, it is reported that stress gradient may also affect the conductivity, which may result in a more accurate lithiation model.

As for the cathode side of lithium ion batteries, the mechanisms behind the mixture of different sizes of cathode materials need to be further studied by integrating the continuum model developed by Newman and his coworkers with the electrochemical measurements from the experiments.

Lastly but not least, the environmental effect on the time dependent behavior of thin film cracking needs further study. Specifically, we have almost determined that it is the attack from the water molecules in the air that contributes to the reduction of crack driving force in the thin film, Therefore, atomic simulations may need to be carried out to simulate the chemical reaction process, which is coupled with mechanical behaviors. Besides, more other substrates can be investigated to improving the reliability of barrier films.

REFERENCES

1. Tarascon, J. M.; Armand, M., Issues and challenges facing rechargeable lithium batteries. *Nature* **2001,** *414* (6861), 359-367.

2. Goriparti, S.; Miele, E.; De Angelis, F.; Di Fabrizio, E.; Proietti Zaccaria, R.; Capiglia, C., Review on recent progress of nanostructured anode materials for Li-ion batteries. *Journal of Power Sources* **2014,** *257*, 421-443.

3. McDowell, M. T.; Lee, S. W.; Nix, W. D.; Cui, Y., 25th Anniversary Article: Understanding the Lithiation of Silicon and Other Alloying Anodes for Lithium-Ion Batteries. *Advanced Materials* **2013,** *25* (36), 4966-4985.

4. Liu, X. H.; Zheng, H.; Zhong, L.; Huang, S.; Karki, K.; Zhang, L. Q.; Liu, Y.; Kushima, A.; Liang, W. T.; Wang, J. W.; Cho, J.-H.; Epstein, E.; Dayeh, S. A.; Picraux, S. T.; Zhu, T.; Li, J.; Sullivan, J. P.; Cumings, J.; Wang, C.; Mao, S. X.; Ye, Z. Z.; Zhang, S.; Huang, J. Y., Anisotropic Swelling and Fracture of Silicon Nanowires during Lithiation. *Nano Letters* **2011,** *11* (8), 3312-3318.

5. Xu, J.; Dou, S.; Liu, H.; Dai, L., Cathode materials for next generation lithium ion batteries. *Nano Energy* **2013,** *2* (4), 439-442.

6. Nitta, N.; Wu, F.; Lee, J. T.; Yushin, G., Li-ion battery materials: present and future. *Materials Today* **2015,** *18* (5), 252-264.

7. Albertus, P.; Christensen, J.; Newman, J., Experiments on and Modeling of Positive Electrodes with Multiple Active Materials for Lithium-Ion Batteries. *Journal of The Electrochemical Society* **2009,** *156* (7), A606-A618.

8. Chung, D.-W.; Shearing, P. R.; Brandon, N. P.; Harris, S. J.; García, R. E., Particle Size Polydispersity in Li-Ion Batteries. *Journal of The Electrochemical Society* **2014,** *161* (3), A422-A430.

9. Darling, R.; Newman, J., Modeling a Porous Intercalation Electrode with Two Characteristic Particle Sizes. *Journal of The Electrochemical Society* **1997,** *144* (12), 4201-4208.

10. Liu, H.; Strobridge, F. C.; Borkiewicz, O. J.; Wiaderek, K. M.; Chapman, K. W.; Chupas, P. J.; Grey, C. P., Capturing metastable structures during high-rate cycling of LiFePO<sub>4</sub> nanoparticle electrodes. *Science* **2014,** *344* (6191).

11. Lueth, S.; Sauter, U. S.; Bessler, W. G., An Agglomerate Model of Lithium-Ion Battery Cathodes. *Journal of The Electrochemical Society* **2016,** *163* (2), A210-A222.

12. Mao, Z.; Farkhondeh, M.; Pritzker, M.; Fowler, M.; Chen, Z., Multi-Particle Model for a Commercial Blended Lithium-Ion Electrode. *Journal of The Electrochemical Society* **2016,** *163* (3), A458-A469.

13. Mao, Z.; Farkhondeh, M.; Pritzker, M.; Fowler, M.; Chen, Z.; Safari, M., Model-Based Prediction of Composition of an Unknown Blended Lithium-Ion Battery Cathode. *Journal of The Electrochemical Society* **2015,** *162* (4), A716-A721.

14. Zhang, G.; Shaffer, C. E.; Wang, C.-Y.; Rahn, C. D., Effects of Non-Uniform Current Distribution on Energy Density of Li-Ion Cells. *Journal of The Electrochemical Society* **2013,** *160* (11), A2299-A2305.

15. Zhang, G.; Cao, L.; Ge, S.; Wang, C.-Y.; Shaffer, C. E.; Rahn, C. D., In Situ Measurement of Radial Temperature Distributions in Cylindrical Li-Ion Cells. *Journal of The Electrochemical Society* **2014,** *161* (10), A1499-A1507.

16. Li, H.; Huang, X. J.; Chen, L. Q.; Wu, Z. G.; Liang, Y., A high capacity nano-Si composite anode material for lithium rechargeable batteries. *Electrochemical and Solid State Letters* **1999,** *2* (11), 547-549.

17. Chan, C. K.; Peng, H. L.; Liu, G.; McIlwrath, K.; Zhang, X. F.; Huggins, R. A.; Cui, Y., High-performance lithium battery anodes using silicon nanowires. *Nature Nanotechnology* **2008,** *3* (1), 31-35.

18. Magasinski, A.; Dixon, P.; Hertzberg, B.; Kvit, A.; Ayala, J.; Yushin, G., High-performance lithium-ion anodes using a hierarchical bottom-up approach. *Nature Materials* **2010,** *9* (4), 353-358.

19. Liu, X. H.; Wang, J. W.; Huang, S.; Fan, F.; Huang, X.; Liu, Y.; Krylyuk, S.; Yoo, J.; Dayeh, S. A.; Davydov, A. V.; Mao, S. X.; Picraux, S. T.; Zhang, S.; Li, J.; Zhu, T.; Huang, J. Y., In situ atomic-scale imaging of electrochemical lithiation in silicon. *Nat. Nanotechnol.* **2012,** *7* (11), 749-756.

20. Ko, M.; Oh, P.; Chae, S.; Cho, W.; Cho, J., Considering critical factors of Li-rich cathode and Si anode materials for practical Li-ion cell applications. *Small* **2015,** *11* (33), 4058-4073.

21. Obrovac, M. N.; Chevrier, V. L., Alloy negative electrodes for Li-ion batteries. *Chemical Reviews* **2014,** *114* (23), 11444-11502.

22. Beaulieu, L. Y.; Eberman, K. W.; Turner, R. L.; Krause, L. J.; Dahn, J. R., Colossal reversible volume changes in lithium alloys. *Electrochemical and Solid State Letters* **2001,** *4* (9), A137-A140.

23. Liu, X. H.; Zhong, L.; Huang, S.; Mao, S. X.; Zhu, T.; Huang, J. Y., Size-Dependent Fracture of Silicon Nanoparticles During Lithiation. *Acs Nano* **2012,** *6* (2), 1522-1531.

24. Wang, X.; Fan, F.; Wang, J.; Wang, H.; Tao, S.; Yang, A.; Liu, Y.; Chew, H. B.; Mao, S. X.; Zhu, T.; Xia, S., High damage tolerance of electrochemically lithiated silicon. *Nature Communications* **2015,** *6*, 8417.

25. Xiao, X.; Liu, P.; Verbrugge, M. W.; Haftbaradaran, H.; Gao, H., Improved cycling stability of silicon thin film electrodes through patterning for high energy density lithium batteries. *Journal of Power Sources* **2011,** *196* (3), 1409-1416.
26. McDowell, M. T.; Lee, S. W.; Harris, J. T.; Korgel, B. A.; Wang, C.; Nix, W. D.; Cui, Y., In Situ TEM of Two-Phase Lithiation of Amorphous Silicon Nanospheres. *Nano Letters* **2013,** *13* (2), 758-764.

27. Lee, S. W.; McDowell, M. T.; Berla, L. A.; Nix, W. D.; Cui, Y., Fracture of crystalline silicon nanopillars during electrochemical lithium insertion. *Proceedings of the National Academy of Sciences of the United States of America* **2012,** *109* (11), 4080-4085.

28. Yao, Y.; McDowell, M. T.; Ryu, I.; Wu, H.; Liu, N. A.; Hu, L. B.; Nix, W. D.; Cui, Y., Interconnected silicon hollow nanospheres for lithium-ion battery anodes with long cycle life. *Nano Letters* **2011,** *11* (7), 2949-2954.

29. Wu, H.; Chan, G.; Choi, J. W.; Ryu, I.; Yao, Y.; McDowell, M. T.; Lee, S. W.; Jackson, A.; Yang, Y.; Hu, L. B.; Cui, Y., Stable cycling of double-walled silicon nanotube battery anodes through solid-electrolyte interphase control. *Nature Nanotechnology* **2012,** *7* (5), 310-315.

30. Xia, F.; Kim, S. B.; Cheng, H. Y.; Lee, J. M.; Song, T.; Huang, Y. G.; Rogers, J. A.; Paik, U.; Il Park, W., Facile synthesis of free-standing silicon membranes with three-dimensional nanoarchitecture for anodes of lithium ion batteries. *Nano Letters* **2013,** *13* (7), 3340-3346.

31. Hertzberg, B.; Alexeev, A.; Yushin, G., Deformations in Si-Li anodes upon electrochemical alloying in nano-confined space. *Journal of the American Chemical Society* **2010,** *132* (25), 8548-8549.

32. Lee, W. J.; Hwang, T. H.; Hwang, J. O.; Kim, H. W.; Lim, J.; Jeong, H. Y.; Shim, J.; Han, T. H.; Kim, J. Y.; Choi, J. W.; Kim, S. O., N-doped graphitic self-encapsulation for high performance silicon anodes in lithium-ion batteries. *Energy & Environmental Science* **2014,** *7* (2), 621-626.

33. Liu, J. Y.; Li, N.; Goodman, M. D.; Zhang, H. G.; Epstein, E. S.; Huang, B.; Pan, Z.; Kim, J.; Choi, J. H.; Huang, X. J.; Liu, J. H.; Hsia, K. J.; Dillon, S. J.; Braun, P. V., Mechanically and chemically robust sandwich-structured C@Si@C nanotube array Li-ion battery anodes. *ACS Nano* **2015,** *9* (2), 1985-1994.

34. Son, I. H.; Park, J. H.; Kwon, S.; Park, S.; Rummeli, M. H.; Bachmatiuk, A.; Song, H. J.; Ku, J.; Choi, J. W.; Choi, J. M.; Doo, S. G.; Chang, H., Silicon carbide-free graphene

growth on silicon for lithium-ion battery with high volumetric energy density. *Nature Communications* **2015,** *6*, 7393.

35. Cao, F. F.; Deng, J. W.; Xin, S.; Ji, H. X.; Schmidt, O. G.; Wan, L. J.; Guo, Y. G., Cu-Si nanocable arrays as high-rate anode materials for lithium-ion batteries. *Advanced Materials* **2011,** *23* (38), 4415-4420.

36. Karki, K.; Zhu, Y. J.; Liu, Y. H.; Sun, C. F.; Hu, L. B.; Wang, Y. H.; Wang, C. S.; Cumings, J., Hoop-strong nanotubes for battery electrodes. *Acs Nano* **2013,** *7* (9), 8295-8302.

37. McDowell, M. T.; Lee, S. W.; Ryu, I.; Wu, H.; Nix, W. D.; Choi, J. W.; Cui, Y., Novel size and surface oxide effects in silicon nanowires as lithium battery anodes. *Nano Letters* **2011,** *11* (9), 4018-4025.

38. Sim, S.; Oh, P.; Park, S.; Cho, J., Critical Thickness of SiO2 Coating Layer on Core@Shell Bulk@Nanowire Si Anode Materials for Li-Ion Batteries. *Adv. Mater.* **2013,** *25* (32), 4498-4503.

39. Yu, B. C.; Hwa, Y.; Park, C. M.; Kim, J. H.; Sohn, H. J., Effect of oxide layer thickness to nano-Si anode for Li-ion batteries. *RSC Adv.* **2013,** *3* (24), 9408-9413.

40. Luo, L. L.; Yang, H.; Yan, P. F.; Travis, J. J.; Lee, Y.; Liu, N.; Piper, D. M.; Lee, S. H.; Zhao, P.; George, S. M.; Zhang, J. G.; Cui, Y.; Zhang, S. L.; Ban, C. M.; Wang, C. M., Surface-coating regulated lithiation kinetics and degradation in silicon nanowires for lithium ion battery. *Acs Nano* **2015,** *9* (5), 5559-5566.

41. Wu, H.; Yu, G. H.; Pan, L. J.; Liu, N. A.; McDowell, M. T.; Bao, Z. A.; Cui, Y., Stable Li-ion battery anodes by in-situ polymerization of conducting hydrogel to conformally coat silicon nanoparticles. *Nature Communications* **2013,** *4*, 1943.

42. Wu, H.; Chan, G.; Choi, J. W.; Ryu, I.; Yao, Y.; McDowell, M. T.; Lee, S. W.; Jackson, A.; Yang, Y.; Hu, L.; Cui, Y., Stable cycling of double-walled silicon nanotube battery anodes through solid-electrolyte interphase control. *Nat Nano* **2012,** *7* (5), 310-315.

43. Schmidt, J. P.; Tran, H. Y.; Richter, J.; Ivers-Tiffée, E.; Wohlfahrt-Mehrens, M., Analysis and prediction of the open circuit potential of lithium-ion cells. *Journal of Power Sources* **2013,** *239*, 696-704.

44. Dai, Y.; Cai, L.; White, R. E., Simulation and analysis of stress in a Li-ion battery with a blended LiMn2O4 and LiNi0.8Co0.15Al0.05O2 cathode. *Journal of Power Sources* **2014,** *247*, 365-376.

45. Jung, S.; Jung, H.-Y., Charge/discharge characteristics of Li-ion batteries with two-phase active materials: a comparative study of LiFePO4 and LiCoO2 cells. *International Journal of Energy Research* **2016,** *40* (11), 1541-1555.

46. Qiu, C.; Liu, L.; Du, F.; Yang, X.; Wang, C.; Chen, G.; Wei, Y., Electrochemical performance of LiMn2O4/LiFePO4 blend cathodes for lithium ion batteries. *Chemical Research in Chinese Universities* **2015,** *31* (2), 270-275.

47. Tang, W.; Liu, L. L.; Tian, S.; Li, L.; Yue, Y. B.; Wu, Y. P.; Guan, S. Y.; Zhu, K., Nano-LiCoO2 as cathode material of large capacity and high rate capability for aqueous rechargeable lithium batteries. *Electrochemistry Communications* **2010,** *12* (11), 1524-1526.

48. Zhang, S.; Qiu, X.; He, Z.; Weng, D.; Zhu, W., Nanoparticled Li(Ni1/3Co1/3Mn1/3)O2 as cathode material for high-rate lithium-ion batteries. *Journal of Power Sources* **2006,** *153* (2), 350-353.

49. Lee, K. T.; Kan, W. H.; Nazar, L. F., Proof of Intercrystallite Ionic Transport in LiMPO4 Electrodes (M = Fe, Mn). *Journal of the American Chemical Society* **2009,** *131* (17), 6044-6045.
50. Liu, H.; Strobridge, F. C.; Borkiewicz, O. J.; Wiaderek, K. M.; Chapman, K. W.; Chupas, P. J.; Grey, C. P., Capturing metastable structures during high-rate cycling of LiFePO4 nanoparticle electrodes. *Science* **2014,** *344* (6191).
51. Li, Y.; El Gabaly, F.; Ferguson, T. R.; Smith, R. B.; Bartelt, N. C.; Sugar, J. D.; Fenton, K. R.; Cogswell, D. A.; Kilcoyne, A. L. D.; Tyliszczak, T.; Bazant, M. Z.; Chueh, W. C., Current-induced transition from particle-by-particle to concurrent intercalation in phase-separating battery electrodes. *Nature Materials* **2014,** *13* (12), 1149-1156.

52. Fuller, T. F.; Doyle, M.; Newman, J., Simulation and Optimization of the Dual Lithium Ion Insertion Cell. *Journal of The Electrochemical Society* **1994,** *141* (1), 1-10.

53. Li, F. M.; Unnikrishnan, S.; van de Weijer, P.; van Assche, F.; Shen, J.; Ellis, T.; Manders, W.; Akkerman, H.; Bouten, P.; van Mol, T., 18.3: Flexible Barrier Technology for Enabling Rollable AMOLED Displays and Upscaling Flexible OLED Lighting. *SID Symposium Digest of Technical Papers* **2013,** *44* (1), 199-202.

54. Bulusu, A.; Singh, A.; Wang, C. Y.; Dindar, A.; Fuentes-Hernandez, C.; Kim, H.; Cullen, D.; Kippelen, B.; Graham, S., Engineering the mechanical properties of ultrabarrier films grown by atomic layer deposition for the encapsulation of printed electronics. *J. Appl. Phys.* **2015,** *118* (8).
55. Andringa, A.-M.; Perrotta, A.; De Peuter, K.; Knoops, H. C. M.; Kessels, W. M. M.; Creatore, M., Low-Temperature Plasma-Assisted Atomic Layer Deposition of Silicon Nitride Moisture Permeation Barrier Layers. *ACS Applied Materials and Interfaces* **2015,** *7* (40), 22525-22532.
56. Majee, S.; Geffroy, B.; Bonnassieux, Y.; Bouree, J.-E., Interface effects on the moisture barrier properties of SiNx/PMMA/SiNx hybrid structure. *Surface and Coatings Technology* **2014,** *254*, 429-432.

57. Rochat, G.; Fayet, P., Characterization of Mechanical Properties of Ultra-thin Oxide Coatings on Polymers by Uniaxial Fragmentation Tests. *Journal of Adhesion Science and Technology* **2012,** *26* (20-21), 2381-2392.

58. van Assche, F. J. H.; Unnikrishnan, S.; Michels, J. J.; van Mol, A. M. B.; van de Weijer, P.; van de Sanden, M. C. M.; Creatore, M., On the intrinsic moisture permeation rate of remote microwave plasma-deposited silicon nitride layers. *Thin Solid Films* **2014,** *558*, 54-61.

59. Zhang, S.; Xue, W.; Yu, Z., Moisture barrier evaluation of SiOx/SiNx stacks on polyimide substrates using electrical calcium test. *Thin Solid Films* **2015,** *580*, 101-105.

60. Wuu, D.; Lo, W.; Chiang, C.; Lin, H.; Chang, L.; Horng, R.; Huang, C.; Gao, Y., Water and oxygen permeation of silicon nitride films prepared by plasma-enhanced chemical vapor deposition. *Surface and Coatings Technology* **2005,** *198* (1), 114-117.

61. Keuning, W.; Van de Weijer, P.; Lifka, H.; Kessels, W.; Creatore, M., Cathode encapsulation of organic light emitting diodes by atomic layer deposited Al2O3 films and Al2O3/a-SiNx: H stacks. *J. Vac. Sci. Technol. A* **2012,** *30* (1), 01A131.

62. van Assche, F. J.; Unnikrishnan, S.; Michels, J. J.; van Mol, A. M.; van de Weijer, P.; van de Sanden, M. C.; Creatore, M., On the intrinsic moisture permeation rate of remote microwave plasma-deposited silicon nitride layers. *Thin Solid Films* **2014,** *558*, 54-61.

63. Martyniuk, M. P.; Antoszewski, J.; Musca, C. A.; Dell, J. M.; Faraone, L. In *Determination of residual stress in low-temperature PECVD silicon nitride thin films*, Microelectronics, MEMS, and Nanotechnology, International Society for Optics and Photonics: 2004; pp 451-462.

64. Huang, H.; Winchester, K. J.; Suvorova, A.; Lawn, B. R.; Liu, Y.; Hu, X. Z.; Dell, J. M.; Faraone, L., Effect of deposition conditions on mechanical properties of low-temperature PECVD silicon nitride films. *Materials Science and Engineering: A* **2006,** *435–436*, 453-459.

65. Huang, H.; Winchester, K.; Liu, Y.; Hu, X. Z.; Musca, C. A.; Dell, J. M.; Faraone, L., Determination of mechanical properties of PECVD silicon nitride thin films for tunable MEMS Fabry–Pérot optical filters. *J. Micromech. Microeng.* **2005,** *15* (3), 608-614.

66. Beuth, J. L. J., Cracking of thin bonded films in residual tension. *Int. J. Sol. Struct.* **1992,** *29* (13), 1657-1675.

67. Jen, S.-H.; Bertrand, J. A.; George, S. M., Critical tensile and compressive strains for cracking of Al2O3 films grown by atomic layer deposition. *Journal of Applied Physics* **2011,** *109* (8), 084305.

68. Jen, S.-H.; Lee, B. H.; George, S. M.; McLean, R. S.; Carcia, P. F., Critical tensile strain and water vapor transmission rate for nanolaminate films grown using Al2O3 atomic layer deposition and alucone molecular layer deposition. *Applied Physics Letters* **2012,** *101* (23), 234103.

69. Miller, D. C.; Foster, R. R.; Zhang, Y.; Jen, S.-H.; Bertrand, J. A.; Lu, Z.; Seghete, D.; O'Patchen, J. L.; Yang, R.; Lee, Y.-C.; George, S. M.; Dunn, M. L., The mechanical robustness of atomic-layer- and molecular-layer-deposited coatings on polymer substrates. *Journal of Applied Physics* **2009,** *105* (9), 093527.

70. Leterrier, Y., Durability of nanosized oxygen-barrier coatings on polymers. *Progress in Materials Science* **2003,** *48* (1), 1-55.

71. Andersons, J.; Modniks, J.; Leterrier, Y.; Tornare, G.; Dumont, P.; Månson, J. A. E., Evaluation of toughness by finite fracture mechanics from crack onset strain of brittle coatings on polymers. *Theoretical and Applied Fracture Mechanics* **2008,** *49* (2), 151-157.

72. Leterrier, Y.; Andersons, J.; Pitton, Y.; Månson, J. A., Adhesion of silicon oxide layers on poly (ethylene terephthalate). II: Effect of coating thickness on adhesive and cohesive strengths. *Journal of Polymer Science Part B: Polymer Physics* **1997,** *35* (9), 1463-1472.

73. Lewis, J., Material challenge for flexible organic devices. *Materials Today* **2006,** *9* (4), 38-45.

74. Lewis, J.; Grego, S.; Vick, E.; Chalamala, B.; Temple, D. In *Mechanical performance of thin films in flexible displays*, MRS Proceedings, Cambridge Univ Press: 2004; p I8. 5.

75. Behrendt, A.; Meyer, J.; van de Weijer, P.; Gahlmann, T.; Heiderhoff, R.; Riedl, T., Stress Management in Thin-Film Gas-Permeation Barriers. *ACS Applied Materials & Interfaces* **2016,** *8* (6), 4056-4061.

76. Allameh, S. M.; Suo, Z. G.; Soboyejo, W., Creep of Al underlayer determined by channel cracking of topical Si(3)N(4) film. *Materials and Manufacturing Processes* **2007,** *22* (2), 170-174.

77. Huang, R.; Prévost, J. H.; Suo, Z., Loss of constraint on fracture in thin film structures due to creep. *Acta Materialia* **2002,** *50* (16), 4137-4148.

78. Liang, J.; Huang, R.; Prevost, J. H.; Suo, Z., Thin film cracking modulated by underlayer creep. *Exper. Mech.* **2003,** *43* (3), 269-279.

79. Liang, J.; Zhang, Z.; Prevost, J. H.; Suo, Z., Time-dependent crack behavior in an integrated structure. *Int. J. Fract.* **2004,** *125* (3-4), 335-348.

80. Lane, M. W.; Liu, X. H.; Shaw, T. M., Environmental effects on cracking and delamination of dielectric films. *Device and Materials Reliability, IEEE Transactions on* **2004,** *4* (2), 142-147.

81. Lane, M. W.; Snodgrass, J. M.; Dauskardt, R. H., Environmental effects on interfacial adhesion. *Microelectronics Reliability* **2001,** *41* (9-10), 1615-1624.

82. Li, H.; Tsui, T. Y.; Vlassak, J. J., Water diffusion and fracture behavior in nanoporous low-k dielectric film stacks. *J. Appl. Phys.* **2009,** *106* (3).

83. Lin, Y. B.; Tsui, T. Y.; Vlassak, J. J., Water diffusion and fracture in organosilicate glass film stacks. *Acta Materialia* **2007,** *55* (7), 2455-2464.

84. Birringer, R. P.; Shaviv, R.; Besser, P. R.; Dauskardt, R. H., Environmentally assisted debonding of copper/barrier interfaces. *Acta Materialia* **2012,** *60* (5), 2219-2228.

85. Vellinga, W. P.; De Hosson, J. T. M.; Bouten, P. C. P., Effect of relative humidity on crack propagation in barrier films for flexible electronics. *J. Appl. Phys.* **2012,** *112* (8), 083520.

86. Guan, Q.; Laven, J.; Bouten, P. C. P.; de With, G., Subcritical crack growth in SiNx thin-film barriers studied by electro-mechanical two-point bending. *J. Appl. Phys.* **2013,** *113* (21), 213512.

87. Bhatnagar, A.; Hoffman, M. J.; Dauskardt, R. H., Fracture and Subcritical Crack-Growth Behavior of Y-Si-Al-O-N Glasses and Si3N4 Ceramics. *J. Am. Ceram. Soc.* **2000,** *83* (3), 585-596.

88. Ishihara, S.; McEvily, A. J.; Goshima, T., Effect of atmospheric humidity on the fatigue crack propagation behavior of short cracks in silicon nitride. *J. Am. Ceram. Soc.* **2000,** *83* (3), 571.

89. McDowell, M. T.; Ryu, I.; Lee, S. W.; Wang, C.; Nix, W. D.; Cui, Y., Studying the Kinetics of Crystalline Silicon Nanoparticle Lithiation with In Situ Transmission Electron Microscopy. *Advanced Materials* **2012,** *24* (45), 6034-6041.

90. Liu, X. H.; Wang, J. W.; Huang, S.; Fan, F.; Huang, X.; Liu, Y.; Krylyuk, S.; Yoo, J.; Dayeh, S. A.; Davydov, A. V.; Mao, S. X.; Picraux, S. T.; Zhang, S.; Li, J.; Zhu, T.; Huang, J. Y., In situ atomic-scale imaging of electrochemical lithiation in silicon. *Nat Nano* **2012,** *7* (11), 749-756.

91. Lee, S. W.; McDowell, M. T.; Choi, J. W.; Cui, Y., Anomalous Shape Changes of Silicon Nanopillars by Electrochemical Lithiation. *Nano Letters* **2011,** *11* (7), 3034-3039.

92. Wang, J. W.; He, Y.; Fan, F.; Liu, X. H.; Xia, S.; Liu, Y.; Harris, C. T.; Li, H.; Huang, J. Y.; Mao, S. X.; Zhu, T., Two-Phase Electrochemical Lithiation in Amorphous Silicon. *Nano Letters* **2013,** *13* (2), 709-715.

93. Chandrasekaran, R.; Magasinski, A.; Yushin, G.; Fuller, T. F., Analysis of Lithium Insertion/Deinsertion in a Silicon Electrode Particle at Room Temperature. *Journal of The Electrochemical Society* **2010,** *157* (10), A1139-A1151.

94. Gao, Y. F.; Zhou, M., Strong stress-enhanced diffusion in amorphous lithium alloy nanowire electrodes. *Journal of Applied Physics* **2011,** *109* (1), 014310.

95. Huang, S.; Fan, F.; Li, J.; Zhang, S.; Zhu, T., Stress generation during lithiation of high-capacity electrode particles in lithium ion batteries. *Acta Materialia* **2013,** *61* (12), 4354-4364.

96. Chen, L.; Fan, F.; Hong, L.; Chen, J.; Ji, Y. Z.; Zhang, S. L.; Zhu, T.; Chen, L. Q., A Phase-Field Model Coupled with Large Elasto-Plastic Deformation: Application to Lithiated Silicon Electrodes. *Journal of The Electrochemical Society* **2014,** *161* (11), F3164-F3172.

97. Yang, H.; Fan, F.; Liang, W.; Guo, X.; Zhu, T.; Zhang, S., A chemo-mechanical model of lithiation in silicon. *Journal of the Mechanics and Physics of Solids* **2014,** *70*, 349-361.

98. Goodenough, J. B.; Kim, Y., Challenges for Rechargeable Li Batteries. *Chem. Mater.* **2009,** *22* (3), 587-603.

99. Nitta, N.; Yushin, G., High-Capacity Anode Materials for Lithium-Ion Batteries: Choice of Elements and Structures for Active Particles. *Particle & Particle Systems Characterization* **2014,** *31* (3), 317-336.

100. Su, X.; Wu, Q.; Li, J.; Xiao, X.; Lott, A.; Lu, W.; Sheldon, B. W.; Wu, J., Silicon-Based Nanomaterials for Lithium-Ion Batteries: A Review. *Advanced Energy Materials* **2014,** *4* (1), n/a-n/a.

101. Kim, H.; Lee, E.-J.; Sun, Y.-K., Recent advances in the Si-based nanocomposite materials as high capacity anode materials for lithium ion batteries. *Mater. Today* **2014,** *17* (6), 285-297.

102. Liu, Y.; Zhang, S.; Zhu, T., Germanium-Based Electrode Materials for Lithium-Ion Batteries. *ChemElectroChem* **2014,** *1* (4), 706-713.

103. Wang, B.; Luo, B.; Li, X.; Zhi, L., The dimensionality of Sn anodes in Li-ion batteries. *Mater. Today* **2012,** *15* (12), 544-552.

104. Goldman, J. L.; Long, B. R.; Gewirth, A. A.; Nuzzo, R. G., Strain Anisotropies and Self-Limiting Capacities in Single-Crystalline 3D Silicon Microstructures: Models for High Energy Density Lithium-Ion Battery Anodes. *Adv. Funct. Mater.* **2011,** *21* (13), 2412-2422.

105. Liu, Y.; Hudak, N. S.; Huber, D. L.; Limmer, S. J.; Sullivan, J. P.; Huang, J. Y., In Situ Transmission Electron Microscopy Observation of Pulverization of Aluminum Nanowires and Evolution of the Thin Surface Al2O3 Layers during Lithiation–Delithiation Cycles. *Nano Lett.* **2011,** *11* (10), 4188-4194.

106. Liu, Y.; Liu, X. H.; Nguyen, B.-M.; Yoo, J.; Sullivan, J. P.; Picraux, S. T.; Huang, J. Y.; Dayeh, S. A., Tailoring Lithiation Behavior by Interface and Bandgap Engineering at the Nanoscale. *Nano Lett.* **2013,** *13* (10), 4876-4883.

107. Liu, X. H.; Fan, F.; Yang, H.; Zhang, S.; Huang, J. Y.; Zhu, T., Self-Limiting Lithiation in Silicon Nanowires. *ACS Nano* **2012,** *7* (2), 1495-1503.

108. Ariel, N.; Ceder, G.; Sadoway, D. R.; Fitzgerald, E. A., Electrochemically controlled transport of lithium through ultrathin SiO2. *J. Appl. Phys.* **2005,** *98* (2), -.

109. Hwa, Y.; Park, C.-M.; Sohn, H.-J., Modified SiO as a high performance anode for Li-ion batteries. *J. Power Sources* **2013,** *222* (0), 129-134.

110. Sun, Q.; Zhang, B.; Fu, Z.-W., Lithium electrochemistry of SiO2 thin film electrode for lithium-ion batteries. *Appl. Surf. Sci.* **2008,** *254* (13), 3774-3779.

111. Li, X.; Dhanabalan, A.; Meng, X.; Gu, L.; Sun, X.; Wang, C., Nanoporous tree-like SiO2 films fabricated by sol–gel assisted electrostatic spray deposition. *Microporous Mesoporous Mater.* **2012,** *151* (0), 488-494.

112. Wang, J.; Zhao, H.; He, J.; Wang, C.; Wang, J., Nano-sized SiOx/C composite anode for lithium ion batteries. *J. Power Sources* **2011,** *196* (10), 4811-4815.

113. Favors, Z.; Wang, W.; Bay, H. H.; George, A.; Ozkan, M.; Ozkan, C. S., Stable Cycling of SiO2 Nanotubes as High-Performance Anodes for Lithium-Ion Batteries. *Sci. Rep.* **2014,** *4*.

114. Yan, N.; Wang, F.; Zhong, H.; Li, Y.; Wang, Y.; Hu, L.; Chen, Q., Hollow Porous SiO2 Nanocubes Towards High-performance Anodes for Lithium-ion Batteries. *Sci. Rep.* **2013,** *3*.

115. Guo, B.; Shu, J.; Wang, Z.; Yang, H.; Shi, L.; Liu, Y.; Chen, L., Electrochemical reduction of nano-SiO2 in hard carbon as anode material for lithium ion batteries. *Electrochem. Commun.* **2008,** *10* (12), 1876-1878.

116. Kim, S.-Y.; Qi, Y., Property Evolution of Al2O3 Coated and Uncoated Si Electrodes: A First Principles Investigation. *J. Electrochem. Soc.* **2014,** *161* (11), F3137-F3143.

117. Zhang, Y.; Li, Y.; Wang, Z.; Zhao, K., Lithiation of SiO2 in Li-Ion Batteries: In Situ Transmission Electron Microscopy Experiments and Theoretical Studies. *Nano Lett.* **2014**.

118. Zinn, A.-H.; Borhani-Haghighi, S.; Ventosa, E.; Pfetzing-Micklich, J.; Wieczorek, N.; Schuhmann, W.; Ludwig, A., Mechanical properties of SiLix thin films at different stages of electrochemical Li insertion. *physica status solidi (a)* **2014,** *211* (11), 2650-2656.

119. Berla, L. A.; Lee, S. W.; Cui, Y.; Nix, W. D., Mechanical behavior of electrochemically lithiated silicon. *J. Power Sources* **2015,** *273* (0), 41-51.

120. Du, J.; Chen, C.-H., Structure and lithium ion diffusion in lithium silicate glasses and at their interfaces with lithium lanthanum titanate crystals. *J. Non-Cryst. Solids* **2012,** *358* (24), 3531-3538.

121. Huggins, R. A., Recent results on lithium ion conductors. *Electrochim. Acta* **1977,** *22* (7), 773-781.

122. Chang, W.-S.; Park, C.-M.; Kim, J.-H.; Kim, Y.-U.; Jeong, G.; Sohn, H.-J., Quartz (SiO2): a new energy storage anode material for Li-ion batteries. *Energy Environ. Sci.* **2012,** *5* (5), 6895-6899.

123. Wang, J.; Luo, H.; Liu, Y.; He, Y.; Fan, F.; Zhang, Z.; Mao, S. X.; Wang, C.; Zhu, T., Tuning the Outward to Inward Swelling in Lithiated Silicon Nanotubes via Surface Oxide Coating. *Nano Letters* **2016,** *16* (9), 5815-5822.

124. Xia, F.; Kim, S. B.; Cheng, H.; Lee, J. M.; Song, T.; Huang, Y.; Rogers, J. A.; Paik, U.; Park, W. I., Facile Synthesis of Free-Standing Silicon Membranes with Three-Dimensional Nanoarchitecture for Anodes of Lithium Ion Batteries. *Nano Lett.* **2013,** *13* (7), 3340-3346.

125. Ge, M.; Lu, Y.; Ercius, P.; Rong, J.; Fang, X.; Mecklenburg, M.; Zhou, C., Large-Scale Fabrication, 3D Tomography, and Lithium-Ion Battery Application of Porous Silicon. *Nano Lett.* **2014,** *14* (1), 261-268.

126. Kim, H.; Han, B.; Choo, J.; Cho, J., Three-Dimensional Porous Silicon Particles for Use in High-Performance Lithium Secondary Batteries. *Angew. Chem. Int. Ed.* **2008,** *47* (52), 10151-10154.

127. Ge, M.; Fang, X.; Rong, J.; Zhou, C., Review of porous silicon preparation and its application for lithium-ion battery anodes. *Nanotechnology* **2013,** *24* (42), 422001.

128. Ye, J. C.; An, Y. H.; Heo, T. W.; Biener, M. M.; Nikolic, R. J.; Tang, M.; Jiang, H.; Wang, Y. M., Enhanced lithiation and fracture behavior of silicon mesoscale pillars via atomic layer coatings and geometry design. *J. Power Sources* **2014,** *248*, 447-456.

129. Hassan, F. M.; Chabot, V.; Elsayed, A. R.; Xiao, X.; Chen, Z., Engineered Si Electrode Nanoarchitecture: A Scalable Postfabrication Treatment for the Production of Next-Generation Li-Ion Batteries. *Nano Lett.* **2013,** *14* (1), 277-283.

130. Yoo, H.; Lee, J.-I.; Kim, H.; Lee, J.-P.; Cho, J.; Park, S., Helical Silicon/Silicon Oxide Core–Shell Anodes Grown onto the Surface of Bulk Silicon. *Nano Lett.* **2011,** *11* (10), 4324-4328.

131. Yu, B.-C.; Hwa, Y.; Park, C.-M.; Kim, J.-H.; Sohn, H.-J., Effect of oxide layer thickness to nano-Si anode for Li-ion batteries. *RSC Advances* **2013,** *3* (24), 9408-9413.

132. Wang, J. W.; Liu, X. H.; Zhao, K.; Palmer, A.; Patten, E.; Burton, D.; Mao, S. X.; Suo, Z.; Huang, J. Y., Sandwich-Lithiation and Longitudinal Crack in Amorphous Silicon Coated on Carbon Nanofibers. *Acs Nano* **2012**, DOI:10.1021/nn3034343.

133. Huang, S.; Fan, F.; Li, J.; Zhang, S. L.; Zhu, T., Stress generation during lithiation of high-capacity electrode particles in lithium ion batteries. *Acta Materialia* **2013,** *61*, 4354-4364.

134. Hsueh, C. H.; Evans, A. G., Oxidation-induced stress and some effects on the behavior of oxide-films. *Journal of Applied Physics* **1983,** *54* (11), 6672-6686.

135. Liang, W.; Yang, H.; Fan, F.; Liu, Y.; Liu, X. H.; Huang, J. Y.; Zhu, T.; Zhang, S., Tough Germanium Nanoparticles under Electrochemical Cycling. *ACS Nano* **2013**, doi: 10.1021/nn400330h.

136. Jung, Y. S.; Lee, K. T.; Oh, S. M., Si–carbon core–shell composite anode in lithium secondary batteries. *Electrochim. Acta* **2007,** *52* (24), 7061-7067.

137. Gu, M.; Li, Y.; Li, X.; Hu, S.; Zhang, X.; Xu, W.; Thevuthasan, S.; Baer, D. R.; Zhang, J.-G.; Liu, J.; Wang, C., In Situ TEM Study of Lithiation Behavior of Silicon Nanoparticles Attached to and Embedded in a Carbon Matrix. *ACS Nano* **2012,** *6* (9), 8439-8447.

138. Liu, J.; Li, N.; Goodman, M. D.; Zhang, H. G.; Epstein, E. S.; Huang, B.; Pan, Z.; Kim, J.; Choi, J. H.; Huang, X.; Liu, J.; Hsia, K. J.; Dillon, S. J.; Braun, P. V., Mechanically and Chemically Robust Sandwich-Structured C@Si@C Nanotube Array Li-Ion Battery Anodes. *ACS Nano* **2015,** *9* (2), 1985-1994.

139. Karki, K.; Zhu, Y.; Liu, Y.; Sun, C.-F.; Hu, L.; Wang, Y.; Wang, C.; Cumings, J., Hoop-Strong Nanotubes for Battery Electrodes. *ACS Nano* **2013,** *7* (9), 8295-8302.

140. Favors, Z.; Wang, W.; Bay, H. H.; George, A.; Ozkan, M.; Ozkan, C. S., Stable Cycling of SiO2 Nanotubes as High-Performance Anodes for Lithium-Ion Batteries. *Sci. Rep.* **2014,** *4*, 4605

141. Wang, C.-M.; Li, X.; Wang, Z.; Xu, W.; Liu, J.; Gao, F.; Kovarik, L.; Zhang, J.-G.; Howe, J.; Burton, D. J.; Liu, Z.; Xiao, X.; Thevuthasan, S.; Baer, D. R., In Situ TEM Investigation of Congruent Phase Transition and Structural Evolution of Nanostructured Silicon/Carbon Anode for Lithium Ion Batteries. *Nano Lett.* **2012,** *12* (3), 1624-1632.

142. Liu, X. H.; Wang, J. W.; Huang, S.; Fan, F.; Huang, X.; Liu, Y.; Krylyuk, S.; Yoo, J.; Dayeh, S. A.; Davydov, A. V., In situ atomic-scale imaging of electrochemical lithiation in silicon. *Nat. Nanotechnol.* **2012,** *7* (11), 749-756.

143. Song, T.; Cheng, H. Y.; Choi, H.; Lee, J. H.; Han, H.; Lee, D. H.; Yoo, D. S.; Kwon, M. S.; Choi, J. M.; Doo, S. G.; Chang, H.; Xiao, J. L.; Huang, Y. G.; Park, W. I.; Chung, Y. C.; Kim, H.; Rogers, J. A.; Paik, U., Si/Ge double-layered nanotube array as a lithium ion battery anode. *Acs Nano* **2012,** *6* (1), 303-309.

144. Liu, X. H.; Huang, S.; Picraux, S. T.; Li, J.; Zhu, T.; Huang, J. Y., Reversible nanopore formation in Ge nanowires during lithiation–delithiation cycling: An in situ transmission electron microscopy study. *Nano Letters* **2011,** *11* (9), 3991-3997.

145. Liu, X. H.; Liu, Y.; Kushima, A.; Zhang, S. L.; Zhu, T.; Li, J.; Huang, J. Y., In situ TEM experiments of electrochemical lithiation and delithiation of individual nanostructures. *Advanced Energy Materials* **2012,** *2* (7), 722-741.

146. Baggetto, L.; Niessen, R. A. H.; Roozeboom, F.; Notten, P. H. L., High energy density all-solid-state batteries: A challenging concept towards 3D integration. *Advanced Functional Materials* **2008,** *18* (7), 1057-1066.

147. Baggetto, L.; Notten, P. H. L., Lithium-ion (de)insertion reaction of germanium thin-film electrodes: An electrochemical and in situ XRD study. *Journal of the Electrochemical Society* **2009,** *156* (3), A169-A175.

148. Wang, J.; Luo, H.; Liu, Y.; He, Y.; Fan, F.; Zhang, Z.; Mao, S. X.; Wang, C.; Zhu, T., Tuning the outward to inward swelling in lithiated silicon nanotubes via surface oxide coating. *Nano Letters* **2016**, 10.1021/acs.nanolett.6b02581.

149. Yu, J. X.; Du, N.; Zhang, H.; Yang, D. R., Synthesis of NixSiy-SiGe core-shell nanowire arrays on Ni foam as a high-performance anode for Li-ion batteries. *RSC Adv.* **2013,** *3* (21), 7713-7717.

150. Qiu, X.-Y.; Zhuang, Q.-C.; Zhang, Q.-Q.; Cao, R.; Qiang, Y.-H.; Ying, P.-Z.; Sun, S.-G., Investigation of layered LiNi1/3Co1/3Mn1/3O2 cathode of lithium ion battery by electrochemical impedance spectroscopy. *Journal of Electroanalytical Chemistry* **2012,** *687*, 35-44.

151. Kim, K.; Luo, H.; Singh, A. K.; Zhu, T.; Graham, S.; Pierron, O. N., Environmentally Assisted Cracking in Silicon Nitride Barrier Films on Poly(ethylene terephthalate) Substrates. *ACS Applied Materials & Interfaces* **2016,** *8* (40), 27169-27178.

152. ABAQUS/Standard 6.13, User's Manual. *SIMULIA, Providence, R.I.* **2010**.

153. Rice, J. R., A path independent integral and the approximate analysis of strain concentrations by notches and cracks. *Journal of Applied Mechanics* **1968,** *35* (2), 379-386.

154. Hutchinson, J. W.; Suo, Z., Mixed mode cracking in layered materials. *Advances in Applied Mechanics* **1992,** *29*, 63-191.

155. Vlassak, J. J., Channel cracking in thin films on substrates of finite thickness. *Int. J. Fract.* **2003,** *119* (4), 299-323.

156. Huang, R.; Prevost, J. H.; Huang, Z. Y.; Suo, Z., Channel-cracking of thin films with the extended finite element method. *Engin. Fract. Mech.* **2003,** *70* (18), 2513-2526.

157. Anderson, T. L., *Fracture mechanics: fundamentals and applications*. Boca Raton: 1995.

158. Hu, M. S.; Evans, A. G., THE CRACKING AND DECOHESION OF THIN-FILMS ON DUCTILE SUBSTRATES. *Acta Metal.* **1989,** *37* (3), 917-925.

159. Rice, J., *A path independent integral and the approximate analysis of strain concentration by notched and cracks*. 1968; Vol. 35.

160. Kim, K.; Graham, S.; Pierron, O. N., Note: A single specimen channel crack growth technique applied to brittle thin films on polymer substrates. *Rev Sci Instrum* **2017,** *88* (3), 036102.

161. Kim, K.; Luo, H.; Singh, A. K.; Zhu, T.; Graham, S.; Pierron, O. N., Environmentally Assisted Cracking in Silicon Nitride Barrier Films on Poly(ethylene terephthalate) Substrates. *ACS applied materials & interfaces* **2016**.

162. Huang, R.; Prévost, J. H.; Huang, Z. Y.; Suo, Z., Channel-cracking of thin films with the extended finite element method. *Engineering Fracture Mechanics* **2003,** *70* (18), 2513-2526.

163. ABAQUS/Standard 6.13, U. s. M., SIMULIA, Providence, RI. **2010**.